UNIVERSITY OF SOUTHAMPTON

FACULTY OF ENGINEERING AND THE ENVIRONMENT

national Centre for Advanced Tribology at Southampton (nCATS) & Bioengineering Sciences Research Group

Towards a micromechanical insight into the visco-dynamic behaviour of UHMWPE for the modelling of knee joint replacement systems

by

Federico Quinci

Thesis for the degree of Doctor of Philosophy

March 2014

UNIVERSITY OF SOUTHAMPTON

ABSTRACT

FACULTY OF ENGINEERING AND THE ENVIRONMENT
national Centre for Advanced Tribology at Southampton (nCATS) & Bioengineering Sciences Research Group

Doctor of Philosophy

TOWARDS A MICROMECHANICAL INSIGHT INTO THE VISCO-DYNAMIC BEHAVIOUR OF UHMWPE FOR THE MODELLING OF KNEE JOINT REPLACEMENT SYSTEMS

by Federico Quinci

Considerable progress has been made in understanding implant wear and developing numerical models to predict certain aspects of wear for new orthopaedic devices. However, any model of wear could be improved through a more accurate representation of the biomaterial micromechanics, including time-varying dynamic and inelastic behaviour such as viscous and plastic deformation as well as any history-dependent evolution of its microstructural properties.

Under in-vivo conditions, the contact surface of the UHMWPE tibial insert evolves as a result of applied loads and complex multidirectional motions of the femoral component against it. Overt time, severe inelastic deformations and damage mechanisms occur and ultimately lead to wear. This process is accompanied by the release of UHMWPE debris in the surrounding tissues with the direct consequences of triggering an inflammatory response that leads to osteolysis and subsequently periprosthetic implant loosening. In that case a revision surgery is required.

Motivated by these facts, the current research effort has been motivated by the need to gain a mechanistic insight into the micromechanical mechanisms associated with wear of UHMWPE in knee arthroplasty. To this end, two main lines of focus have been followed in this work.

One line of focus concerns the inelastic mechanisms of deformation such as creep and plasticity since they are critical in altering the contact properties of the articulating surface of UHMWPE components, leading to damage and formation of wear debris. Therefore, the relative contributions of elastic, creep, and plastic deformations on the contact area, and so contact pressure has been investigated through different numerical techniques. Additionally, contact pressure is a critical input parameter of computational wear algorithms, and it is therefore essential to establish the nature of and quantify the interplay between contact pressure, contact area, creep and plastic deformations. What are the consequences of neglecting creep deformations on wear predictions?

A first approach to investigate these aspects consisted in conducting a series of physically-based finite element analyses replicating the mechanical characteristics and operating conditions of an AMTI Knee Simulator. Experimental creep testing on a unicondylar knee replacement system in a physiologically representative context was simulated. In both studies, linear elastic, plastic and time-varying visco-dynamic properties of computational models were benchmarked using literature data to predict contact deformations, pressures and areas.
Results indicate that creep deformations have a significant effect on both experimental and simulated contact pressures at the surface of the UHMWPE tibial insert. The use of a purely elastoplastic constitutive model for UHMWPE lead to compressive deformations of the insert which were in general smaller than those predicted by a creep-capturing viscoelastic model. At high compressive loads, inelastic deformation mechanisms dominate the mechanical response of UHMWPE components by altering the surface geometry (i.e. contact area), and therefore the contact pressure.
The second line of focus concerns the study of the role of transient and permanent polymer chain realignment during multidirectional sliding, and its potential correlation to wear. The main working hypothesis is that the evolution of the UHMWPE microstructure during multidirectional pin-on-disk (POD) tests can provide information on possible correlations between wear, sliding track characteristics and the mechanics of UHMWPE. Therefore, finite element-based POD tests were used to investigate the effects of motion paths in simulated multidirectional sliding motions on metrics related to the mechanical response of UHMWPE, with particular attention to evolution of molecular chain realignment. For this purpose, the concept of *anticoaxiality* as a measure of molecular chain realignment (or anisotropy) has been introduced.
The concept of *anticoaxiality* as a measure of molecular chain realignment (or anisotropy) was introduced to quantify the deviation from mechanical isotropy of UHMWPE microstructure. Results from these metrics support the hypothesis that multidirectional sliding as well as long sliding distances produced microstructural changes in UHMWPE, resulting in an enhanced likelihood of material damage, and so wear.

Contents

List of Figures

List of Tables

Declaration of Authorship

I, Federico Quinci, declare that the thesis entitled *Towards a micromechanical insight into the visco-dynamic behaviour of UHMWPE for the modelling of knee joint replacement systems* and the work presented in the thesis are both my own, and have been generated by me as the result of my own original research. I confirm that:

- this work was done wholly or mainly while in candidature for a research degree at this University;
- where any part of this thesis has previously been submitted for a degree or any other qualification at this University or any other institution, this has been clearly stated;
- where I have consulted the published work of others, this is always clearly attributed;
- where I have quoted from the work of others, the source is always given. With the exception of such quotations, this thesis is entirely my own work;
- I have acknowledged all main sources of help;
- where the thesis is based on work done by myself jointly with others, I have made clear exactly what was done by others and what I have contributed myself;
- parts of this work have been published as:

  Quinci, et al. (2013). The role of viscoelastic and plastic effects in the creep behaviour of UHMWPE: An experimentally based computational study using an AMTI knee wear simulator. In *Multifunctional Materials for Tribological Applications*. Pan Stanford Publishing Pte. Ltd. *In press*

  Quinci, et al. (2014). Towards an accurate understanding of UHMWPE visco-dynamic behaviour for numerical modelling of implants. JMBBM. 32, 62-75.

Signed:.....

Date:.....

Acknowledgements

This PhD project would not have been possible without the support of many people. I wish to express my deepest gratitude to my supervisor and friend, Dr Georges Limbert who offered invaluable assistance, support, and guidance throughout these years.

Deepest gratitude is also due to my supervisor at DePuy Dr Matthew Dressler and Dr Michael Strickland, whose knowledge and assistance were crucial for the success of this project.

Special thanks also to all my postgraduate friends, especially group members of the bioengineering research group and nCATS for sharing invaluable assistance and good moments. In particular, thanks to Michele, Dario, Lorenzo, Stefano, Orestis K., Orestis A., and Maria.

A sincere thanks to my best friends Antonio (spina), Enrico (Enri), Roberto (Mic), Stefano (Zullo), and Enrico C. (Ciup), whom I have shared the most valuable experiences of life and the best moments of joyfulness with.

I wish to express my deepest love and gratitude to my mum Clara, granny Orsolina, and uncle Danilo, for their understanding and love through the duration of my studies. Indeed, without their presence this achievement would not have been possible.

I would also spare a thought to my guardian angels Piero and Giovanni, which circumstances of life took them away far too soon.

I would also like to convey thanks to my soulmate Dr Stefania Mazzitelli for her endless support and patience offered during the harshest periods of this PhD, with the wish of sharing an entire life of personal successes and beautiful moments together.

"Satisfaction lies in the effort, not in the attainment. Full effort is victory"
[M. Gandhi]

Nomenclature

UHMWPE	Ultra High Molecular Weight Polyethylene
TJR	Total Joint Replacement
TKR	Total Knee Replacement
THR	Total Hip Replacement
UKR	Unicondylar Knee Replacement
PCL	Posterior Cruciate Ligament
FE	Finite Elements
MBD	Multi Body Dynamics
CA	Contact Area
CP	Contact Pressure
PD	Penetration Depth
AMTI	Multiaxial Biomedical Testing Machines
MoP	Metal on Polyethylene
CS	Cross Shear
POD	Pin on Disk
CRSS	Critical Resolved Shear Stress
DCM	Direct Compression Molding
BW	Body Weight
CAD	Computer Aided Design
Q−C	Quality Check
LS	Laser Scanner
Pr	Profilometer
Ph	Photographs
I−E	Internal External
A−P	Anterior Posterior
V−V	Valgus Varus
M−L	Medial Lateral
E-FE	Elastic Finite Element
EP-FE	Elastic Plastic Finite Element
EV-FE	Elastic Viscoelastic Finite Element
FE-E	Finite Element Elastic
FE-P	Finite Element Plastic

FE-V	Finite Element Viscoelastic
T_m	Melt transition temperature
T_g	Glass transition temperature
F	Contact force
E	Linear elastic modulus
ν	Poisson ratio
A	Individual cell area
h	Material thickness
d	Interpenetration depth
d_{creep}	Interval creep depth
t_{start}	Start time
t_{end}	End time
$\mathbf{F}$	Deformation gradient
$\mathbf{F}_A^e, \mathbf{F}_B^e$	Elastic component of the deformation gradient acting on networks A and B
$\mathbf{F}_A^\nu, \mathbf{F}_B^\nu$	Viscoplastic component of the deformation gradient acting on networks A and B
$\sigma_A, \sigma_B, \sigma_C$	Cauchy stress acting on networks A, B, and C
μ_A, μ_C	Initial shear modulus of networks A and C
μ_{Bi}, μ_{Bf}	Initial and final shear modulus of network B
J_A^e, J_B^e, J	Jacobian determinant of networks A, B, and C
$\bar{\lambda}_A^{e^*}, \bar{\lambda}_B^{e^*}, \lambda_{chain}$	Effective chain stretch of networks A, B, C based on the eight chain topology assumption
θ, θ_0	Current temperature and reference temperature
$\hat{\theta}$	Parameter for the temperature response of the stiffness
$\mathfrak{L}^{-1}$	Inverse Langevin function
λ_L	Chain locking stretch
$\mathbf{b}_A^{e^*}, \mathbf{b}_B^{e^*}, \mathbf{b}^*$	Cauchy-Green deformation tensor of networks A, B, and C
κ	Bulk modulus
β	Evolution rate of μ_B
$\dot{\gamma_A}, \dot{\gamma_B}$	Viscoplastic (deviatoric) flow rate acting on networks A and B
I_2	Second invariant
q	Relative contribution of I_2 of network C
$\mathbf{L}$	Total velocity gradient
$\mathbf{L}_A^e, \mathbf{L}_B^e$	Elastic component of the velocity gradient of networks A and B
$\tilde{\mathbf{D}}_A^\nu, \tilde{\mathbf{D}}_B^\nu$	Rate of viscoplastic flow of networks A and B
$\tilde{\mathbf{W}}_A^\nu, \tilde{\mathbf{W}}_B^\nu$	Skew (spin) part of the velocity gradient of networks A and B
$\mathbf{N}_A, \mathbf{N}_B$	Direction of the driving deviatoric stress of networks A and B
τ_A, τ_B	Effective stress of network A and B
σ'_A, σ'_B	Driving deviatoric stress of networks A and B
m_A, m_B	Stress exponential of networks A and B
a	Pressure dependence of flow
$\hat{\tau_A}, \hat{\tau_B}$	Flow resistance of networks A and B
p_A, p_B	Hydrostatic pressure of networks A and B

$R(x)$	Rump function
$\dot{\mu_B}$	Evolution of the effective shear modulus with plastic strain
$\dot{\gamma_0}$	Constant introduced for dimensional consistency
n	Parameter controlling the temperature dependency

Chapter 1

Introduction

1.1 Background

Ultra high molecular weight polyethylene (UHMWPE) has been widely used as standard bearing material for total joint replacements (TJRs) due to its excellent properties such as biocompatibility, chemical stability, ductility, fatigue resistance, and superior wear resistance when compared to other polymers (Saikko, 1993; Goldman and Pruitt, 1998). However, wear of UHMWPE is the main limiting factor influencing the longevity of TJRs, and more particularly that of total knee replacement (TKR)(Walker et al., 1996; Dressler et al., 2011; Strickland et al., 2012). The generation of micron or sub-micron size wear particles from the bearing surface of UHMWPE is known to cause a cascade of reactions in the surrounding soft tissues of the knee that will ultimately lead to osteolysis and to the need of revision surgery (Wang, 2001; Takahashi et al., 2013).

Because of change in the diversity of patient demographics with younger and more active patients, and an increase of life expectancy, TKR components made of UHMWPE are required to last longer and operate under a wider range of conditions. In particular, studies have revealed that young patients might need three or more revisions within 15 years (Dressler et al., 2011; Malchau and Herberts, 1996), which is not the case for less active elderly patients where a single implant can last for more that 20 years before arthoplasty revision surgery (Malchau and Herberts, 1996). Revision surgery is a more detrimental procedure than the primary operation since a higher volume of bone-stock is removed (Barbour et al., 1997).

In order to enhance the lifetime of knee implants, the negative effects of damage mechanisms such as wear and delamination, should be reduced as much as possible. Currently, wear of TKR designs is assessed through *in vitro* experimental tests, however, these are expensive, time consuming, and are only able to replicate restricted and specific loading scenarios (Dressler et al., 2011).

Therefore, comparatively fast computational tools for pre-clinical wear prediction such as multi body dynamics (MBD) (Strickland et al., 2012) and finite element (FE) analysis (Knight et al., 2007) have been recently developed, and the initial results look promising. Considerable progress has been made in understanding implant wear and building numerical models to predict wear for new orthopaedic devices. Generally, the approaches for predicting the mechanical response of UHMWPE components in TJRs can be either phenomenological or micro-structurally-based, or a combination of both.

Most computational models of wear of UHMWPE in TKRs implement a time-invariant version of Archard's law of wear (Archard, 1953) that links the volume of worn material (W) to the contact pressure (CP) between the metal implant and the polymeric tibial insert, sliding distance (s), and an empirical wear factor (k) (i.e. $W = k \cdot CP \cdot s$). The parameter k includes factors related to the articulating surface such as hardness and real contact area (CA) (Mazzucco and Spector, 2003; Archard, 1953). These "first generation" wear models are phenomenological in nature, do not adequately capture the physics of the wear mechanisms, and do not generalise to arbitrary loading conditions. Recently, *in vitro* tests have revealed the effect of multidirectional motions of articulating joints on increasing wear rates of UHMWPE components (Wang et al., 1997). This finding has led to the development of a "second generation" of wear models accounting for the concept of cross-shear (CS), which is defined as the measure of the deviation in sliding orientation with respect to the principal sliding direction (Wang, 2001). Again, the applicability of these models is restricted to specific kinematic conditions where wear rates are assumed to be constant (Strickland et al., 2012). Current models of wear could be improved through a more accurate representation of the UHMWPE mechanics, including time-varying dynamic and inelastic behaviour such as viscoelasticity and plasticity. The inclusion of micro-mechanical deformation mechanisms accounting for the semi-crystalline structure of UHMWPE would also be relevant.

In particular, a more mechanistic physics-based approach in predicting the mechanical response of UHMWPE undergoing cyclic loading and multidirectional sliding could be supported by constitutive theories for semi-crystalline polymers (Boyce et al., 1989). Most of these formulations are used to predict stress and strain distributions within UHMWPE components in TJRs, and incorporate finite strain time-dependent properties such as viscoelasticity and viscoplasticity (Arruda and Boyce, 1993; Bergström et al., 2003; Boyce et al., 1989; Hasan and Boyce, 1995; Bergström and Bischoff, 2011). These models present a varying degree of complexity and the identification of a potentially large number of material parameters from experimental tests can prove challenging. Although most of these theories are quite capable of predicting the mechanical response of a polymer under a wide range of loading conditions (Bergström et al., 2002), their constitutive formulation do not include wear *per se*, which is still viewed as a system property rather than an intrinsic material property.

Nevertheless, if improved, phenomenological-based wear models and constitutive theories for semi-crystalline polymers might ultimately provide greater flexibility and allow for a more rigorous analysis of the wear potential for new orthopaedic implant designs than what is currently possible using state of the art computational wear models.

1.2 Aims of this PhD work

The current research effort has been motivated by the need to gain a mechanistic insight into the micromechanical mechanisms associated with wear of UHMWPE components in TKRs during simulated *in-vivo* operating conditions. Therefore, the ultimate goal was the development of a predictive computational mechanistic model capable of accounting for changes in the microstructure of UHMWPE when subjected to different external loading conditions. To this end, two main lines of focus have been followed in this PhD work.

As reported in the literature (D'Lima et al., 2008), normal activities such as walking and running generate severe *in vivo* loading conditions at the articulating surface of the UHMWPE tibial insert in a TKR, which alter the characteristics of the knee implant and eventually limit its functionality.
Therefore, **one line of focus concerns the inelastic deformation mechanisms such as creep and plasticity, which are critical because of their role in modifying the contact properties of the articulating surface of UHMWPE components, leading to damage initiation and generation of wear debris**.
During *in-vivo* conditions, the articulating surface of UHMWPE modifies its characteristics over time due to sliding and rocking motions of the counterbearing femoral component against it, making the CA a time-varying quantity. Consequently, the CA is dependent upon the dynamic deformation response of the material, the changes of which produce a significant effect on the CP at the contact surface of UHMWPE. From the modelling viewpoint, it is important to faithfully estimate both CA and CP at the UHMWPE surface since the volumetric wear calculated through any algorithm based on Archard's law of wear relies on these quantities, as also described in section 1.1. From these observations, one can conclude that "time dependent" or "dynamic" inelastic deformations of UHMWPE are potentially very important to consider when conducting computational wear analyses.

Simple mechanical tests (i.e. compression, tension, and shear flow tests) coupled with SEM and SAXS techniques have demonstrated that the anisotropy generated within UHMWPE as a result of inelastic deformations is due to molecular chain rearrangements occurring in both amorphous and crystalline phases (Lin and Argon, 1994). Furthermore, *in vivo* pin-on-disk tests (Turell et al., 2003) carried out on UHMWPE samples have proved that sliding along a principal direction leads the polymeric chains to realign

along that direction, resulting in material hardening and low wear rates. Conversely, rupture of polymeric chains occurs when a secondary motion orthogonal to the principal sliding direction is introduced, resulting in high wear rates (Wang, 2001).
These experimental observations have motivated the **second line of focus that concerns the study of the role of transient and permanent polymer chains realignment during multidirectional sliding and its potential correlation to wear**.
For this purpose, the concept of anticoaxiality between the stress and the strain tensors (Vianello, 1996a; Menzel, 2007), which indirectly quantifies molecular chain realignment, was embedded within the framework of the most advanced constitutive theory for UHMWPE that accounts for its complex non-linear behaviour (Bergström and Bischoff, 2011).

1.3 Outline of the PhD work

The initial part of the project has been spent on reviewing the relevant literature to lay down the basis of the computational studies presented herein.
The initial step of research was dedicated to the study of the anatomy of a natural knee, the pathologies that lead a patient to undergo knee surgery, and the causes for arthoplasty revision surgery. These topics shed light on the physiological environment and the operating conditions in which the UHMWPE component of a TKR is required to operate. These are known to chemically alter its mechanical properties due to changes in lubrication conditions, kinetics, and kinematics.
The next step was the study of the chemical structure of UHMWPE together with the common techniques employed to improve its mechanical properties. Techniques such as sterilization and thermal treatments modify the chemical microstructure of UHMWPE resulting in a crosslinked material with different mechanical properties when compared to a virgin UHMWPE. This step was crucial in order to understand part of the constitutive framework of the most advanced mechanistic models for UHMWPE. The remaining part was covered by investigating the micromechanical mechanisms of deformation acting on UHMWPE from small to large deformations. The manufacturing techniques of UHMWPE resins were also investigated as these are crucial in conditioning the physical properties of the finished product. These aspects are illustrated in chapter 2.

As previously discussed in section 1.2, inelastic deformations occurring at the articulating surface of the UHMWPE component in a TKR must be accounted for since they are linked to the kinetic quantity CP. As discussed earlier, CP is a critical input parameter used in computational wear algorithms and this is why it is legitimate to wonder whether accounting for creep and plastic deformations (and recovery) is important when developing numerical wear models and associated algorithms. The implications of this observation are manifold.

Therefore, the respective role of elastic, creep, and plastic deformations of a UHMWPE tibial insert under compression on the CA characteristics and associated kinematic and kinetic quantities such as deformation and CP has been investigated using different numerical techniques. This study was first approached through an experimentally based FE model replicating the mechanical characteristics of an AMTI knee wear simulator (Advance Mechanical Technology Inc., Watertown, MA, USA) under static conditions. Then, the same problem was further investigated through a series of tailored physical uniaxial compressive tests on commercially available UHMWPE unicondylar tibial inserts, which were computationally realised using both FE and MBD modelling. These studies are reported in chapter 3 and chapter 4.

These computational studies were based on simple constitutive assumptions. They considered the elastic, viscoelastic, and plastic deformations separately, resulting in a simplified approximation of the actual mechanical response of UHMWPE. Therefore, in order to account for all these mechanisms of deformation at the same time, and in order to improve our understanding of the relations between molecular chains realignment and multidirectional sliding, an advanced microstructurally based constitutive model of UHMWPE (Bergström and Bischoff, 2011) was implemented in a finite element code. This physics-based model has been used to study the effects of multidirectional sliding characteristics (i.e. sliding track shape, sliding velocity, and sliding distance) on the evolution of microstructural anisotropy of UHMWPE. These kinematic characteristics are generally reported to be correlated with wear rates (Dressler et al., 2011; Saikko et al., 2004; Fisher et al., 1994). Therefore, *in silico* pin-on-disk (POD) tests with a UHMWPE pin sliding over a CoCr counterbearing have been used as a basis for the explicitation of the mechanistic model's predictive capabilities. The constitutive framework of the model as well as the FE simulations are reported in chapter 5.

The numerical models presented herein have used a physics-based approach in describing/explaining the role of kinetics/kinematics quantities associated with multidirectional sliding and that of the evolution of anisotropy on the propensity to wear. This work lays down more solid bases towards the understanding of the wear mechanisms of UHMWPE components in TKRs when compared to purely phenomenological-based wear models by introducing a more mechanistic approach thanks to a microstructurally-motivated constitutive model implemented in a robust finite element framework. The implications of this work are discussed in chapter 6 where opportunities for further work are also highlighted.

1.4 Structure of the PhD thesis

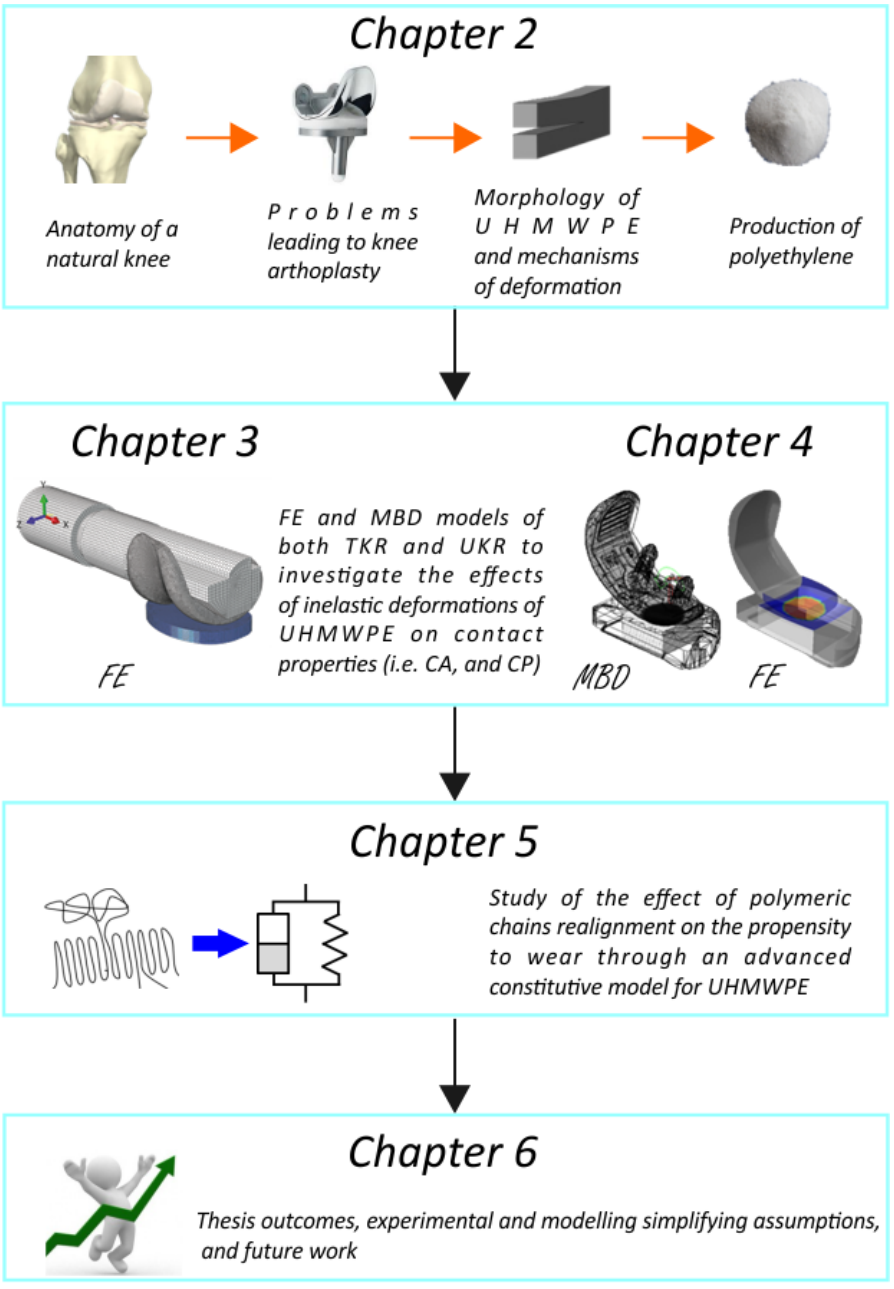

Chapter 2

Literature review on the UHMWPE for TKRs

In this chapter, the basic background information on the UHMWPE used in knee implants is provided. In particular, in order to gain a better insight into the physiological environment and the loading conditions under which the UHMWPE tibial insert operates, a natural knee, its biomechanics, and the pathologies that affect the functionality of a TKR are presented. Then, the morphology, micro-scale deformation mechanisms, and the most common methods employed to improve wear resistance of UHMWPE are discussed. A concise summary of the most common designs and materials for artificial knee joints is also provided.

2.1 The knee joint

2.1.1 Anatomy of the knee

The knee is one of the most complex existing joints in the human body as well as one of the most fragile since it can absorb a vertical force equal to nearly seven times body weight, but is very vulnerable to horizontal blows. The knee presents an highly nonconforming articulating surfaces that allows for extreme flexions up to 140 ° (Marieb and Hoehn, 2007). When the joint is not loaded, there is about 5 mm of laxity in the soft tissue structure surrounding the knee to enable complex rotations and relative sliding of the joint surfaces (Kurtz, 2009). The knee can be viewed as an assembly of three joints into one: the *femoropatellar joint* that is located between the patella and the lower end of the femur, and the two *tibiofemoral joints* that are positioned between the femoral condyles above the menisci (**Figure 2.1**).

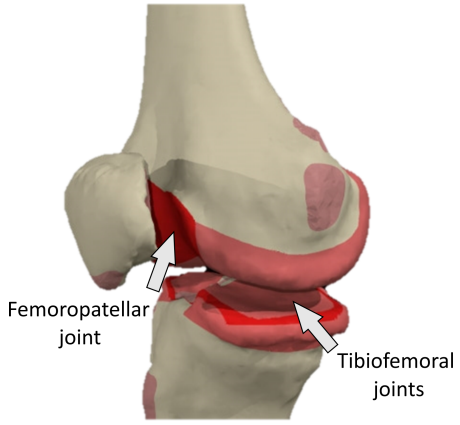

Figure 2.1: Lateral view of a right knee. The picture illustrates the three articular joints in a healthy knee. One joint is located between the patella and the femur, while the other two are located between medial and lateral condyles of both tibia and femur (source: http://www.anatomy.tv.)

The menisci play a crucial role to prevent the side-to-side rocking of the femur on the tibia, furthermore, they absorb shocks transmitted to the knee joint. The tibiofemoral joints act as a hinge, permitting flexion and extension. When the knee is partly flexed or extended, some rotation is still possible. The femoropatellar joint is considered a plane joint and during knee flexion the patella glides across the distal end of the femur. The knee cavity is partially enclosed by a capsule filled with synovial liquid, a fluid which acts as a lubricant; it is located only on the sides and posterior aspect of the knee covering the bulk of tibia and femur condyles. Anteriorly, where the capsule is absent, three broad ligaments −the patellar ligament flanked by the medial and lateral ligaments− run from the patella/distal end of the tight bone to the tibia/fibula below. These three broad ligaments merge imperceptibly into the articular capsule on each side (Marieb and Hoehn, 2007) (**Figure 2.2**-a).

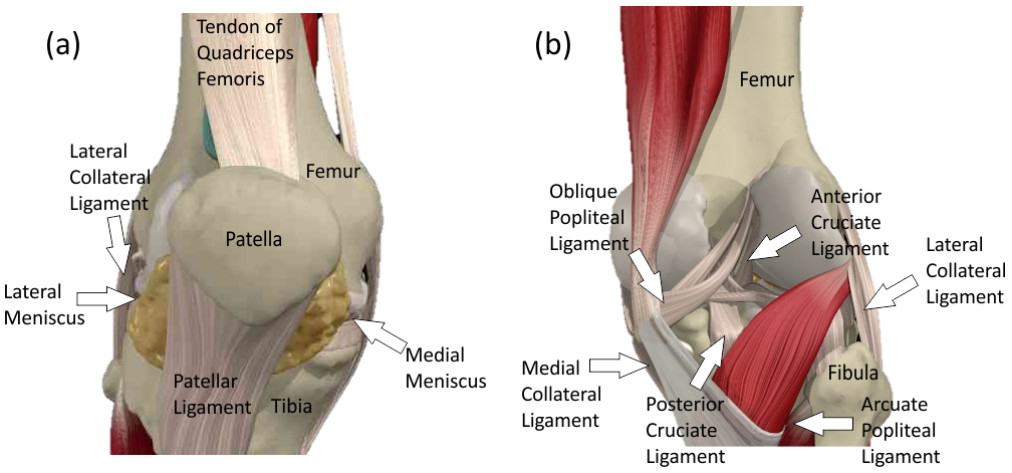

Figure 2.2: Inset (a) illustrates the anterior view of a right knee, while inset (b) the posterior view (source: http://www.anatomy.tv)

All three joint ligaments stabilise and strengthen the capsule of the knee (Marieb and Hoehn, 2007). The *tibial collateral ligaments* prevent lateral and medial rotations when the knee is extended, while the *oblique popliteal ligament* helps to stabilize the posterior aspect of the knee, and the *arcuate popliteal ligament* reinforces the joint capsule posteriorly.

The intracapsular ligaments are termed cruciate ligaments since they cross each other (**Figure 2.2**-b). The *anterior cruciate ligament* prevents forward sliding of the tibia on the femur and checks hyperextension of the knee. It is lax when the knee is flexed, and taut when is extended. On the contrary, the *posterior cruciate ligament* (PCL) prevents either backward displacement of the tibia or forward sliding of the femur.

2.1.2 Knee pathologies, intervention options, and arthoplasty revision surgery

The osteoarthritis and the rheumatoid arthritis are knee pathologies that in most cases, lead the patient to undergo knee surgery. Osteoarthritis leads to a total wear out of the cartilage at the joint articulation with consequent tissue inflammation and pain for the patient. The causes that trigger osteoarthritis might be attributed to factors such as a long and active life, injuries, obesity, and diabetes (Norman and Kress, 2003). Conversely, rheumatoid arthritis is a progressive disease where the immune system triggers an inflammation of the synovial fluid with the result of damaging the joint soft tissue (Kurtz, 2009). When it is not possible to alleviate the pain or restore the functionality of the knee for normal daily activities, and medication and/or physiotherapy are unsuccessful, partial or TKR is the only alternative left. The intervention options on the knee are listed below in order of increasing invasive character.

Tissue Resection: Knee implants should be avoided as much as possible in young patients because of the concern of the implant wearing out too quickly, therefore, resecting the natural knee tissues is substitutive and less invasive solution. For instance, the meniscectomy surgery removes part of the meniscal cartilage, while the osteomy removes part of the bone for the purpose of better redistributing the load on the knee.

Interpositional spacers: A spacer replaces the worn meniscal cartilage in order to avoid the bone-on-bone contact.

Hemiarthoplasty: It is a surgical technique used to correct the varus or valgus (see appendix B.2) deformity by inserting a tibial insert to replace the worn part of the joint, thus restoring the normal stability of the knee (MacIntosh and Hunter, 1972).

Unicompartimental and bi-lateral arthroplasty: This option is adopted when one of the two condyles is damaged. The technique requires a limited resection of both tibia and femur in order to leave enough bone stock for a subsequent TKR if needed.

Primary TKR (tri-compartimental knee arthroplasty): This surgery resects a considerable amount of bone, which include part of the intercondylar region of femur and tibia.

Revision: A more extensive knee implant than a standard TKR is required. For instance, if a patient undergoes a unicondylar knee replacement (UKR), the revision surgery will require a TKR. However, a revision procedure reduces the bone stock and carries further risks of infection and related complications. Therefore it is desirable to have an implant with high longevity.

2.1.3 Causes for arthroplasty revision surgery

The TKR can be revised for factors related to both implant and patient post-operation issues:

Wear: Two bodies in contact subjected to relative motion will wear out, and in the case of UHMWPE, wear debris are built-up in the surrounding soft tissues, resulting in osteolysis (Casey et al., 2007). This is a process whereby macrophages attempt to remove the foreign wear debris from the body, and in so doing also reabsorb the natural surrounding bone stock.

Loosening: The mechanical fixation of the implant interface fails, which can be either the bone-cement or the implant-cement interface (Barbour et al., 1997).

Dislocation and subluxation: These articulating issues take place in either the femoropatellar or the tibiofemoral joints when the soft tissue constraint is inadequate, or implant components are malpositioned (Cameron and Hunter, 1982).

Instability: The knee is inherently unstable depending on the extensive surrounding soft tissue (ligaments and muscles) to provide stability. If this soft tissue is damaged, then the internal kinematics of the knee becomes under-constrained (Waslewski et al., 1998).

Patellar complication: The patient feels a pain around the patella, and a common problem is a poor patellar tracking due to the fact that the patella has not been resurfaced (Strickland, 2009).

Mechanical fracture: The implant can experience a structural failure *in-vivo*.

Limited Implant functionality: If implant components are misplaced or ligaments are not balanced, the range of mobility of the knee might reduce with the consequence of restricting the normal daily activities of the patient (Kim et al., 2004).

Infection: A bacterial infection of the implant inevitably leads to the removal of the implant.

Pain: Post-operative pain is not a standard parameter, and mainly depends on the sensitivity of the patient.

2.1.4 Designs and materials for TKRs

TKRs refer to the design family of endoprostheses where the entire distal surface of the femoral condyles is resurfaced, and the proximal surface of the tibial condyles is resected. These two artificial surfaces are articulated together through a UHMWPE bearing. Total (bicondylar) knee replacements can be classified as *cruciate sparing* or *cruciate sacrificing* depending on whether the PCL was removed during the implantation of the UHMWPE tibial insert (Kurtz, 2009). The most common designs for knee prostheses use either the fixed or the rotating platforms. The Fixed-Bearing Knee implants (**Figure 2.3**-a) permit only motions of flexion and extension of the knee since the UHMWPE inlay is rigidly fixed to the metal backing plate on the tibia. Conversely, the Rotating-Bearing Knee implants (**Figure 2.3**-b) mimic the motions of a natural knee by permitting the implant to rotate, twist, flex and extend since the polyethylene insert that articulates against the femoral component loose its fixation to the metallic back-up plate. According to McEwen et al. (2001), this design would generate lower internal stresses and wear in UHMWPE .

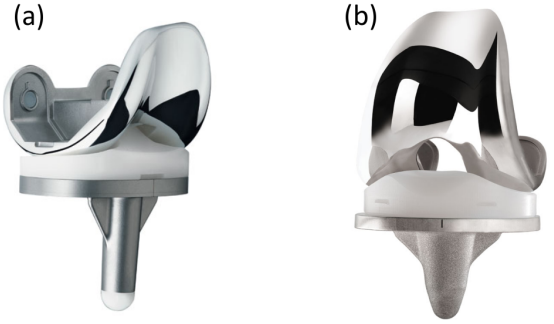

Figure 2.3: (a) Sigma ® Fixed-Bearing Knee implant and (b) Sigma ® Rotating-Bearing Knee implant (DePuy ® Synthes, Warsaw, IN, USA)

The standard coupling for TKRs is the metal-on-polyethylene (MoP) bearing. Although polyethylene presents a good resistance to impact, wear fatigue, and biocompatibility, the generation of wear particles due to the *in vivo* accumulated damage and cyclic contact stresses at the articulating surface remains the primary concern in TKRs (Pruitt, 2005). However, once implanted, the MoP gives immediate pain relief and restoration of mobility for the patient (Kurtz et al., 1999). At present, more advanced bearing couples with low contact friction such as ceramic-on-ceramic or metal-on-metal (Renò and Cannas, 2006) are used in total hip replacements (THR), but these are not suitable for TKRs since TKR joints are less conform than THR joints. Furthermore, the hip is constantly subjected to compressive loads by the musculature, which is not the case for the knee considering that tibiofemoral lift-off may occur and generate impact loadings. The conformity level of TKR implants is conditioned by the geometry of the UHMWPE tibial surface in contact with the double convex surface of the femoral condyles. A tibial insert with a flat surface leads to a non-conform contact, resulting in high stresses that tend to promote damage mechanisms such as wear and delamination. A partially flat tibial insert reduces the stresses in the material by increasing the articulating CA, which lead to a more restricted articulating motion (Walker and Hsieh, 1977). However, the susceptibility of the TKR implant developing three-body abrasive wear increases with the degree of conformity of the TKR (Walker and Hsieh, 1977).

Generally, the femoral component of TKRs is made of a cobalt-chrome-molybdenum (Co-Cr-Mo) alloy, although titanium alloys have shown to possess higher strength, biocompatibility, and resistance to corrosion (Long and Rack, 1998). UHMWPE tibial inserts are mounted on a metal tray that is made of either a Co-Cr-Mo alloy or titanium in order to get a stiffer backing. The metal tray is fixed to the tibial bone by press-fitting or cementation.

2.2 Molecular structure of UHMWPE and micro-scale mechanisms of deformation

2.2.1 Morphology of UHMWPE

Polyethylene possesses the simplest structure of all commercial polymers, and is also a very versatile material since is widely used to produce goods such as shampoo bottles, grocery bags, children's toys, and even bullet proof vests. This material is generally classified as a linear (not branched) thermoplastic homopolymer (Kurtz, 2009). The UHMWPE chain presents a structure of repeated ethylene units made of carbon and hydrogen molecules (**Figure 2.4**), where C−C and C−H chemical bonds are covalent, while neighbouring molecular chains are held together by van der Waals forces (Lin and Argon, 1994). UHMWPE presents two transition temperatures; the glass transition temperature (T_g) at $-120\,^{\circ}$C, and the melt temperature (T_m) at $137\,^{\circ}$C. Below $-120\,^{\circ}$C, it behaves like a brittle material since there is no thermal energy available for chains to move, while above $137\,^{\circ}$C it looses its solid state since crystallites start to melt.

$$[C_2H_4]_1 - [C_2H_4]_2 - [C_2H_4]_3 \ldots [C_2H_4]_n$$

Figure 2.4: The degree of polymerization is indicated by n, which is the number of ethylene repeat units in a UHMWPE molecular chain. Generally, the value of n for UHMWPE is 200 000 (Kurtz, 2009).

A single UHMWPE molecular chain can be seen as an entangled string about a kilometre long with internal stored energy, which becomes mobile at elevated temperature. In the molten state, polymer chains are in a random coil configuration (entangled), and as the melt cools down below the melt temperature, the molecular chain tends to rotate about the C−C bond to form chain folds, with the result of minimising the free energy of the system. The chain folding process creates local regions of ordered molecular chains (crystalline lamellae) that are embedded within an amorphous matrix (**Figure 2.6**). Moreover, there is experimental evidence of a third partially ordered interfacial phase between crystallites and amorphous regions (Barron and Birkinshaw, 2008). The nature of the folded surface in UHMWPE is believed to lie in between two extremes theoretical models, the "adjacent re-entry" with either sharp (**Figure 2.5**-a) or loose folds (**Figure 2.5**-b), and the "random re-entry" (**Figure 2.5**-c) (Peacock, 2000; Flory, 1962). In the former model, molecular chains fold in regular 3-D arrays, while the latter model allows molecular chains to assume random spatial configurations on the fold plane before re-entering the lamellae (Lin and Argon, 1994).

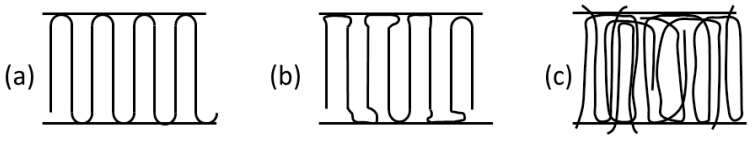

Figure 2.5: Adjacent re-entry model with sharp folds (a) and loose folds (b). Random re-entry model (c). Figure adapted from Young and Lovell (1991).

The physical and mechanical properties of polyethylene are governed by the relative portion of crystalline and amorphous phases. For instance, properties such as density and stiffness depend upon the degree of crystallinity, which is defined as the degree of structural order in a solid. Given that the crystalline phase is stiffer than the amorphous phase, the elastic modulus and yield stress of UHMWPE increase with increasing number of crystals (Kurtz et al., 2008). A single crystalline lamella of a conventional UHMWPE is about 10−50 nm thick and 10−50 μm long (**Figure 2.6**), while the gap between crystals is approximately of the order of 5−50 nm (Peacock, 2000; Kurtz, 2009; Sobieraj and Rimnac, 2009). A crystalline lamella is made of many single unit cells, which are entities that contains the minimum required information to build up a crystal. The polyethylene used for commercial products contains orthorhombic unit cells, where each side of the cell has a different length of 0.741 nm (a), 0.495 nm (b), and 0.255 nm (c) under unperturbed conditions, with angles of 90 ° between faces (**Figure 2.7**) (Das-Gupta, 1994; Lin and Argon, 1994). The zig-zag molecular chains are parallel to the *c*-axis of the orthorhombic cell (**Figure 2.7**).

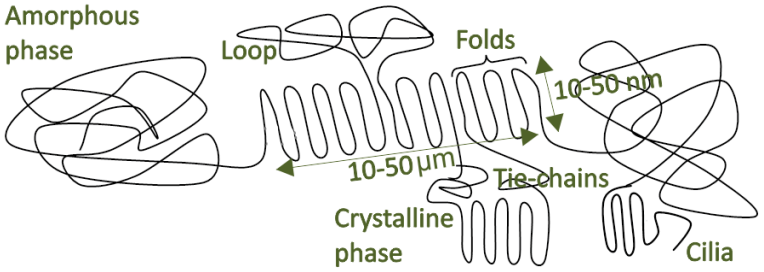

Figure 2.6: Schematic representation of the semicristalline structure of UHMWPE. Molecular chains in the amorphous region are continuous with those in the crystalline region through "tie-chains", "loops", and "cilia". Figure adapted from Kurtz (2009).

The connections between crystallites are of two types: direct "tie-chains" and entangled "loose loops" emanating from adjacent lamellae (**Figure 2.6**). They cannot be directly imaged, therefore, their existence and properties have to be extrapolated from the properties of the material. The term tie-chains includes all types of intercrystalline connections that transmit forces between crystallites. These physical links affect mechanical properties such as ductility, toughness, and modulus. Clearly, polyethylene would be a brittle material with low physical strength without the presence of tie-chains. It is postulated that only taut tie-chains are able to transmit stresses to crystallites, and the higher concentration of physical connections, the greater load they can carry. However, if the number of tie-chains is not enough to sustain the applied load, they start to break, and the load is then transmitted to adjacent tie-chains with the consequence of triggering a domino-like effect. Under these conditions, the material will break due to brittle failure across the width of the specimen considering that the strength of lamellae exceed the load-breaking capabilities of interlamellar physical connections (Peacock, 2000; Meyer and Pruitt, 2001).

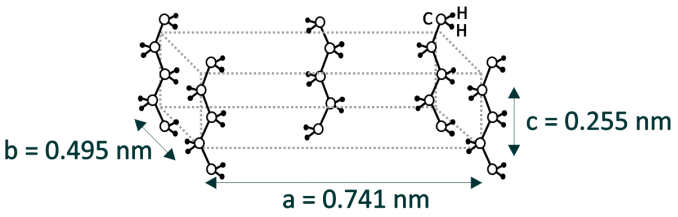

Figure 2.7: Spatial zig-zag configuration of molecules for the orthorhombic unit cell of polyethylene. Figure adapted from Argon (2013) and Das-Gupta (1994).

2.2.2 Micro-scale deformation mechanisms of UHMWPE

The concept of crystallographic defects, which was initially proposed for crystalline metals, has also been used to describe deformation mechanisms of polymers (Lin and Argon, 1994). In addition to point defects such as vacant lattice sites, substitutional and interstitial single atoms, the lamellar crystals contain more complex defects like chain ends, chain twists, kinks, and dislocations (Peacock, 2000; Lin and Argon, 1994). The deformation of crystal lamellae occurs for crystallographic slip, mechanical twinning, and stress-induced martensitic transformation, although the last two are present to a lesser extent. These mechanisms of deformation occur if one assumes a particular structure of UHMWPE where crystal lamellae are separated each other by layers of amorphous phase, and held together by physical connections (Lin and Argon, 1994; Bowden and Young, 1974). Based on this morphology, three mechanisms of deformation occurring in the amorphous phase, which is associated to lamellar deformations, have been hypothesised; interlamellar shear, interlamellar separation, and lamella-stack rotation. In addition, the inelastic response of UHMWPE initially occurs in the amorphous phase because its glass-transition temperature is far below typical room temperature (Kurtz, 2009), resulting in lower modulus and strength when considering the crystalline phase. At high strains, the deformation mechanisms of crystal lamellae and the shear of the amorphous matter take place simultaneously (Lin and Argon, 1994).

2.2.2.1 Deformation in the crystalline phase of UHMWPE

A crystallographic slip is the process by which a dislocation moves, resulting in plastic deformation of the material. In addition, this mechanism produces a change in the shape of crystals but not in the volume, which remains constant. By definition, a dislocation is an irregularity in the crystal structure, and in polyethylene the irregularities emerge around chain ends (Lin and Argon, 1994).

Crystallographic slip happens on particular sets of crystallographic planes that are known as *slip planes*, and along a specific set of directions within these planes that are called *slip directions*. The combination of *slip plane* and *slip direction* identifies the *slip system*, which is normally reported in Miller index (Ashcroft and Mermin, 1976). The intercepts of a plane are identified on the three crystallographic axes, and for a surface parallel to one axis the intercept is ∞. The intercepts are then expressed in fractions of the crystal parameters. The Miller index are obtained by calculating the reciprocal of these fractional intercepts, which are reduced to integral proportions. These numbers, which are enclosed in round brackets without commas (hkl), identify a crystal plane (Lapedes, 1978). For instance, the Miller index (001) refers to a plane orthogonal to direction 1. Moreover, the curly bracket {hkl} represents a family of slip planes, while the square bracket [hkl] and the angle bracket <hkl> stand for a single slip direction and a family of slip directions, respectively (William, 1995).

In polyethylene, the slip plane is restricted to that containing the chain direction (i.e. (hkl)), since the covalent bonds in the chain backbone do not break easily (Galetz and Glatzel, 2010). Only the slip occurring in directions parallel and perpendicular to the chain direction [001] is considered. When the slip direction is parallel to the chain axis c, the deformation is called "chain slip" (**Figure 2.8**-a), while the deformation is referred to as "transverse slip" when the slip direction is perpendicular to c (**Figure 2.8**-b). In orthorhombic polyethylene, the chain slip systems are (100)[001] and (110)[001], while the transverse slip systems are (100)[010] and (110)[1$\bar{1}$0] (**Figure 2.9**), where the overbar symbol stands for a minus sign (Allan and Bevis, 1980; Lin and Argon, 1994).

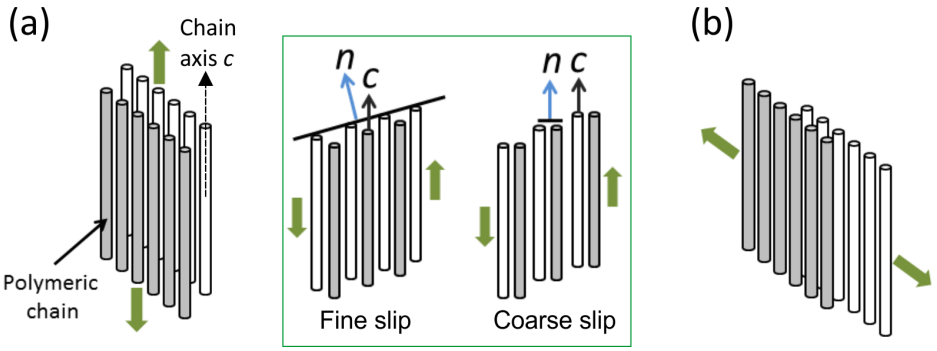

Figure 2.8: Mechanisms of deformations for chain slip (a) and transverse slip (b). The former mechanism can occur for either fine slip or coarse slip. Figure adapted from Lin and Argon (1994).

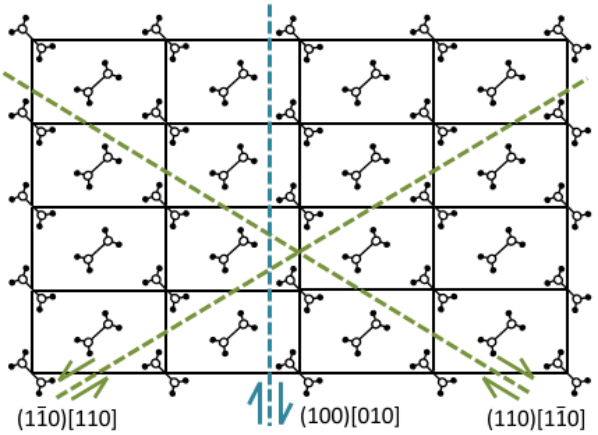

Figure 2.9: Schematic highlighting the transverse slip systems in polyethylene. The unit cell is projected along the chain axis. Figure adapted from Bowden and Young (1974).

The presence of dislocations such as screw and edge, reduce the shear strength of semi-crystalline materials when compared with the shear strength of perfect crystals. Therefore, crystallographic slip is mainly governed by the resistance to the motion of dislocations on the slip plane. Shadrake and Guiu (1979) calculated the energy required for a specific slip system to become operative during deformation of polyethylene at room temperature. They found that the deformation of polyethylene is mainly governed by the motion of screw dislocations along the chain axis (i.e slip system (100)[001])(Lin and Argon, 1994). Transverse slip systems possess higher activation energy than chain systems. Screw dislocations possesses lower activation energy than edge dislocations. The relationship between the direction of the applied force and the slip system can be approximated using the critical resolved shear stress (CRSS) (Lin and Argon, 1994).

The likelyhood of a slip system to become active increases with the CRSS. Once the CRSS is exceeded, the motion of dislocations on the slip plane in the slip direction separates the two parts of the crystal.

The same macroscopic deformation for chain slip can be obtained either for fine slip or coarse slip (**Figure 2.8**-a). In the former mode, a small amount of slip occurs on a large number of planes, and only the normal **n** of the lamellar plane rotates with respect to the chain axis **c**. In the latter mode, a large amount of slip occurs in a bunch of planes, where both **n** and **c** rotate together. The coarse slip occurs mainly at large deformations (Hinton et al., 1974).

Twinning is a common mechanism of plastic deformation in metals, occurring at low temperatures. This deformation mechanism, like in the case of a crystallographic slip, permits a crystal to change its shape but not its volume. Twinning involves the shear of only a part of the crystal, which reorients relative to the unsheared part. The twinning plane is the region of the crystal that separates these two contiguous parts. In UHMWPE, the occurrence of twinning deformation in the {310} and {110} planes for both solution-grown and melt-crystallized polyethylene was demonstrated by using a X-ray diffraction technique (Eyerer et al., 1985; Bowden and Young, 1974). The amount of deformation is measured through the rotation around the chain c axis in the direction [001] of both a and b crystal axes. The {110} and {310} twinning planes produce a lattice rotation of 67 ° and 55 °, respectively (**Figure 2.10**).

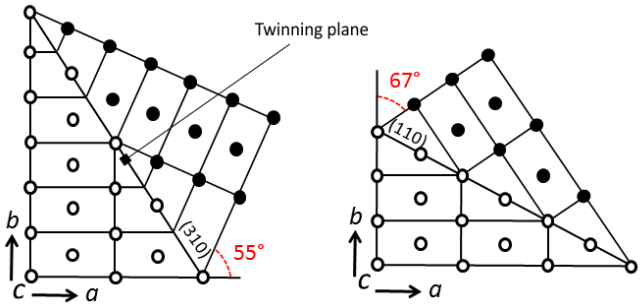

Figure 2.10: Twinning deformation occurring in {110} and {310} planes with 67 ° and 55 ° rotation around the chain axis (normal to the page) c, respectively. Open circles refer to the untwinned crystal. Figure adapted from Burbank (1960).

The existence of a shear transformation in the deformed bulk polyethylene that involves a change in the crystal structure occurring in a short-range diffusion has been demonstrated using the wide-angle X-ray diffraction (Cowking et al., 1968). When the polyethylene is deformed, a small amount of orthorhombic unit cells (**Figure 2.7**) turns into monoclinic (**Figure 2.11**). The **martensitic transformation** occurs through the shear in a direction perpendicular to the chain direction [001] (Seto et al., 1968). In addition, an orthorhombic to hexagonal unit cell (figure not reported) transformation has been observed for UHMWPE under specific pressures and temperatures (Lin and Argon, 1994).

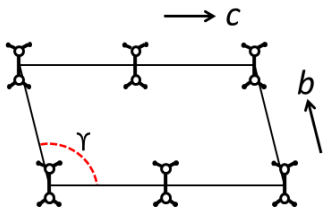

Figure 2.11: Monoclinic unit cell of polyethylene. In the martensitic transformation, the angle γ between directions b and c becomes different from 90 °. Figure adapted from Lin and Argon (1994).

2.2.2.2 Deformation in the amorphous phase

Interlamellar shear includes the shearing of amorphous material between crystal lamellae through an applied driving force parallel to the surface of the lamella (**Figure 2.12**-a).

The mechanism of **interlamellar separation** accounts for an increase in the distance between lamellae because the interlamellar amorphous phase is stretched by an applied tensile force (**Figure 2.12**-b).

The **lamella stack rotation** is described as a deformation mechanism in which blocks of 3 to 10 lamellae rotate in order to compensate the distortion in surrounding amorphous regions caused by deformation (**Figure 2.12**-c). However, the pure rotation itself does not produce any strain in the material, but it rather accompanies deformations such as interlamellar shear (**Figure 2.12**-a), interlamellar separation (**Figure 2.12**-b), and intralamellar chain slip (**Figure 2.10**-a).

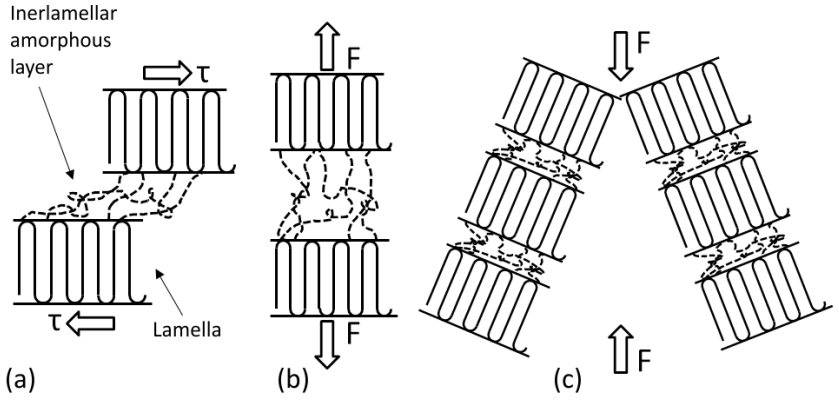

Figure 2.12: Deformation mechanisms occurring in the amorphous phase of UHMWPE: (a) Interlamellar shear, (b) interlamellar separation, and (c) lamella-stack rotation. The applied shear and vertical force are τ and F, respectively. Figure adapted from Lin and Argon (1994).

2.3 Techniques to improve UHMWPE's wear resistance

In the past, UHMWPE components of TJRs were sterilised in air using γ radiation as the process was economically advantageous. However, the exposure of UHMWPE to γ radiation in the presence of an oxygen source embrittles the material by oxidative degradation (Sobieraj and Rimnac, 2009). This mechanism is known as post-irradiation oxidative aging, and reduces the wear and fracture resistance of UHMWPE. In order to lessen the oxygen supply, new sterilization techniques such as the γ irradiation in either vacuum-packaging or inert-gas packaging, have been used instead.

The resistance of UHMWPE to wear damage can be enhanced by applying a high-dose of ionising radiation to the amorphous region (crosslinking), followed by heat treatments (Kurtz, 2009; Sobieraj and Rimnac, 2009). The applied irradiation creates chemical crosslinks among molecular chains by forming both hydrogen and free radicals, where the latter are simple macro-molecules with an unpaired electron. For crosslinking to occur, free radicals needs to be nearby polyethylene molecules in the first place, and secondly polyethylene molecules should be mobile. A covalent bond is formed between polyethylene molecules as soon as nearby free radicals reach one another (**Figure 2.13**). This process alters the chemical structure of UHMWPE, and the extent of crosslinking is proportional to its absorbed dose of irradiation (50 to 105 kGy) (Kurtz et al., 2008; Sobieraj and Rimnac, 2009).

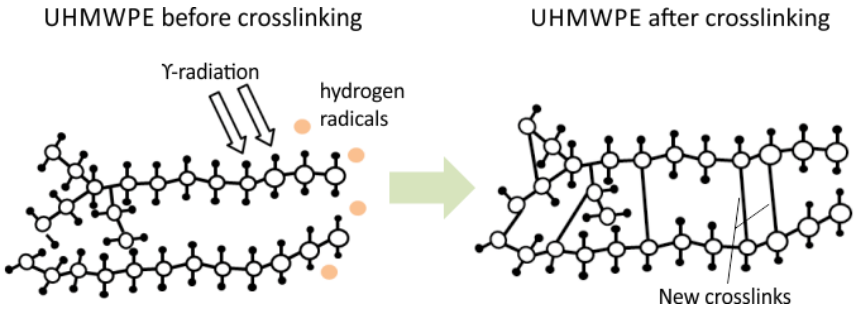

Figure 2.13: Schematic illustration of UHMWPE crosslinking.

Nevertheless, not all free radicals recombine with each other during the irradiation process, and those left remain trapped in the crystalline phase. These radicals react with diffuse oxygen to form peroxy radicals ($R-O_2$, where R stands for radical) that attack other polyethylene chains, hence triggering an oxidative cascade that ends with oxidative embrittlement, and reduction of mechanical properties (Renò and Cannas, 2006). The role of heat treatments such as annealing and re-melting, is to improve the material resistance to oxidative embrittlement by quenching the free radicals trapped in the crystalline phase. Heat treatments at temperatures above 137 °C melt the crystals, and the previously trapped free radicals are now available to form new crosslinks. However, the re-melting process causes a reduction in the size of UHMWPE crystals that is highly detrimental to its mechanical properties. A possible remedy to this problem, is the sequential irradiation and annealing at a temperature comprised between 130 °C and 136 °C, which reduce the amount of free radicals without remelting the material, and do not induce substantial changes of crystallinity.

The repeated irradiations of 30 kGy each, leave fewer and fewer free radicals in the material in such a way that the annealing step is more effective at quenching the free radicals left. In addition, a further way to reduce the issues related to the post-irradiation melting is by incorporating an antioxidant such as vitamin *E* within UHMWPE, which is capable of consuming free radicals that do not form crosslinks (Renò and Cannas, 2006). The crosslinked UHMWPE with vitamin *E* presents the same wear resistance as that of a simple irradiated and post heat-treated UHMWPE, but with increased elongation to break, toughness, oxidative stability, resistance to delamination, and resistance to fatigue cracks (Renò and Cannas, 2006; Sobieraj and Rimnac, 2009; Takahashi et al., 2013).

2.4 Production of UHMWPE resins

The fabrication of conventional UHMWPE for joint implants requires three basic steps. The UHMWPE is polymerised from ethylene gas through the Ziegler-Natta process, and the product of the reaction is a resin powder. This resin powder is consolidated into a semi-finished product like a rod or a sheet that is then machined into a final shape. In case of direct compression molding, UHMWPE is directly consolidated from the powder to its final shape without further machining (Kurtz, 2009).

2.4.1 Polymerization of UHMWPE

The Ziegler-Natta process requires the presence of ethylene (reactive gas), hydrogen, and titanium-tetra-chloride (catalyst) in order to polymerize UHMWPE. The polymerisation occurs at a temperature comprised between 60 °C and 100 °C within a solvent used for mass and heat transfer (Keller, 1979). Since these chemical compounds are volatile and highly dangerous, the polymerisation must be conducted in a specialised production plant. The catalyst is key in the synthesis of UHMWPE, and a great effort has been put over the years to reduce the presence of impurities in it. These resins are divided into type 1, type 2, and type 3 depending on their molecular weight and producer. Type 1−2 refer to Ticona resin GUR 1020 (2−2.5 x 10^6 g/mol) and GUR 1050 (5.5−6 x 10^6 g/mol)(Ticona/Celanese-Plant, Florence, Kentucky, USA), while type 3 refer to Basell polyolefins resin 1900H (2−4 x 10^6 g/mol, now discontinued) (Kurtz, 2009). The first digit after the acronym GUR stands for the loose bulk density of the resin, the second indicates the presence “1” or absence “0” of calcium stearate that is believed to cause oxidation in UHMWPE, and the third is the average molecular weight of the resin. The fourth digit refers to an internal code designation.

2.4.2 Conversion from UHMWPE powder to consolidated semi-finished products

The consolidation phase of the resin powder takes place at high temperature and pressure due to the low ability of the UHMWPE melt to flow, therefore, common thermoplastic techniques such as injection molding, screw extrusion, or blow molding cannot be used with it. Instead, the resin powder is treated by using compression molding and ram extrusion as will be explained in more detail, later in this section (Haasen et al., 1997). The right combination of temperature, pressure, and time to obtain the resin powder consolidation is generally proprietary and therefore not in the public domain. The consolidation mechanism is for self-diffusion, and the kinetic of intergranular diffusion is supported by close proximity of surfaces at high pressure, while the chain motions is promoted by the high temperature. This process requires a long enough time to allow polymeric chains to migrate across boundaries. To visually inspect the structure of UHMWPE, particularly grain boundaries, techniques such as optical and scanning electron microscopy (SEM) can be used (Kurtz, 2009).

In **compression molding**, the UHMWPE powder resin is placed between two oil-heated platens in a sheet-like mold (i.e. 1 x 2 m in size), and is compressed by using a hydraulic actuator located at the basement of the rig. The conversion process lasts for 24 hours due to the low thermal conductivity of UHMWPE. Moreover, a long processing time is necessary to maintain slow and uniform heating and cooling rates throughout the entire UHMWPE sheet. The compression is carried out within a clean room to prevent chemical contamination from external agents.

In the **ram extruder**, the UHMWPE powder is fed into a powder supply, and subsequently is ramped down inside an extruder that includes a hopper to access the heating-chamber, a horizontal hydraulic ram, a heated die, and an outlet. Inside the extruder, the UHMWPE is pressed by both ram and back pressure of the melted UHMWPE that is generated from the friction between the melt and the die wall during the horizontal sliding of the melt toward the outlet. Beyond the outlet, the melt is slowly cooled down in a series of electrical heating mantles. The productions rates (mm/minute) depend upon the diameter of the rod (20 to 80 mm) that consequently affects the time of cooling. The ram extrusion of medical-grade UHMWPE occurs in a clean room environment. However, semi-finished products can also be obtained by isostatic pressing and direct compression molding (DCM). These techniques are no any discussed further.

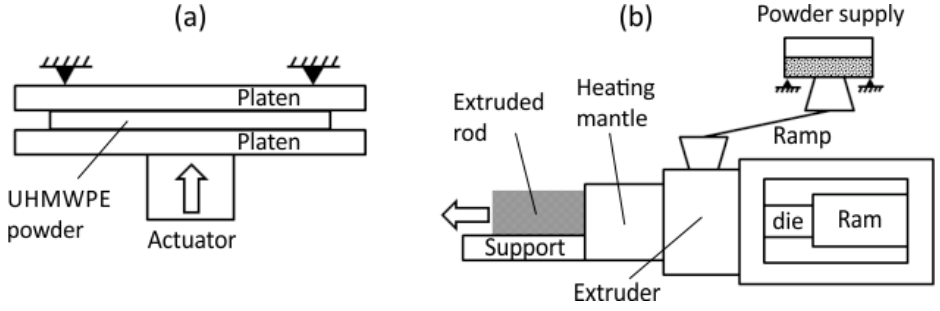

Figure 2.14: Schematic illustration of the compression molding press (a), and the ram extruder (b).

However, studies have reported a difference in the morphology and fatigue crack propagation behaviour of UHMWPE when is subjected to either ram extrusion or compression molding. Compression molding leaves the structure of UHMWPE isotropic, while its morphology varies in function of the distance from the centerline when ram extruded (Feldman and Hui, 1997).

Chapter 3

FE modelling of the mechanical behaviour of UHMWPE - Part 1

As mentioned in section 1.3, both chapter 3 and chapter 4 report computational studies which provided a novel insight into the relative contributions of creep and plastic deformations to contact area (CA), and so contact pressure (CP). As it will be discussed in the following introductory section, CP is a critical input parameter used in computational wear algorithms and it is therefore critical to account for creep and plastic deformations (and recovery) when developing numerical wear models and associated algorithms. The significance of creep deformations on CP is our main working hypothesis. Moreover, in these chapters it is shown that finite element (FE) and multi-body-dynamics (MBD) models featuring relatively crude constitutive laws can provide results in good agreement with experimental measurements.

3.1 Introduction

Characterising the mechanics of engineered biomaterials is essential in order to understand their clinical performance *in-vivo*. Physical testing provides valuable data on true material performance, while computational models provide a framework for encapsulating this data in a material model and using it for other applications, such as *in-silico* testing of new geometries or exploration of more complex physiologically representative loading conditions. Typically, experimental data is used to inform, develop and fit a constitutive law of a new material, which is essentially a set of mathematical equations relating stress to strain. This requires accurate and appropriate data using suitable experimental methods that captures the mechanical behaviour of interest under relevant (physiological conditions) under specific conditions (e.g. range of deformations, strain rates, time scales). The quality of any resulting model is directly dependent upon the quality of the underlying data.

In the field of orthopaedic implants the assessment of the performance of conventional MoP devices is of particular interest. Although MoP is an established technology, the composition of the polymers in use has evolved over the years, with improved variants of UHMWPE and new developments such as the use of cross-linked and anti-oxidant enriched polymers (McKellop et al., 1999). Furthermore, the theories employed to predict wear have often relied on a simplified relationship with contact pressure and total sliding distance (Archard, 1953). Recently, however, new evidence suggests that wear of UHMWPE is more highly dependent on contact area and the specific articulation path (Dressler et al., 2011; Mazzucco and Spector, 2003; Strickland et al., 2012). Because of these continuing advances, there is an on-going need to characterise experimentally these new variations of UHMWPE and develop improved simulation strategies, such as wear, using predictive models that more fully recreate *in-vivo* loading scenarios or at least estimate the lost fidelity when aspects like plasticity, creep, and viscoelasticity are ignored.

In clinical use, polymers are subjected to high compressive loads, often in excess of the elastic response range of the material. For instance, instrumented *in-vivo* studies have reported loads at the hip in excess of eight times body weight (BW) (Bergmann et al., 2001) and at the knee in excess of six times BW (D'Lima et al., 2008). These significant loads which produce inelastic deformations have the potential to result in long-term alterations to the polymer microstructure which could in turn modify its wear properties. Non-irradiated pre-compressed UHMWPE samples have been shown to wear at a lower rate than non-compressed specimens (Lee and Pienkowski, 1997).

The dynamic viscous behaviour of UHMWPE components are also important when investigating long-term wear because the associated surface re-modelling has been found to be a confounding factor when attempting to estimate linear or volumetric wear *in-vivo* using medical imaging (Isaac et al., 1996; Kabo et al., 1993). The resulting depth of indentation in a polymer component −also called penetration− is often used as a direct surrogate for wear in the clinical community; however penetration is the combined result of creep, plastic deformations, as well as material erosion. Creep is the phenomenon by which a solid body subjected to a constant force deforms over time. In theory, if the load is removed creep deformations are recoverable provided one waits sufficiently long enough. Creep is therefore distinct from plasticity where plastic deformations are not recoverable and are permanent.

The effect of creep and plastic deformation in orthopaedic devices *in-vivo* has been recognised since the earliest follow-up studies on hip implants (Charnley and Cupic, 1973), and has been shown to vary considerably depending on *in-vivo* conditions (Lavernia et al., 2001). Therefore, understanding the shorter-term (transient) response characteristics of new biomedical polymers, as well as the longer-term adaptations, is important for future medical device design, particularly if the goal is to predict wear. To this end, computational models have been widely used to incorporate creep effects in determining the wear of orthopaedic implants for both hips (Bevill et al., 2005; Penmetsa et al., 2006), and knees (Willing and Kim, 2009), partly because creep is believed to play an important role in driving sub-surface damage (Hailey et al., 1994), particularly in the period immediately following implantation. Transient creep effects have also been studied using a number of different methods (Abdelgaied et al., 2011; Deng et al., 1998). While investigators have continued to incorporate more advanced models, such as the microstructurally-based constitutive Three-Network-Model of UHMWPE (Bergström and Bischoff, 2011), there is no study that examines the benefits and potential trade-offs of increasing computational complexity. Specifically what is relative contribution of elastic, viscoelastic, and plastic behaviour in a model and similarly what accuracy is lost using a simplified rigid multi-body dynamics (MBD) analysis that has been used effectively for rapid wear simulation (Strickland and Taylor, 2009).

It appears that the respective mechanical contributions of creep and plasticity to inelastic deformations occurring in compression-loaded UHMWPE tibial components has not been studied in detail. These inelastic deformations are mainly the results of the contact forces exerted by the metal component over the polymer tibial insert. To simplify modelling, surface CP is often used as an indicative representation of the complex stress-fields both on and within the polymer. The effect of these mechanical forces can then be expressed in terms of a CP term which evolves with the kinematics of the artificial joint. It is straightforward to realise that creep and plastic deformations (as well as elastic deformations) are part of a time-dependent non-linear feedback loop mechanism. During regular or irregular cycling loading, at a given loading cycle, if creep deformations are not fully recovered, the next cycle might introduce incremental creep deformations which will accumulate with the previous ones. Ultimately, once this process has been repeated sufficiently, certain zones of the UHMWPE insert may be driven into the plastic regime. The transient nature of creep deformations is also likely to create transient contact areas between the femoral implant and the UMWPE tibial insert and therefore create transient contact pressures.

CP is a key variable in the FE approaches to simulate wear of UHMWPE components. These numerical techniques are generally based on Archard's law of abrasive wear (Archard, 1953), which uses CP and sliding distances as inputs to calculate the resulting wear volume. It is worth reiterating that these (naturally time-dependent) contact properties are intrinsically linked to the CA, which is in turn related to the extent of the external applied loads and any resulting deformation of the implant articulating surfaces. Inelastic deformation mechanisms such as creep and plasticity which do occur *in-vivo* are therefore critical because of their role in modifying the contact properties of the articulating surfaces, and in damage initiation and generation of wear. Furthermore, the wear behaviour of UHMWPE that has experienced creep, or plastic deformation in general, may differ from the virgin bulk material and must be analysed separately.

3.2 The role of viscoelastic and plastic effects in the creep behaviour of UHMWPE: An experimentally based computational study using an AMTI knee wear simulator

In this numerical study, a FE model of a AMTI knee wear simulator is used to characterise the respective role of elastic and inelastic deformations on variables such as CA, CP, and penetration depth.

3.2.1 Materials and Methods

3.2.1.1 Experimental Setup

An AMTI knee simulator (Advance Mechanical Technology Inc., Watertown, MA, USA) was used to create a simplified articulation using a size 3 right CoCrMo DePuy ® femoral component (DePuy Orthopaedics, Warsaw, IN) with a modified DePuy ® fixed bearing polyethylene insert secured in a CoCrMo Sigma modular tray. The proximal (articulating) surface of the insert was machined flat to provide a uniform 8 mm thickness that reduced confounding factors that may obfuscate measurements of contact area and penetration depth (Metcalfe, 2011). A constant vertical load (0.25, 0.5, 0.9, 1.8, 3.6 kN) was applied with flexion (0 ° to 30 °) for 1000 seconds with a 10 second ramp-up and ramp-down. The flexion was applied at 1 Hz about the distal sagittal femoral radius with no internal-external (I−E) rotation, anterior-posterior (A−P) translation or anterior-posterior (A−P) tilt. Valgus-varus (V−V) motion was constrained while medial-lateral (M−L) motion was left unconstrained. A description of these motions is reported in appendix B. To help identify the contact area, the proximal surface of the insert was coated with blue ink prior to each loading condition. The articulation of the femoral component against the ink on the insert was sufficient to preferentially remove the ink in the contact region, thus highlighting the contact scar. The experiment was conducted at room temperature and the surface was lubricated with water. It is important to note that the femoral component design has a constant radius within the applied flexion range, so the contact geometry should stay constant. The resulting deformation was determined by quantifying the penetration depth (PD) and contact area after each loading condition. The PD was defined as the maximum deviation from an idealised best fit of the proximal surface, and was measured using a contact profilometer (Zeiss Surfcom 5000, Maple Grove, MN, USA) and a three-dimensional (3D) laser scanner (Metron G2-24, Snoqualmie, WA, USA) with post-processing performed in Geomagic Qualify (Research Triangle Park, NC, USA). The CA was assessed through photographs showing the removal of toolmakers ink from the insert as well as images of the deformed inserts generated from the laser scanner. These images of CA were analysed using ImageJ (NIH, Bethesda, MD, USA). Recovery of the PD was also measured 1 and 2 days after the 3.6 kN loading cycle, (using the laser-scanner and profilometer). Although, the loading was intended to be symmetrical (i.e. 50 / 50 medial / lateral load split), this was not achieved due to pliancy in the flexion arm, resulting in asymmetry between the two condyles. Consequently care was taken to model this *in-silico*. The arm extends into the socket by about 65 mm, and has a diameter of about 35 mm **Figure 3.1**.

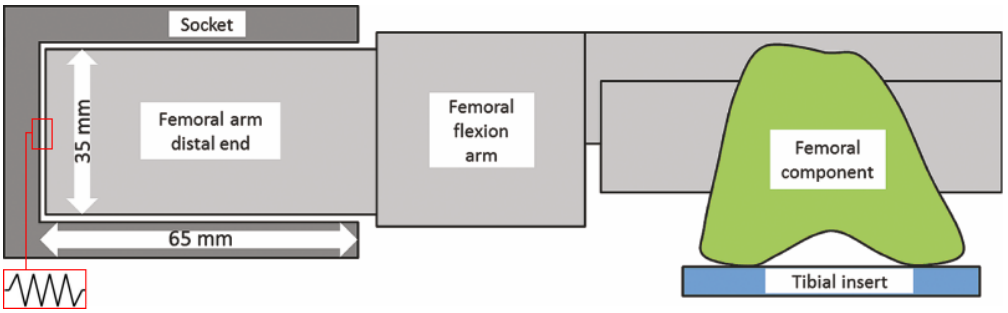

Figure 3.1: Schematic highlighting the geometrical details of the AMTI knee simulator arm placed within its socket together with the placement of the implant components (frontal view and not to scale).

The arm is actually undersized relative to the socket, hence a small amount of motion is possible and this can include translation and/or rotation, see **Figure 3.2**.

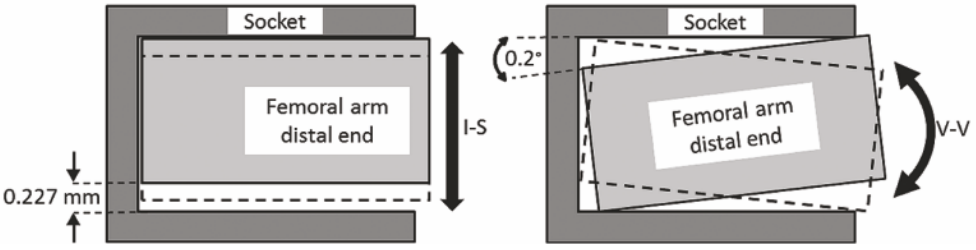

Figure 3.2: Schematic highlighting the (exaggerated) fitting tolerance of the femoral arm within its socket using the same frontal view as **Figure 3.1**. The type and magnitude of possible motions are indicated as I−S translation and V−V.

The motions can take place along the I−S and V−V directions, or in the A−P and I−E directions **Figure 3.2**. It is not possible to get either the maximum rotation at the same time as the maximum translation, nor the maximum translation in two directions at the same time (e.g. I−S and A−P directions) since the socket is circular in cross-section. One can work out the difference in sizes between the arm and the socket using basic trigonometry and measurements from the rig. The maximum possible V−V rotation is up to 0.2 °, and was measured via manual manipulation of the rig. This introduces a degree of measurement uncertainty and there is probably a station-to-station variability associated with this measurement. Because the arm extends inside of the socket by about 65 mm the difference between the arm and the socket diameters can be calculated as A−B = 65 mm * 0.0035 = 0.227 mm, see **Figure 3.1** and **Figure 3.2**. The possible translation motion is therefore 0.227 mm, which can be seen as about ± 0.11 mm relative to a fixed central reference point in the A−P and I−S directions. The motion in the medial-lateral (M−L) direction is different; it is governed by the pliancy of the mechanism locking the arm into the socket, and has been experimentally measured to have a range of 0.5 mm, i.e. ± 0.25 mm relative to a neutral fixed reference point.

3.2.1.2 Computational modelling

A FE model simulating an AMTI knee simulator articulating a PFC ®DePuy ® femoral component (size 3) on a flat UHMWPE tibial insert (size 3), under a series of monotonically increasing vertical loads was developed in Abaqus/CAE 6.11 (Dassault Systèmes Simulia Corp., Providence, RI, USA) according to the experiment described in the previous section (ABAQUS, 2012) (**Figure 3.3**).

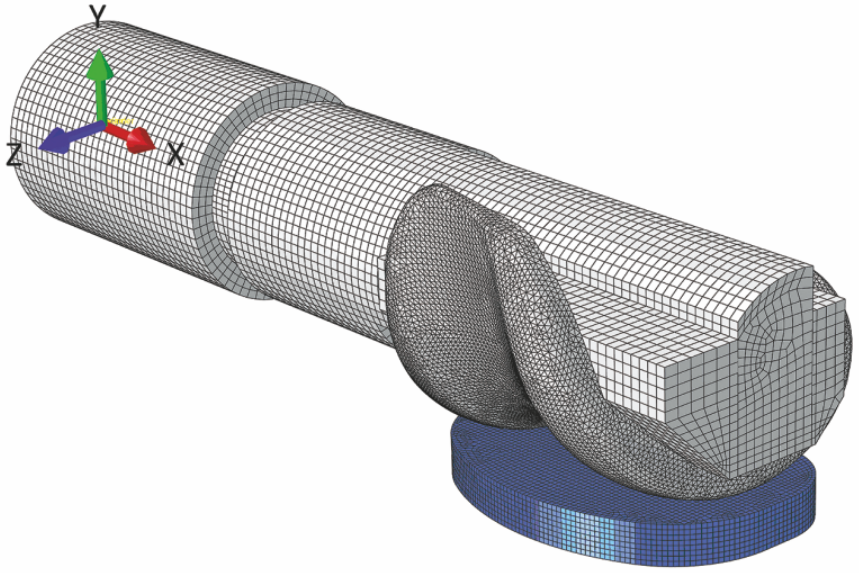

Figure 3.3: Perspective view of the finite element model of the AMTI knee simulator setup. Both tibial and femoral components were of size 3. The tibial insert was machined flat 8 mm thick.

From this generic FE model, three different FE models, each with a different material model for UHMWPE, were generated:

- **E-FE model** (Elastic-FiniteElement): isotropic linear elastic properties (Young's modulus of 575.5 MPa and Poisson's ratio of 0.46 (Kurtz et al., 1998).
- **EP-FE model**(ElasticPlastic-Finite Element): isotropic elastoplastic properties with kinematic hardening (Young's modulus of 575 MPa and Poisson's ratio of 0.46 and stress-plastic strain curve from Godest et al. (2002), 16 MPa yield stress), see **Figure 3.4**-a.
- **EV-FE model** (ElasticViscoelastic-Finite Element): isotropic viscoelastic properties featuring creep measured at 15 MPa compressive load (Reeves et al., 1998), see **Figure 3.4**-b.

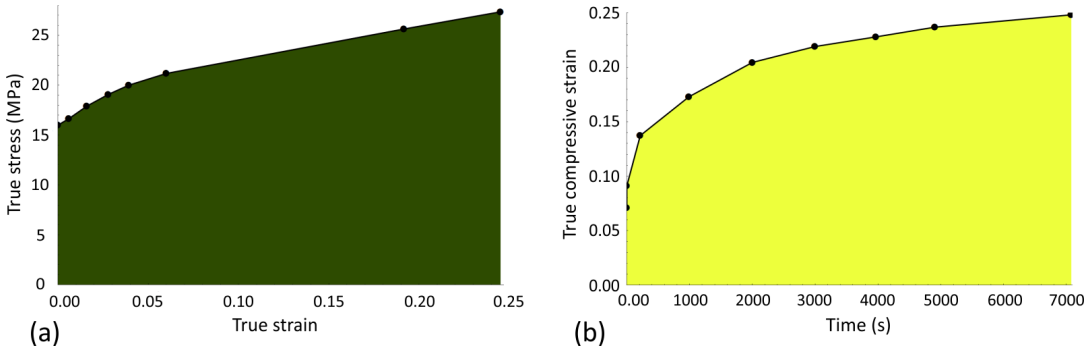

Figure 3.4: (a) Sress-strain curve for UHMWPE adapted from Godest et al. (2002). (b) Mean creep curve for UHMWPE at 37 °C under constant stress of 15 MPa adapted from Reeves et al. (1998).

In the FE simulation, the mechanical response of the femoral component (CoCrMo) was assumed to be linear elastic with a 220 GPa Young's Modulus and Poisson's ratio equal to 0.33. Similar constitutive assumptions were used for both the socket and cantilever arm (steel) and a 200 GPa Young's modulus and a 0.3 Poisson's ratio were used. The forces driving the simulated AMTI system consisted of constant vertical loads (0.25, 0.45, 0.9, 1.8 and 3.6 kN) modulated by a time-dependent amplitude curve (**Figure 3.5**) and applied sequentially.

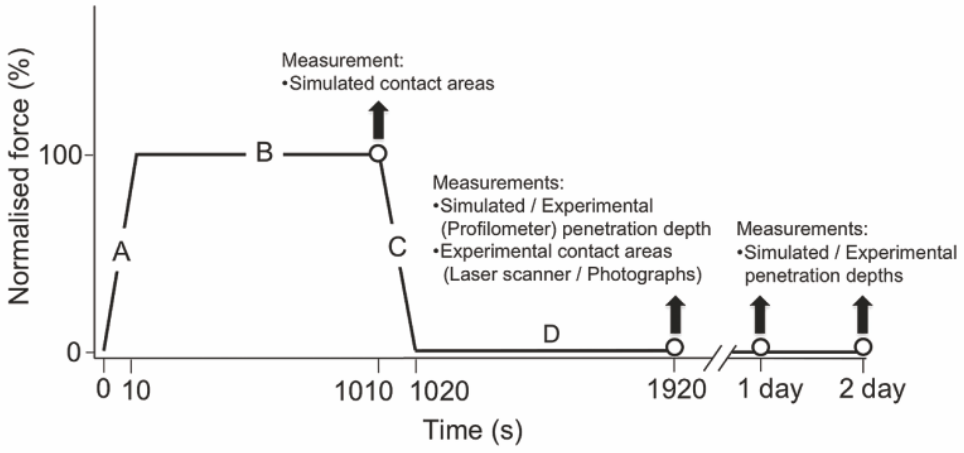

Figure 3.5: Force amplitude profile for each of the 5 loads considered (0.25, 0.45, 0.9, 1.8 and 3.6 kN). The loading cycle is split into 4 stages (A: ramping-up of the load, B: holding of the load, C: ramping-down of the load, D: deformation recovery). The final loading cycle (3.6 kN) features 2 additional stages corresponding to extended recovery periods (1920 s to 24 hours and 24 to 48 hours).

There were no input motions such as I−E rotation, V−V / M−L motions, and A−P tilt. Unlike for the physical experiment, the sinusoidal flexion about the distal sagittal femoral radius was not considered in the FE analyses. It was assumed that the flexion cycle operated at a constant deformation of the UHMWPE surface, and consequently this meant that the CA was not affected by the sinusoidal flexion. The pliancy effect of the cantilevered arm due to imperfect conformity between the femoral flexion arm and the socket was computationally replicated through direct geometrical constraints induced by recreating the identical geometrical tolerances of the mechanical parts as measured in the physical setup. The nodes of the external surface of the socket were fixed in translation while the vertical load was applied at the bottom surface of the tibial insert through a rigid surface (analytical surface in ABAQUS) that was tied to it. This rigid backing prevents the occurrence of unwanted bending moments in the UHMWPE insert, as those occurring in a standard three point bend test (flat UHMWPE/double convex femoral component). Each experimental loading cycle in the FE models was simulated using four distinct analysis steps (**Figure 3.5**)(option *STEP in Abaqus):

- **Step A:** ramp loading over 10 s,
- **Step B:** load holding for 1000 s,
- **Step C:** ramp unloading over 10 s,
- **Step D:** deformation recovery over 900 s.

The total cycle length per loading cases is therefore 1920 seconds. This 4-step cycle was applied sequentially for the five load cases: 0.25, 0.5, 0.9, 1.8 and 3.6 kN. This meant that a full FE analysis consisted of 5×4 steps with the addition of 2 steps simulating deformation recovery between 9600 seconds (the end of the five cycles) and 1 day, and between 1 and 2 days (**Figure 3.5**).

Tie constraints were created between the femoral component and the AMTI cantilever arm to simulate the experimental constraint created through cementation of these parts. A horizontal spring with a stiffness of 10 N (**Figure 3.1**) was connected to the distal end of the beam to the inside of the socket in order to simulate the mechanism locking the arm into the socket and to prevent horizontal sliding of the beam. Gravity loads were not accounted for.

Abaqus/Standard surface-to-surface contact algorithm (ABAQUS, 2012) was used to enforce the contact between the socket and flexion arm, and between the femoral and tibial components. Static coefficients of friction for lubricated and greasy surfaces of 0.08 (steel-on-steel) (Johannes et al., 1973) and 0.04 (CoCrMo-on-UHMWPE) (Godest et al., 2002) were used. The whole mechanical system had a total of 226 949 elements. Both socket and AMTI flexion arm were meshed with fully integrated linear hexahedral (C3D8) elements, with global mesh size of 2 mm. The femoral component geometry was partitioned so that a hybrid tetrahedral-hexahedral mesh could be built (**Figure 3.6**)

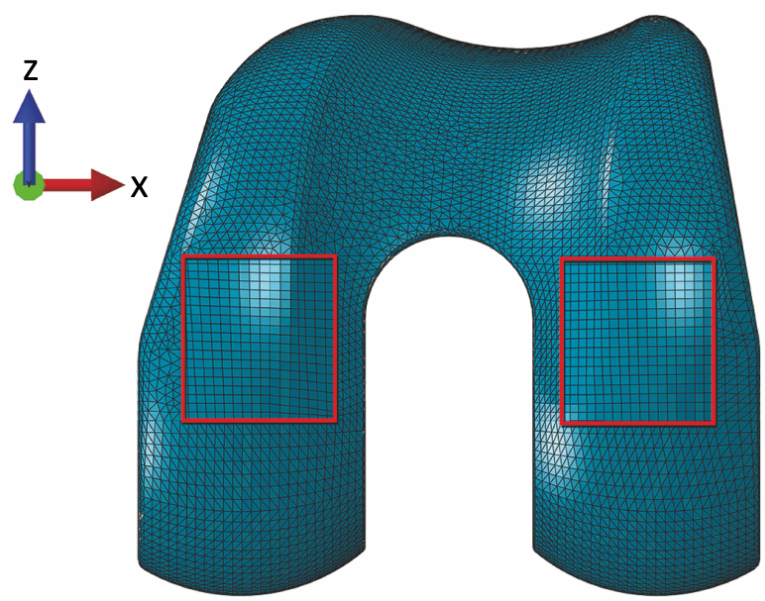

Figure 3.6: Inferior-superior view of the femoral condyle hybrid mesh highlighting the boundary between the sub-regions (tetrahedral and hexahedral elements).

The rationale for this was to use linear hexahedral elements for the surfaces of the femoral condyles contacting the tibial insert, also meshed with fully-integrated 8-noded hexahedrons (C3D8). Because of the complexity of the femoral condyle geometry it was not possible to mesh it automatically using exclusively hexahedral elements. The remaining part of the femoral condyle was meshed using linear tetrahedral (C3D4) elements. A mesh sensitivity study to assess the accuracy of results was performed on the femoral and tibial components using three different global mesh sizes: 0.6, 1, and 1.5 mm. The best compromise between accuracy and analysis time was found to be for a global mesh size of 1 mm. The femoral and tibial components used the same global mesh size in all simulations. CAs and PDs were measured at the lateral condyle because it had the larger loads and PDs in both experiments and FE simulations.

3.2.2 Results

3.2.2.1 Penetration Depth

The PD for each of the 5 vertical loads (peak values at the end of the loading cycle) and after 1 and 2 days of deformation recovery are depicted in **Figure 3.7** for the laser scanning and profilometry measurements as well as the 3 series of FE analyses (E-FE, EP-FE and EV-FE models which will also subsequently be referred to as respectively the "elastic model", "elastoplastic model" and "viscoelastic model").

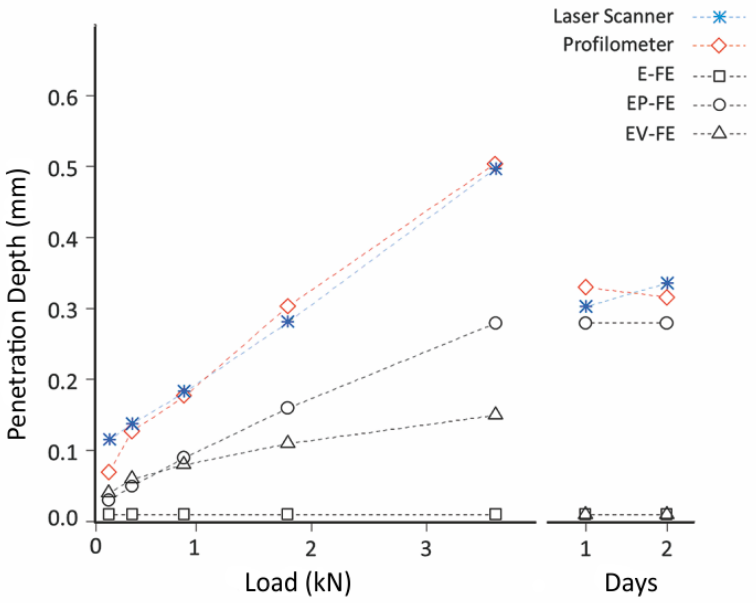

Figure 3.7: Maximum penetration depths within the UHMWPE tibial insert for both simulations and experiments and for the 5 different loading scenarios (0.25 to 3.6 kN). Penetration depths at 1 and 2 days following the last loading cycle (3.6 kN) are also plotted.

The variation of PD with increasing load follows an almost linear trend for both experimental measurements which are very similar (**Figure 3.7**). At 1 day deformation recovery, the PDs are 0.293 and 0.320 respectively for the laser scanning and profilometry measurements. At 2 days recovery, these values are 0.326 and 0.306.

As expected, and by construction, the E-FE model fully recovers the deformation in each loading cycle after 900 s as well as after 1 and 2 days of recovery. The FE models under-predict PDs compared to those measured experimentally. The variation of PD for the viscoelastic model exhibits a characteristic creep-like curve (plateauing exponential) with increasing load whilst that curve is also non-linear for the elastoplastic model (**Figure 3.7**). At loads higher than 0.5 kN the PD for the EV-FE model increases more slowly than that of the EP-FE model. After 1 and 2 days of recovery, the deformation predicted by the EP-FE is the closest to that of the experimental data. The E-FE and EV-FE models, on the other hand, fully recover their deformation (**Figure 3.7**).

The overall relative difference between the EV-FE model and the laser scanner data range between 72 % and 59 %, while between the EV-FE model and the profilometer data range between 50 % and 72 %. For the EP-FE model, these differences lie respectively in the ranges 8−81 % and 12−66 %. At 1 and 2 days deformation recovery, the residual deformation in the EP-FE model is 0.27 mm which is very close to the 0.326 and 0.306 mm values obtained experimentally (**Table 3.1**).

Table 3.1: Relative difference (%) in the penetration depth between FE simulations (E-FE, EP-FE, and EV-FE) and experiments (laser scanner-LS, profilometer-Pr)

Load (kN)	EV-FE vs. LS	EP-FE vs. LS	EV-FE vs. Pr	EP-FE vs. Pr
0.25	−72	−81	−50	−66
0.45	−61	−69	−57	−66
0.9	−59	−53	−58	−52
1.8	−63	−45	−66	−49
3.6	−71	−45	−72	−45
1st day recovery	n\a	−8	n\a	−16
2nd day recovery	n\a	−17	n\a	−12

3.2.2.2 Contact Area

CA measurements are compared for the FE models, laser scanning and photographic measurements on **Figure 3.8**.

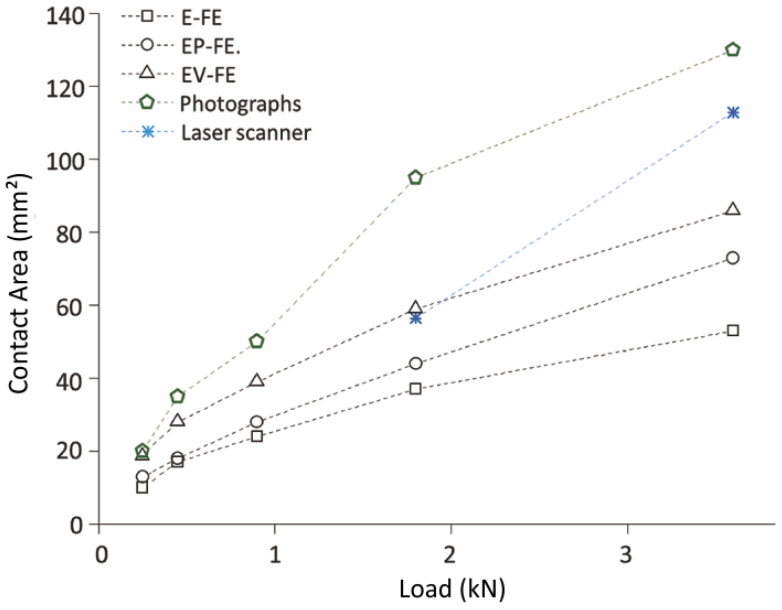

Figure 3.8: Maximum contact areas on the UHMWPE tibial insert (reported for the lateral condyle) for both simulations (E-FE, EP-FE, and EV-FE) and experiments (photographs of contact scars and profilometry measurements).

Laser scanning acquisitions of the CA were only performed for the 1.8 and 3.6 kN loads. The photogrammetric (ink-staining) method only provides an indication of the peak experimental CA, whereas the laser-scanning method provides additional measurements of the subsequent recovery phase. CAs are generally higher for the viscoelastic model than for the plastic and the elastic models. As expected, the CA increases with the load. The CAs for the inelastic (EV-FE and EP-FE) and elastic models monotically deviate from each other as the load increases which highlights the progressive dominant role of inelastic deformation mechanisms. The numerical models consistently under-predict the CAs measured experimentally except for the viscoelastic model which matches the CA obtained via photographic measurements at 0.25 kN and mostly that obtained by laser scanning at 1.8 kN. In both experimental acquisitions and simulations, CAs are found to be different between the medial and lateral condyles. This imbalanced load distribution between them is caused by non-negligible geometrical tolerances magnified by the pliancy effect of the arm (**Figure 3.2** and **Figure 3.11**). Simulated *total* CAs with the relative distribution of the load between the lateral and medial condyles for every load cycle are listed in **Table 3.2**.

Table 3.2: Simulated total contact areas (CA) for the 3 FE models and for each loading cycle and relative distribution (RD) of load (%) between the medial (Med.) and lateral (Lat.) condyles of the tibial insert.

	Simulated total CA			**RD of load (%) between tibial condyles**					
Load (kN)	E-FE	EP-FE	EV-FE	Lat. cond. E-FE	Med. cond. E-FE	Lat. cond. EP-FE	Med. cond. EP-FE	Lat. cond. EV-FE	Med. cond. EV-FE
0.25	10	13	21	100	0	100	0	90	10
0.45	17	19	37	100	0	95	5	76	24
0.9	29	35	58	83	17	80	20	67	33
1.8	49	62	90	76	24	71	29	66	34
3.6	76	108	138	70	30	68	32	62	38

Unlike the elastic and plastic models, in the EV-FE model contact was always distributed on both the medial and lateral condyles. The overall CA difference between the EV-FE model and photographs ranges between 5 and 38 %, while the difference between the EP-FE model and photographs varies between 35 and 54 % **Table 3.3**.

Table 3.3: Relative difference (%) in CA between FE simulations (E-FE, EP-FE, and EV-FE) and experiments (photographs-Ph, and laser scanner-LS) for each loading cycle.

Relative difference in contact area (%)				
Load (kN)	EV-FE vs. Ph	EP-FE vs. Ph	EV-FE vs. LS	EP-FE vs. LS
0.25	−5	−35	n\a	n\a
0.45	−20	−49	n\a	n\a
0.9	−22	−44	n\a	n\a
1.8	−38	−54	+5	−22
3.6	−34	−44	−24	−35

3.2.2.3 Contact Pressure

In the experiments, CPs were not measured but they are standard output of any contact FE analysis. As highlighted in the introductory paragraph, CPs are critical in computational wear algorithms based on Archard's law. They are therefore reported for the three FE models and for each load interval on **Figure 3.9**.

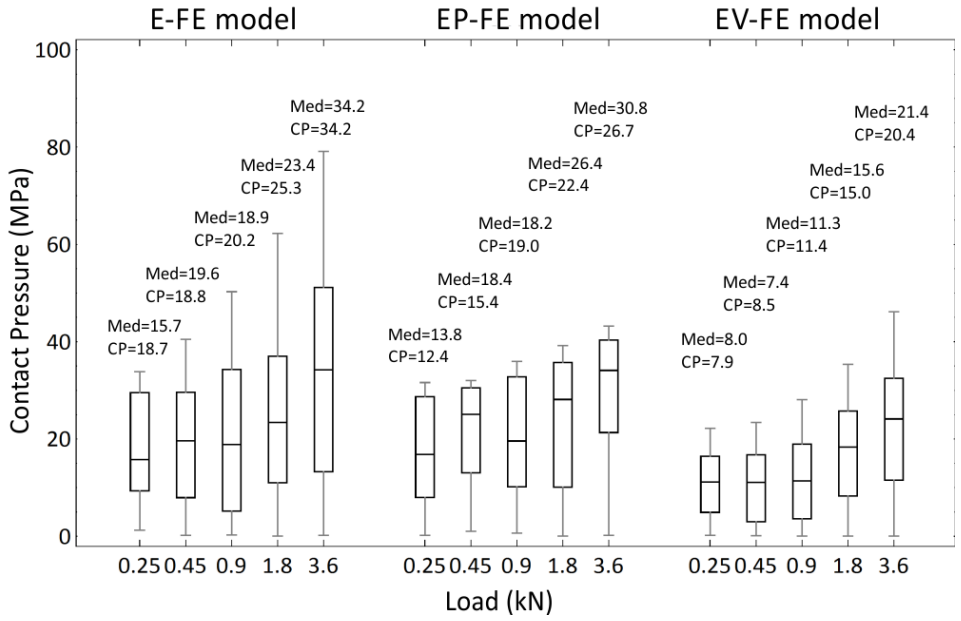

Figure 3.9: Box plots of the calculated contact pressure as a function of the compressive load applied (0.25 to 3.6 kN) for the 3 finite element models considered: elastic UHMWPE (E-FE), elastoplastic UHMWPE (P-FE) and viscoelastic UHMWPE (V-FE). Minimum, maximum, first, second (Med) and third quartile of the contact pressure are reported together with the mean contact pressure (CP).

CP values were output for all the surface nodes part of the potential contact zone on the tibial insert (pre-defined before each FE analysis and identical for the 3 FE models). This means that, nodes not in contact with the femoral condyles have a null CP.

In stark contrast with other published studies, and instead of reporting only peak CPs which can be misleading due to numerical artefacts, minimum, maximum, first, second (median) and third quartiles as well as the mean values are reported. The median value has the advantage of not being influenced by the extreme ones. The mean CP (averaged over the nodes in contact) increases with the load magnitude in all FE simulations.

However, the mean CP is only an approximation of the actual CP profile at the articulating surface of UHMWPE. In particular, assuming a frictionless Hertz contact between a sphere and an elastic half-space, there is a CP gradient with a maximum at the centreline of the contact and minima at the edges of the contact (see **Figure 3.10**-a). On the other hand, the mean assumes a homogeneous/equal distribution of CP over the contact. In a real situation, it is expected a contact condition similar to that predicted by Hertz's theory, with some regions of the material experiencing peak pressures values. Clearly, values of mean CP are smaller than those measured for the peak CP since they are averaged over the contact.

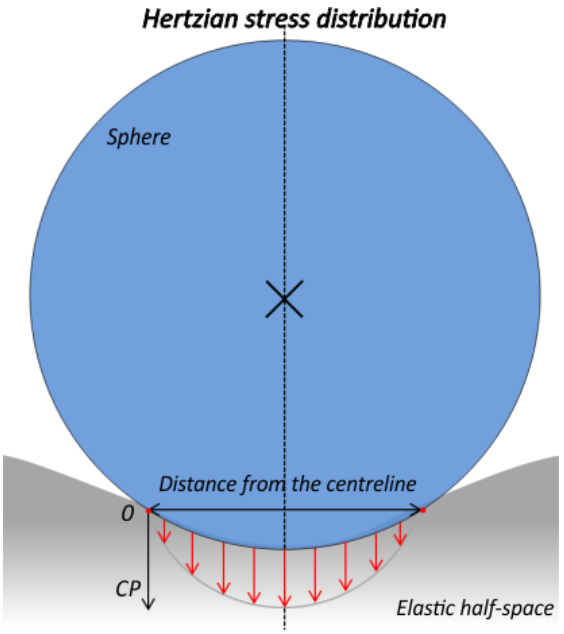

Figure 3.10: Expected stress distribution between a sphere and an elastic half-space using Hertz's theory of elasticity (Johnson and Johnson, 1987; Young and Budynas, 2002) (a) and mean (b).

The mean and median CPs are very close to each other indicating a relatively homogeneous spread of values which was also corroborated by homogeneous distributions of CP on colour plots (not presented here). Mean CPs (**Figure 3.9**) for the E-FE model ranges from 18.73 MPa (0.25 kN load) to 34.19 MPa (3.6 kN load). For the EP-FE and EV-FE models, the ranges are respectively 12.46−26.68 MPa and 7.92−20.43 MPa. Overall, for the elastic model CP values are more spread around the median than those of the viscoelastic and plastic models suggesting larger gradients of deformation (**Figure 3.9**).

3.2.3 Discussion

3.2.3.1 Penetration depth

Results of the FE analyses indicate that permanent plastic deformations (EP-FE model) and residual creep deformations (EV-FE model) are observed at all load levels. This qualitatively corroborates the laser scanner and profilometry measurements which also highlight the existence of inelastic residual deformations. At low loads (0.25 and 0.45 kN) residual deformations for the viscoelastic model are higher than those for the elastoplastic model. However, it should be noted that the constitutive parameters for the creep formulation were based on a creep experiment at a 15 MPa compressive stress level. This means that the creep response of the EV-FE model is probably over-estimated for loads that induce a CP lower than 15 MPa (Reeves et al., 1998). Conversely, at stress levels higher than 15 MPa that would mean under-estimation. From 0.9 to 3.6 kN loads the residual deformations of the elastoplastic model are higher than those experienced by the viscoelastic model. The residual deformations of the EP-FE model are the closest to those measured experimentally and follow a similar mostly linear evolution. After 1 and 2 days recovery the plastic deformations are very close to the experimental ones (**Figure 3.7**) indicating that, by deduction, the viscous effects in the UHMWPE insert under compression have a negligible influence after 1 and 2 days. This is also confirmed by the full deformation recovery (zero residual PD) obtained for the EV-FE model after 1 day. From these results, it is evident that viscous and plastic effects are key in the mechanical response of a UHWMPE tibial insert mounted on a AMTI knee simulator and subjected to the loads described in section 3.2.1. Besides, by summing up the penetration depths measured for both viscoelastic and elastoplastic models at high loads (i.e. load-case 3.6 kN in **Figure 3.7**), a closer fit to the experimental results is obtained. This suggests the need for a combined viscoplastic model (see chapter 5) to account for the viscous and plastic contributions observed in the experiments.

Significant viscous effects are still present after 900 seconds recovery and this has an important significance for *in vivo* clinical conditions where joints are subjected to high frequency loads with a time period two order of magnitude smaller than 900 seconds. Depending on the magnitude of compressive loads, up to 0.14 mm penetration (at 3.6 kN) can be observed at the surface of the UHMWPE insert after 900 seconds recovery. That means that this figure can be significantly higher in the immediate time vicinity of when the maximum load is applied. These surface deformations have the potential to be detrimental to the kinematics of the TKR but this remains to be proved. Any deviation from the optimal kinematics may lead to high stress (particularly for cross-shear motions) which could exceed the plastic yield point of UHMWPE. The potential consequence of that is an acceleration of the wear process particularly if UMWPE debris are released in the joint.

In a FE study looking at the influence of creep deformation on the contact mechanics of TKR, Rullkoetter and Gabriel (Rullkoeter and Gabriel, 2000) calculated a PD of 0.44 mm before unloading with an applied compressive load of 3 kN.

They used a quasi-static FE simulation to replicate a tibio-femoral contact above 30 ° knee flexion. The UHMWPE tibial insert was modelled as a linear viscoelastic solid similar to the current study but with different constitutive parameters. In the EV-FE model, at the end of the load holding phase, a 0.7 mm PD was observed. This value has a comparable magnitude to that found by Rullkoeter and Gabriel (2000) in their computational analysis.

3.2.3.2 Contact area

It is known that the contact patches on the tibial insert changes according to the degree of knee flexion (Carr and Goswami, 2009). It is therefore worth to point out that the present study considered the TKR system for a zero degree flexion configuration (which corresponds to a standing position).

The EV-FE simulations showed the highest CA among all FE simulations (**Figure 3.8**), and, as a logical consequence, the lowest CP (**Figure 3.9**).

Using a finite element model Rullkoeter and Gabriel (2000) simulated a compressive creep experiment on a TKR with a 3 kN load. They measured a total CA of 140 mm^2, which was very close to 138 mm^2 at 3.6 kN found in our EV-FE model (summing together the medial and lateral condyles). Combining physical experiments and finite element analyses, Liau et al. (2002) studied the effects on the contact mechanics of inserting a Fuji-film into an artificial tibio-femoral articulation (TKR). In their simulation the contact was set at $0\,^\circ$ flexion and the UHMWPE tibial insert was modelled as linear elastic. They found a CA of 200 mm^2 at 3 kN, while a CA of 76 mm^2 for the 3.6 kN load case was measured in our elastic E-FE model, which was about 2.5 times smaller. This significant difference in CA could be attributed to a number of factors including implant size, mechanical properties, implant conformity; we used a flat tibial insert (low conformity) while Liau et al. (2002) used an implant with higher conformity. The finite elements composing the mesh of the UHMWPE insert in the study carried out by Liau et al. (2002) appears to have a sub-optimal aspect ratio which could have led to erroneous (not converged) solutions. Since the version 5.8 of Abaqus/Standard used by Liau et al. (2002), significant advances have been made in the accuracy of contact algorithms. Frictionless contact was also used in their FE model but this effect is believed to be negligible in explaining the difference in CA.

In the present study, the observed difference in CA distribution between condyles (**Table 3.2**, **Figure 3.11**) is likely due to the pliancy effect on the femoral arm of the AMTI simulator. The effect was observed in both the physical and computational experiments. The FE results demonstrating this physical observation were obtained by replicating as accurately as possible the exact dimensions and geometrical tolerances of the AMTI setup and not by tweaking (for best fit) FE parameters controlling the stiffness of the whole assembly such as mechanical properties of the individual components or by creating artificial constraints. This certainly provides confidence in the general methodology followed in this study.

As a general rule, it can prove challenging to compare apparently similar computational studies as they generally differ in terms of geometries, boundary and loading conditions, material properties, numerical solving schemes (implicit versus explicit), choice of element formulations, density of the mesh or contact algorithms. However, our CA results are of the same order of magnitude of what has been found by Rullkoeter and Gabriel (2000) and Liau et al. (2002).

Figure 3.11: Photograph of contact scars (white regions) on the UHMWPE tibial insert after application of the 1.8 kN load cycle. The scars are produced by friction-induced removal of the blue tooling ink. Colour contours (Red: viscoelastic model & Black: elastoplastic model) indicate contact area boundaries predicted by the finite element analyses while the filled blue patches represents the surface plot of the contact area obtained by laser scanning, which have not to be confounded with the blue tooling ink. The colour intensity of the area corresponds to the maximum penetration depth measured using laser scanner (mm).

3.2.3.3 Contact pressure

In the experiment conducted by Metcalfe (2011), no pressure measurement system (e.g. TekScan) was used so simulated CP obtained in the current work in both condyles could only be compared to data available in the literature. The fact that the inter-quartile range −which represent half of the data spread around the median− of the CP is much smaller for the viscoelastic model (**Figure 3.9**-C) indicates that the CP values are more homogeneous than those computed for the elastic and plastic model. Given that the mean and median CP values of the viscoelastic model are the smallest of the 3 FE models one can infer that viscoelastic deformations offer a stress reduction mechanism which could be beneficial on one hand. On another hand, this is accompanied −or rather induced− by larger UHMWPE deformations which could be detrimental to the kinematics of the joint when it is no longer loaded in simple axial compression.

Halloran et al. (2005) simulated a TKR using an elastoplastic constitutive law to model the mechanical response of the tibial insert. They measured a CP of 5 MPa at 0 % gait cycle for an applied load of 0.25 kN, and a value of 10 MPa at 25 % gait cycle for an applied load of 0.4 kN. The EP-FE model predicted a mean CP of 12.46 MPa at 0.25 kN and 15.45 MPa at 0.45 kN, which is comparable to Halloran et al. (2005).

In their study simulating the compressive creep behaviour of a tibial insert, Rullkoeter and Gabriel (2000) found a maximum CP of 28 MPa for an applied load of 3 kN, which is comparable to the mean CP of 20.43 MPa found in the EV-FE model.

Liau et al. (2002) found a CP of 28 MPa for an applied load of 3 kN, which value was comparable to 34 MPa at 3.6 kN found in our F-FE model. The differences in CP between Liau et al. (2002) study and this one are not so dramatic as those found for CA. This would suggest that the main source of discrepancy for CA is probably related to differences in size of the implant components considered.

In the physical experiment (Metcalfe, 2011), the tibial surface articulating against the femoral component have probably experienced shear forces in the A−P direction due to the femoral F−E rotation rather than pure I−S compression. These F−E rotations would be likely to be induced by kinematic geometric constraints arising from bringing in contact two surfaces featuring different curvatures (possibly misaligned). In an *in-vivo* setting, the shear forces generated at the tibial insert surface through the rotation of the femoral component could lead to cyclic fatigue damage, and consequently to a more severe degree of deformation of the tibial insert than that predicted by the FE simulations, particularly if considering inelastic effects such as creep or plastic flow. Explicit and implicit FE methods have been widely used in the last two decades to simulate TKR kinematics and kinetics with special emphasis on predicting contact mechanics. UHMWPE contact stresses and deformations are key quantities to evaluate the potential for wear and/or damage occurring in TKRs. Indeed, they are the main input variables that drive algorithmic phenomenological wear models based on the Archard's law of abrasive wear (Archard, 1953). Although these types of model have been very successful at replicating or even predicting wear of orthopedic implants (Knight et al., 2007; Pal et al., 2008; Willing and Kim, 2009; Zhao et al., 2008; Strickland et al., 2011; Zhao et al., 2006), they suffer from their very empirically-based nature with the result that the underlying physics of wear is not captured.

Consequently, these phenomenological models of wear are restricted to specific type of loading conditions and tend to generalise poorly. It is the authors' opinion that the future of wear prediction of orthopedic implants lies in the development of more mechanistic approaches that will capture the underlying physics of the material (e.g. temporary and permanent viscous realignment of UHMWPE polymer chains with slip of crystalline planes) where wear becomes part of the constitutive formulation of the material instead of being a system property that depends, for example, on the direction and magnitude of sliding and on an associated empirical factor.

3.2.3.4 Conclusions

This hybrid experimental-computational study has demonstrated that, under physiological compressive loads, creep and plastic deformations must be both accounted for into a numerical model (i.e. viscoplastic model) to predict more faithfully the inelastic deformations and CPs experienced by the UHMWPE tibial component of a TKR. Failure to predict accurately CAs and CPs limit the validity of most current computational wear models which centrally rely on these quantities and the sliding distance to compute wear volume (see section 1.1). A way to improve the predicted mechanical response of UHMWPE is to consider the coupled time-dependent anisotropic inelastic mechanical response from small to finite deformations.

Chapter 4

FE modelling of the mechanical behaviour of UHMWPE - Part 2

4.1 Towards an accurate understanding of UHMWPE visco-dynamic behaviour for numerical modelling of implants

In the present study, a series of physical uniaxial compressive tests on commercially available UHMWPE unicondylar inserts (Diezi et al., 2010) were conducted and their computational realisation was implemented using two different approaches: finite element (FE) and multi body dynamics (MBD) modelling. The tests were designed to characterise the respective influence of viscoelastic and plastic deformations of a UHMWPE unicondylar insert on the CA characteristics and associated kinematic and kinetic quantities (deformation and CP) during both loading and unloading. It is noteworthy that the mechanical properties of UHMWPE assigned to the numerical models were extracted from the literature and not subsequently "tuned" so that the computational models fit the experimental tests conducted on the unicondylar component to measure CP, CA and penetration deformations. By comparing the two computational modelling methods to the experimentally-collected data for creep deformation and recovery, it was possible to benchmark current modelling capabilities and quantify how accurately these *in silico* approaches are able to characterise the true visco-dynamic behaviour of the UHMWPE unicondylar tibial insert under test without optimising the constitutive parameters of UHMWPE used in the simulations.

It is noteworthy that the author of this PhD work contributed to the current study through the conceptual design of experiments and the FE modelling, while experimental tests and MBD simulations have been performed by external collaborators.

4.1.1 Material and Methods

A servohydraulic test frame with customised fixtures was used to accommodate a unicondylar knee replacement (UKR) for a load-controlled compressive test (**Figure 4.1**-A).

Then computer-aided design (CAD) files of the implant components were used to generate the experimentally-based MBD and FE models. Alongside these computational models, a Hertzian contact analytical model (Young and Budynas, 2002) was compared with the linear elastic FE model to provide additional validation. For these calculations, the femoral component was assumed to be constant-radius while the tibial insert was idealised as a concave ellipsoid.

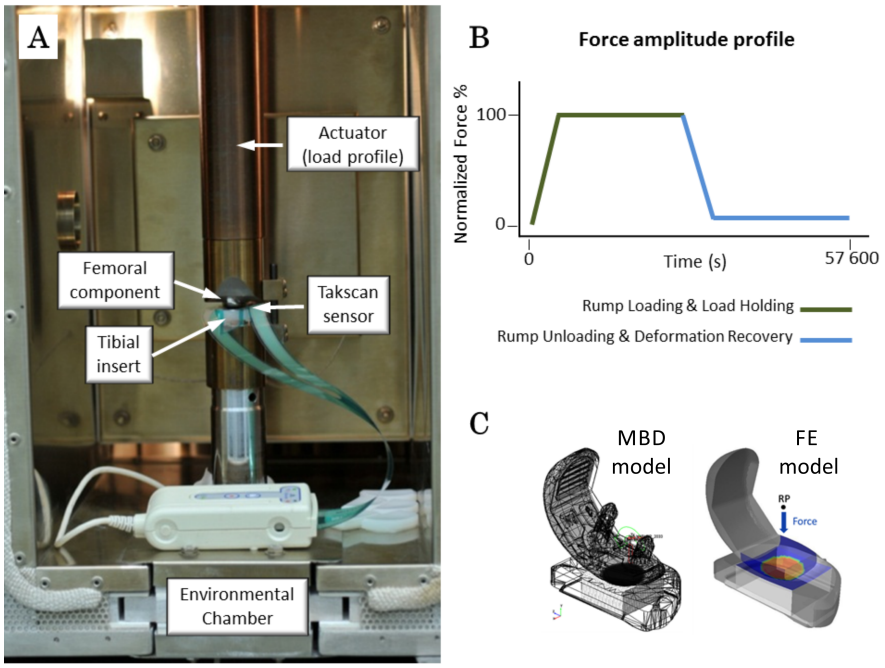

Figure 4.1: (A) Servohydraulic test frame with custom fixturing to accommodate a Unicondylar Knee Replacement (UKR). (B) Force amplitude profile for each of the 4 peak loads considered (450, 900, 1800, and 3600 N). The loading cycle is split into 2 stages: the first is the ramping-up and holding of the load, while the second is the ramping-down of the load and deformation recovery. (C) Perspective view of both MBD and FE models of the UKR (Sigma^{TM} HP UKR system, Size 3, DePuy $^{®}$).

4.1.1.1 Physical testing

Load-controlled compressive creep/recovery tests were performed on a Sigma™ HP UKR system (Size 3, DePuy ® Synthes, Warsaw, IN, USA). The metal femoral component and tibial tray were manufactured from cobalt-chrome and the XLK™ polyethylene insert was made of a remelted compression moulded sheet of GUR 1020 base resin that had nominally been crosslinked using 50 kGy. The metal components were secured to an MTS servohydraulic test frame (model 810) (MTS Systems Corporation, MN, USA) using bone cement and custom fixturing, which aligned the femoral component and tibial tray in zero degrees flexion and zero degrees posterior slope, respectively (**Figure 4.1**-A). The testing was performed dry in an environmental chamber at $37 \pm 1.5\,^{\circ}\mathrm{C}$. Samples were stored in the test chamber at this temperature for at least 24 hours prior to testing.

Four peak load levels (450 N, 900 N, 1800 N, and 3600 N) were selected to span the expected *in-vivo* loading range (D'Lima et al., 2008) as well as subject the UHMWPE structure to elastic and plasticity-inducing loading (Deng et al., 1998; Jauffrès et al., 2008). The experimental force amplitude profile is illustrated in **Figure 4.1**-B. At the beginning of each test a 4 N preload was applied to initiate contact. This load was then quickly ramped at 1000 N/s up to the peak load level and held for 20 000 s. To assess recovery, the loading was reduced at 1000 N/s down to 250 N and held for 37 600 s for all cases. This "recovery load" of 250 N was necessary to maintain sufficient contact at the joint articulation to allow for contact area measurements using TekScan pressure sensors. The total duration of each test was approximately 57 600 s (16 hours). This number was selected so that the downtime for the test equipment was minimised whilst offering a sufficient time span to assess the long-term viscoelastic behaviour of the polyethylene component. A new insert was used for each of the four loading cases.

Throughout each of the four compressive tests, the force, displacement, and CA data were recorded. The force and actuator displacement were measured directly by the MTS force and actuator displacement transducers. Actuator displacement (the superior-inferior translation of the femoral component) provides a surrogate measure of the maximum deformation of the polymer insert (which is measured directly in the numerical models). CA was measured using a TekScan™ (Boston, MA, USA) sensor (model 5033), which was placed between the femoral and tibial components immediately before applying the initial 4 N contact load. Both the MTS and TekScan data were sampled at 1 Hz during the hold phase, while the data rate was faster in both loading and unloading phases.

4.1.1.2 Numerical modelling technique 1: Finite element Analysis

A FE model was developed in ABAQUS/CAE 6.12 (Dassault Systèmes Simulia Corp., Providence, RI, USA), with aSigma™ HP Uni Femoral (Size 3, RM/LL, DePuy Synthes, Warsaw, IN, USA) component on a UHMWPE Sigma™ HP Uni Insert (Size 3, RM/LL size 10 mm). The model was used to replicate the experimental conditions described in the previous section. From this generic FE model, three different model variants, each with a different constitutive model for UHMPWE were generated:

- **FE-E** (Finite Element-Elastic): isotropic linear elastic properties (Young's modulus of 575 MPa and Poisson's ratio of 0.46 (Kurtz et al., 1998).
- **FE-P** (Finite Element-Elastoplastic): isotropic elastoplastic properties with kinematic hardening (Young's modulus of 575 MPa and Poisson's ratio of 0.46 and stress-plastic strain curve from Godest et al. (2002), 16 MPa yield stress), see **Figure 3.4**-a. Plasticity is defined through a von Mises yield surface criteria with associated plastic flow.
- **FE-V** (Finite Element-Viscoelastic): viscoelastic properties featuring compression creep at a 15 MPa stress level for GUR 415 UHMWPE were extracted from the work of Reeves et al. (1998), see **Figure 3.4**-b. The experimental data was fitted to a Prony series-based creep kernel (ABAQUS, 2012).

In the FE simulation, the mechanical response of the femoral component (cobalt-chrome) was assumed to be linear elastic with a Young's Modulus of 200 GPa and 0.3 Poisson's ratio (Bitsakos et al., 2005). Each loading cycle in the FE model was simulated using a single analysis step (option *STEP in ABAQUS) of one phase (**Figure 4.1**-B) and applied through a coupling constraint between a reference point and the surface of the femoral component (**Figure 4.1**-C). As the physical experiment used a "recovery load" it was also included in the FE models. The tibial tray was not included into the FE model, and the nodes of the bottom surface of the tibial insert were rigidly fixed in translation.

An ABAQUS/Standard surface-to-surface contact algorithm (ABAQUS, 2012) was used to enforce the contact between the femoral component and the tibial insert. A 0.04 static coefficient of friction for cobalt-chrome on UHMWPE bearing was used (Godest et al., 2002). The FE model of the whole mechanical system had a total of 72 125 elements. Both femoral and tibial components were partitioned so that a hybrid tetrahedral-hexahedral mesh could be built. The rationale for this was to use linear hexahedral elements for the surfaces of the femoral condyles contacting the tibial insert, also meshed with fully-integrated 8-noded hexahedrons (C3D8). Because of the geometric complexity of the UKR components it was not possible to mesh it automatically using exclusively hexahedral elements. The other parts of the components were meshed using linear tetrahedral (C3D4) elements. A mesh sensitivity study to assess the accuracy of results revealed that a global mesh size of 1 mm provided the best compromise between accuracy and analysis time. Deformation (which is the peak UHMWPE insert deformation in the direction of loading), and CA were measured in both experiments and FE simulations (see chapter 3).

4.1.1.3 Numerical modelling technique 2: Multi-body dynamics simulation

A MBD model of the experimental setup was developed using MSC.ADAMS ® (MSC Software Corp., Santa Ana, CA, USA). Similar to the FE analysis described above, the geometry was imported from CAD data, reproducing the experimental test alignment (**Figure 4.1**-C) and the appropriate boundary conditions of the physical experimental set-up. The insert contact region was discretised into a regular grid of cells, of size 0.5 mm x 0.5 mm (area = 0.25 mm^2) with an elastic contact behaviour defined as previously described (Strickland, 2009). Briefly, an approximate force-overclosure relationship was assigned, of the form:

$$F = E * (1 + 2\nu) * A * \frac{d}{h} \tag{4.1}$$

where F is the contact force, E is the linear elastic modulus (575 MPa), ν is the Poisson's ratio (0.45), A is the individual cell area (0.25 mm^2), h is the material thickness (which varied depending upon location, but averaged approximately 8.5 mm) and d is the interpenetration depth. This interpenetration depth allows the two rigid bodies to partially overlap and intersect (overclosure), to approximate non-rigid contact within a rigid-body environment (this approach is sometimes called the elastic foundation method). This was implemented using the standard MSC.ADAMS ® internal impact function.

In order to simulate creep, a relationship was adopted from the literature (Deng et al., 1998), using a logarithmic response function originating from Deng et al. (1998). This relationship was modified to be used iteratively with an adaptive surface remodelling algorithm:

$$d_{creep} = 1.294 * t * CP * [(log_{10}(t_{end}))^{0.507} - (log_{10}(t_{start}))^{0.507}] \tag{4.2}$$

where d_{creep} is the interval creep depth, CP is the cycle averaged contact pressure, t_{start} and t_{end} are the start-time and end-time of the adaptive time step interval relative to a test start time at t =1 second.

This algorithm was coupled to an adaptive sampling routine with the surface iteratively re-modelled to account for creep. The time-steps were non-linear to reflect creep progression, with smaller steps initially when the rate of creep is high, and larger steps later on when the creep rate has dropped exponentially. Three time-steps were used per log10 decade, at t= 1 s, 2 s, 5 s, 10 s, 20 s, 50 s, , etc − for a total simulated duration of 20 000 s (i.e. equal to the loading time for the experimental test data). Each load case therefore required 14 adaptive iterations, with each iteration requiring 1-2 minutes of simulation time for convergence purposes.

The MBD model was used to simulate the four different loading conditions (450 N, 900 N, 1800 N, 3600 N), and results were plotted at each time interval. The values reported were maximum vertical surface deformation (i.e. peak creep depth), total CA, and both mean and maximum predicted CP. In addition, contour pressure-maps of the contact zone were also produced in each case. Importantly, the model used by Deng et al. (1998) described creep only and was not able to simulate the recovery phase. Therefore, the MBD models were not able to simulate the second half of the experiment (unloading and recovery phase), unlike the FE models, which recreate the full experimental test duration.

4.1.1.4 Hertz theory: Contact of ellipsoidal surfaces

The contact between components of the UKR was assumed to be ellipsoidal under compressive load (Quinci et al., 2014) with the femoral component being concave and the tibial insert convex. Using this particular case of Hertz's theory (Young and Budynas, 2002; Johnson and Johnson, 1987), contact properties such as CA, maximum and mean CP, and deformation in the direction of loading (PD) were computed. The input values used in the following formulas are reported in **Table 4.1**, which relate to the geometry of the UKR used in current study. Subscripts 1 and 2 refer to the UHMWPE tibial insert and the femoral component, respectively.

$$C_E = \frac{1-\nu_1^2}{E_1} + \frac{1-\nu_2^2}{E_2} \tag{4.3}$$

Where C_E, $E_{1/2}$, $\nu_{1/2}$ are respectively the equivalent elastic modulus, Young's modulus, and Poisson's ratio. The major/minor semiaxes (c/g) of elliptical contact area and the parameter accounting for the curvatures of bodies (K_D) are defined as:

$$c = \alpha \sqrt[3]{PK_DC_E} \qquad g = \beta \sqrt[3]{PK_DC_E} \qquad K_D = \frac{1.5}{1/R_1 + 1/R_2 + 1/R_1' + 1/R_2'} \tag{4.4}$$

Where P, $R_{1/2}/R'_{1/2}$ are respectively the total applied load and the minimum/maximum radii of curvature at point of contact, while α, β and λ (see equation 4.6) are tabulated values (table not reported), which selection depends on the following term:

$$cos\theta = \frac{K_D}{1.5}\sqrt{\left(\frac{1}{R_1}-\frac{1}{R_1'}\right)^2 + \left(\frac{1}{R_2}-\frac{1}{R_2'}\right)^2 + 2\left(\frac{1}{R_1}-\frac{1}{R_1'}\right)\left(\frac{1}{R_2}-\frac{1}{R_2'}\right)cos2\vartheta} \tag{4.5}$$

The plane containing the curvature $1/R_1$ makes with the plane containing the curvature $1/R_2$ the angle ϑ. The PD, CA, and maximum/mean CP are defined as follow:

$$PD = \lambda \sqrt[3]{\frac{P^2C_E^2}{K_D}} \qquad CA = \pi cg \qquad CP_{Max} = \frac{1.5P}{CA} \qquad CP_{Mean} = \frac{2}{3}CP_{Max} \tag{4.6}$$

Table 4.1: Input parameters used to describe an ellipsoidal Hertz contact. Values of parameters refer to the UKR used in current study. Subscripts 1 and 2 are associated to the UHMWPE tibial insert and the femoral component, respectively. $E_{1/2}$, $\nu_{1/2}$, $R_{1/2}/R'_{1/2}$, ϑ, α, β, λ are respectively the Young's modulus, Poisson's ratio, minimum/maximum radii of curvature at point of contact, angle between planes of contact bodies, and the remaining are tabular parameters.

Parameters	**Assigned values**
$E_{1/2}$ (Pa)	$5.75 \cdot 10^8/2.00 \cdot 10^{11}$
$\nu_{1/2}$	0.46/0.33
R_1/R'_1 (m)	-0.116/-0.181
R_2/R'_2 (m)	0.036/0.036
α	1.07
β	0.936
λ	0.748
ϑ	18.19

4.1.2 Results

4.1.2.1 Deformation

As expected, an increase in load magnitude is accompanied by an increase in deformation for both the experimental measurements and numerical computations (**Figure 4.2**). Furthermore, the evolution of deformation over time for the experimental and computational (FE-V and MBD) models exhibit a characteristic creep-like curve (plateauing exponential), whilst that curve is clearly not time-dependent for the FE-E and FE-P models. The simulations, however, consistently under-predict deformations compared to the experimental measurements during loading and unloading with the viscoelastic models more closely matching the in vitro experiment than the elastic and elastoplastic models.

At each loading cycle the deformation for the FE-V model increases at a slower rate than that of both the experiment and MBD model. Plastic deformation occurs at loads higher than 900 N (around typical body-weight). This is clearly evidenced on **Figure 4.2**-a-b where the FE-E and FE-P models have an almost identical response.

The elastic model (FE-E) does not recover the deformation after unloading (**Figure 4.2**) due to the presence of the "recovery load" of 250 N (see sub-subsections 4.1.1.1 and 4.1.1.2), which was applied in the physical experiment to maintain contact at the articulation of the UKR.

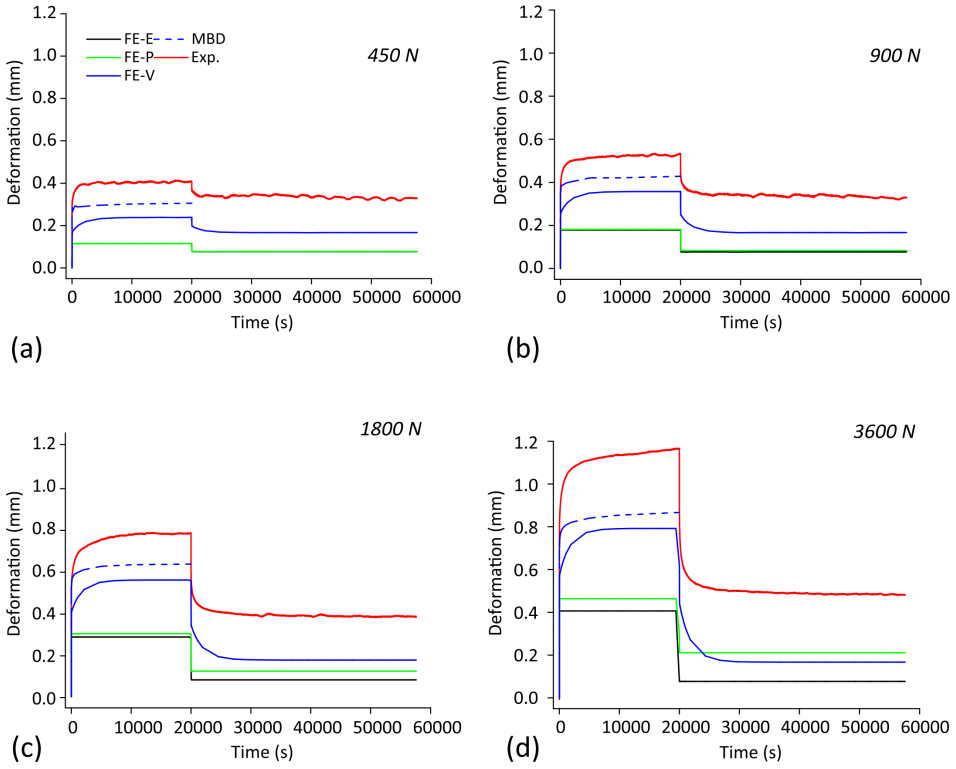

Figure 4.2: Maximum deformation within the tibial insert for both simulation (FE-E, FE-P, FE-V and MBD) and experiments for 4 different loading scenarios (peak loads 450 N to 3600 N). Deformation recovery was not simulated for the MBD model.

Deformation levels are under-predicted for the FE-E model (0.12 mm at 450 N to 0.41 mm at 3600 N) compared to those of the analytical Hertzian model (0.16 mm at 450 N to 0.65 mm at 3600 N) but lie however within the same order of magnitude (**Table 4.2**). It can therefore be concluded that analytical approximations based on Hertzian contact theory could be used for an approximate estimation of the penetration depth.

Table 4.2: Relative difference (%) in deformation between FE simulations (FE-E, FE-V, and FE-P) and experimental measurements under load-holding for the 4 different loading scenarios. The experiment is taken as the reference case. Contact pressures (CPs) within the UHMWPE tibial insert for the FE-E (elastic) and Hertzian analytical models (HM) are reported. The mean CP multiplied by the CA gives the total force applied to the system, which is used as a quality check (Q-C) metric for both numerical model and analytical calculations. All FE measurements were taken at the end of the Ramp Loading & Load Holding phase, see **Figure 4.1**-B.

Load-Holding

	Deformation (mm)				Contact Area (mm^2)			
Load (N)	450	900	1800	3600	450	900	1800	3600
Exp.	0.40	0.52	0.74	1.16	70	104	155	237
FE-E	0.11	0.18	0.27	0.41	31	45	67	99
FE-P	0.11	0.18	0.29	0.46	31	46	74	125
FE-V	0.24	0.36	0.53	0.79	59	89	125	183
MBD	0.30	0.42	0.60	0.86	103	142	192	257
HM	0.16	0.26	0.41	0.65	20	32	51	80
	Relative difference (%)				Relative difference (%)			
FE-E	−73	−65	−64	−65	−56	−57	−57	−58
FE-P	−73	−65	−61	−60	−56	−56	−52	−47
FE-V	−40	−31	−28	−32	−16	−14	−19	−23
MBD	−25	−19	−19	−26	+47	+37	+24	+8
HM	−60	−50	−45	−44	−71	−69	−67	−66
	Max CP (MPa)				Mean CP (MPa)			
Load (N)	450	900	1800	3600	450	900	1800	3600
FE-E	26.8	34.7	45.3	60.3	14.8	20.3	26.9	36.4
Q-C					451	903	1802	3604
HM	33.7	42.4	53.4	67.3	22.4	28.3	35.6	44.9
Q-C					448	900	1798	3601

The deformation recovery is greater for higher loads. This is true for both the physical experiment and the FE-V model, with maximum relative differences of 59 % and 79 % for 3600 N, respectively (**Table 4.3**). The presence of the 250 N "recovery load" explains the non-zero deformation measured during deformation recovery for the FE-E model. Deformation recovery was not accounted for in the MBD simulations.

Table 4.3: Relative difference (%) in contact areas between FE simulations (FE-E, FE-V, and FE-P) and experiments during deformation recovery for the 4 different loading scenarios. The total deformation recovery is defined as the difference between the maximum deformation measured at the end of the holding phase (**Figure 4.1**-B) and the maximum deformation measured at the end of the recovery period (**Figure 4.2**). The deformation recovery factor (%) is the ratio between the total deformation recovery and the maximum deformation measured at the end of the holding phase. MBD computations did not simulate deformation recovery.

Recovery of deformation

	Deformation (mm)				Contact Area (mm^2)			
Load (N)	450	900	1800	3600	450	900	1800	3600
Exp.	0.34	0.34	0.37	0.49	54	53	60	65
FE-E	0.08	0.08	0.08	0.08	21	21	21	21
FE-P	0.08	0.08	0.12	0.21	21	23	27	35
FE-V	0.17	0.17	0.17	0.17	41	41	41	41
	Relative difference (%)				Relative difference (%)			
FE-E	−76	−76	−78	−84	−61	−60	−65	−68
FE-P	−76	−76	−68	−57	−61	−57	−55	−46
FE-V	−50	−50	−54	−65	−24	−23	−32	−37
	Total deformation recovery				Deformation Recovery (%)			
Load (N)	450	900	1800	3600	450	900	1800	3600
Exp.	0.10	0.22	0.39	0.69	24	40	52	59
FE-V	0.07	0.19	0.36	0.62	30	53	68	79

The overall relative difference between the FE-E model and the experimental data ranges between -64 % and -73 % during load-holding (**Table 4.2**) and between -76 % and -84 % during deformation recovery (**Table 4.3**), whilst for the FE-P model these differences lie respectively between -60 and -73 % and between -57 and -76 %. For the FE-V model, these differences range between -28 and -40 % during load-holding (**Table 4.2**) and between -50 and -65 % during deformation-recovery (**Table 4.3**), while the MBD model exhibits relative differences in the range of -19 and -26 % during load-holding (**Table 4.2**). After 10 hours deformation recovery, the residual deformation in both the physical experiment and the FE-P model increases with the load magnitude, respectively from 0.34 mm to 0.49 mm (experiment) and from 0.08 mm to 0.21 mm (FE-P), whilst both the FE-E and FE-V do not show this trend, see **Table 4.2** and **Table 4.3**.

4.1.2.2 Contact Area

CA measurements are compared for the numerical models (FE-V and MBD models will also subsequently be referred to as viscoelastic models) and the physical experiment on **Figure 4.3**. Predicted CA is generally higher for viscoelastic models than for plastic (FE-P) and elastic (FE-E) models.

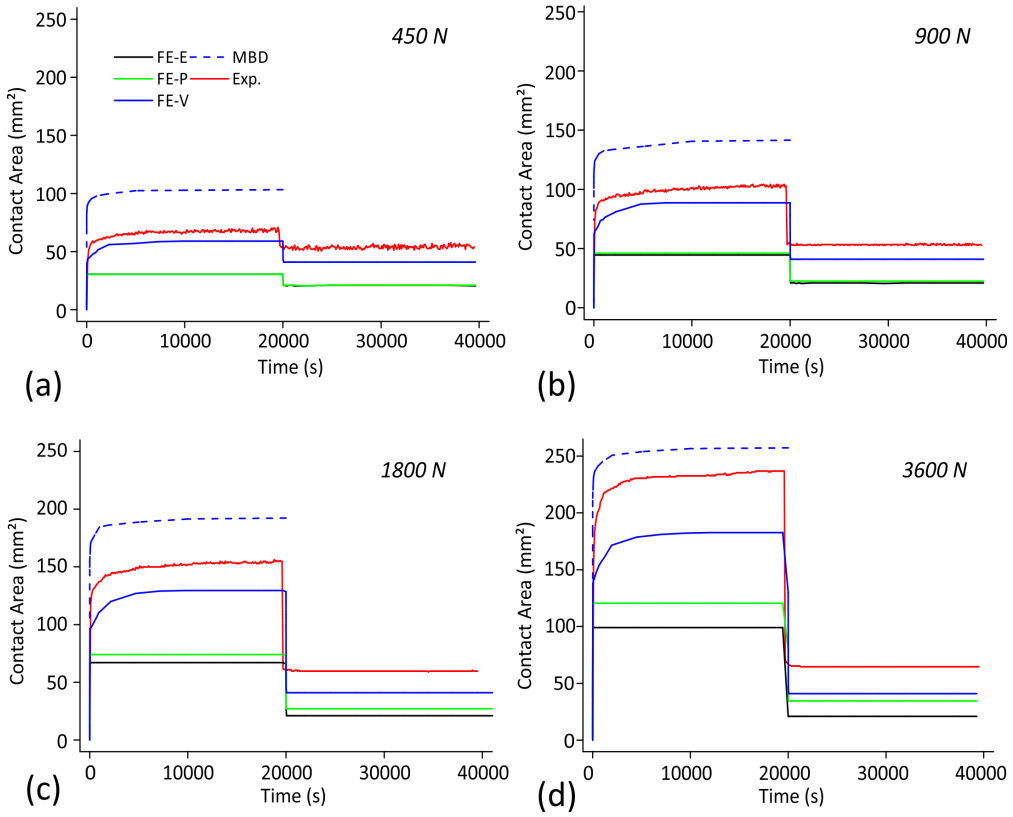

Figure 4.3: Maximum contact areas on the UHMWPE tibial insert for both numerical methods (FE-E, FE-P, FE-V and MBD), and experiments for 4 different loading scenarios (peak loads 450 N to 3600 N). The MBD model did not account for deformation recovery.

The contact areas values (**Figure 4.3** and **Table 4.2**) were higher for the FE-E model (CA = 30.5 to 99.0 mm^2) compared to those of the Hertzian analytical model (CA = 20.0 to 80.2 mm^2). As observed in **Figure 4.3**, the variation of CA for both the viscoelastic models and the physical experiment exhibits a typical exponential creep-type function with a slower rate of creep for the FE-V model. The CAs for the inelastic (FE-V, FE-P, and MBD) and elastic model (FE-E) deviate from each other as the load increases which highlights the progressive dominant role of distinct inelastic deformation mechanisms (i.e. creep and plasticity). The MBD model consistently over-predicts the CAs measured in the physical experiment, whilst a closer estimation of CAs is found for the FE-V model (**Figure 4.3**). The overall CA difference between the FE-E model and the experimental data ranges from -56 % to -58 % during load holding (**Table 4.2**) and from -60 % to -68 % during deformation-recovery (**Figure 4.3**), whilst for the FE-P model these differences lie respectively in the range of -47 to -56 % and -46 to -61 %. For the FE-V model, these differences lie in the range of -14 and -23 % (**Table 4.2**) during load-holding and between -23 and -37 % during deformation-recovery (**Figure 4.3**) , while the MBD shows relative differences in the range of + 8 and +47 % during load-holding.

The FE-E model is clearly most different to the experimental data. The FE-P and MBD models are closer, and the FE-V model comes closest to the experimental results. Similar to the residual deformations, after 10 hours of deformation recovery the residual CA (under nominal loading) in the physical experiment and the FE-P model increases with the load, respectively from 54.06 mm^2 to 64.55 mm^2 and from 21.01 mm^2 to 34.51 mm^2, whilst both the FE-E and FE-V do not show this trend (**Figure 4.3**).

In these latter models the CA during recovery is independent of the load (21 and 41 mm^2 respectively for the FE-E and FE-V models).

The geometries of the simulated (FE-V and MBD) and experimental contact patches were compared using an aspect ratio (AR) metric, which was defined as the ratio of the semi-minor to the semi-major antipodal distances of an ellipse fitting the boundaries of the CA. This metric ranged between 0.73 and 0.84 in both simulations and experiments for all loads (**Figure 4.4**). The AR metric is almost identical for the FE-V and MBD simulations for the four load cases. The angular deviation of the semi-major axis from the semi-major axis of the CA for the experiment at a 450 N load (taken as reference) is also reported for the FE-V and MBD models. The angle of deviation varied between 10 and 41 degrees in both experiments (exception for 450 N) as well as in the simulations for all loads (**Figure 4.4**). For the 3600 N load case there is a very close mutual agreement between both computational and experimental models (**Figure 4.4**).

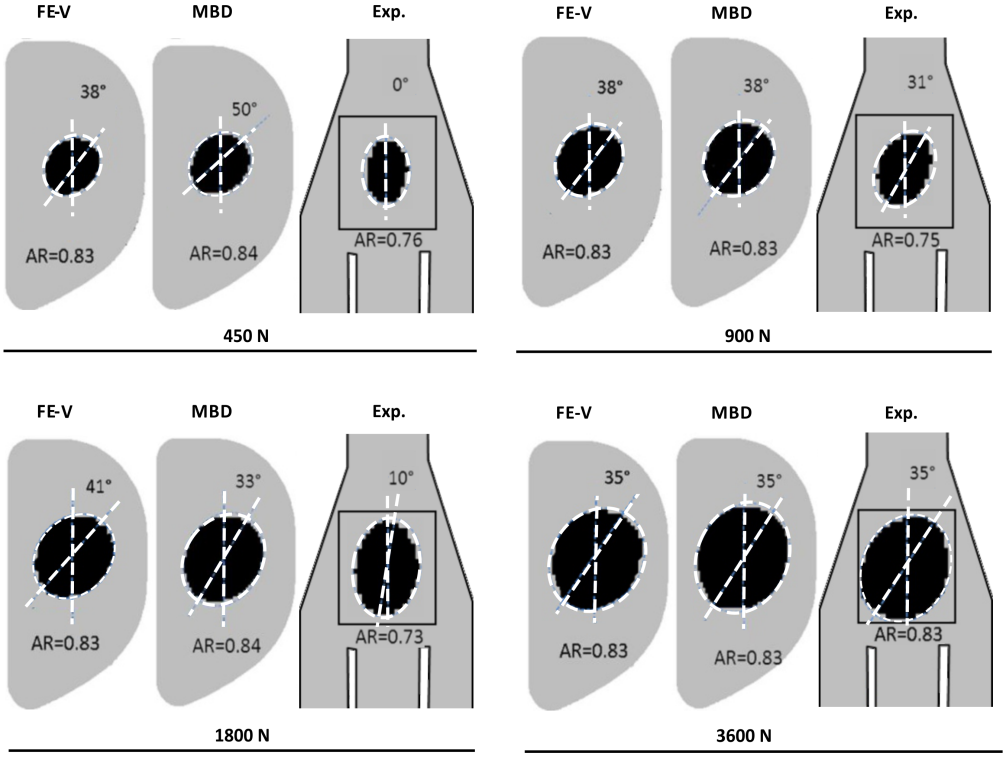

Figure 4.4: Surface plots of the CAs (measured at the end of the holding phase, see **Figure 4.1**-B for the FE-V and MBD models as well as for the physical experiments, for the 4 different loading scenarios (450, 900, 1800 and 3600 N). Simulated and experimental contact areas were compared to each other using the aspect ratio (AR) metric and deviation angle defined in section 4.1.2.2.

4.1.2.3 Contact Pressure

As emphasised in the introduction, CP is critical in computational wear algorithms based on Archard's law. In numerical models, peak CP values can be distorted by numerical singularities and meshing (discretisation) artefacts. Therefore, instead of reporting only peak CP values (**Figure 4.6**), mean CP values (**Figure 4.5**) are also reported. As expected, both the mean and maximum CP increase with the load magnitude in both numerical models. The maximum values of maximum and mean CP are obtained for the elastic FE-E model, followed by the inelastic FE-P, FE-V and MBD models (**Figure 4.5** and **Figure 4.6**). Values of mean and maximum CP for the FE-V model decrease more slowly over time than those measured for the MBD model. It is clear that both viscoelastic models predict lower contact pressure than the elastic and elastoplastic models. In a wear-prediction context this would mean that viscoelastic models would predict a lower wear volume.

The FE-E model under-predicts both mean and maximum CPs (mean CP = 14.8 to 36.4 MPa and maximum CP = 26.8 to 60.3 MPa) compared to those predicted analytically using the Hertzian contact theory (mean CP = 22.4 to 44.9 MPa and maximum CP = 33.7 to 67.3 MPa) (**Table 4.2**). This result was expected due to the higher CAs measured for the FE-E model compared to those calculated for the Hertzian contact theory.

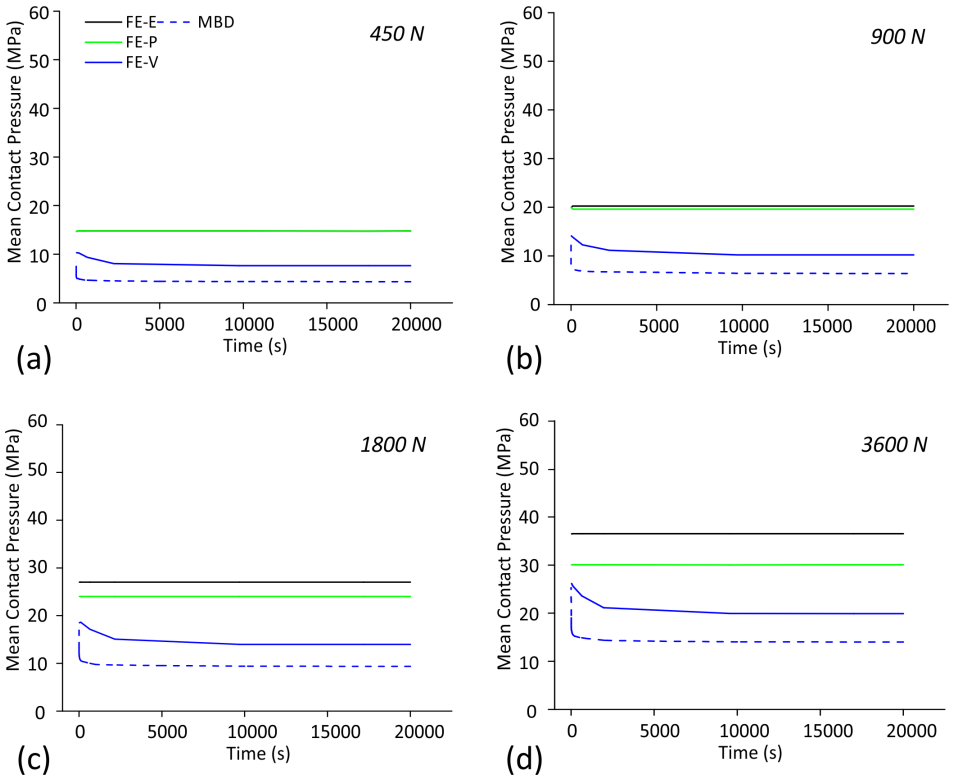

Figure 4.5: MMean contact pressures measured at the joint articulation for both numerical methods (450 N to 3600 N) for loading phase only.

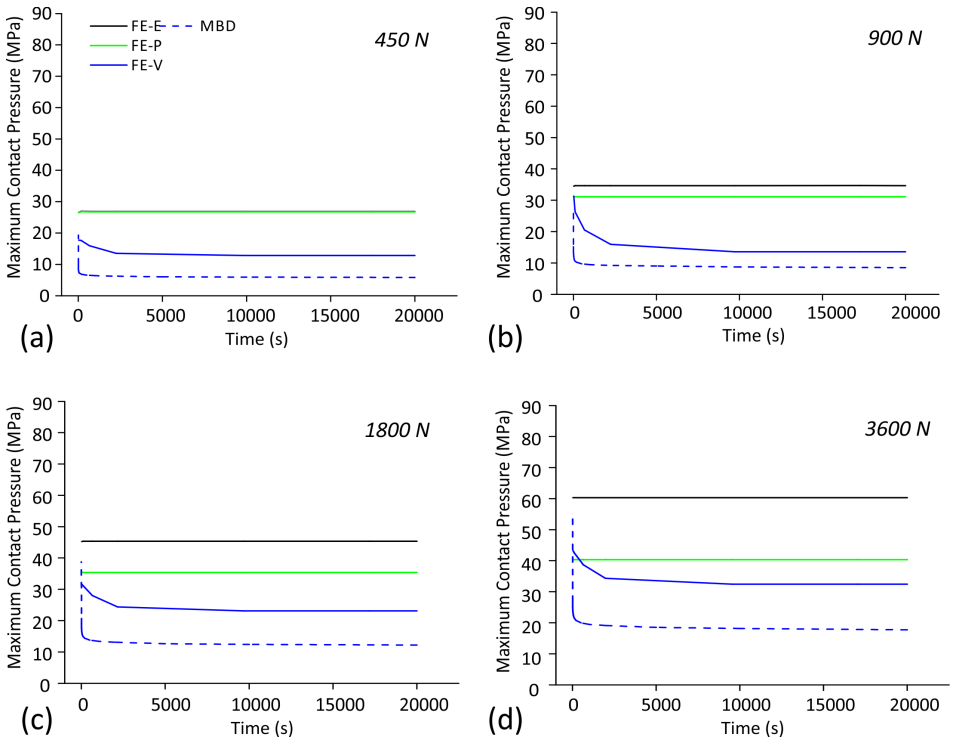

Figure 4.6: Maximum contact pressures measured at the joint articulation for both numerical methods (450 N to 3600 N) for loading phase only.

CP distributions for the FE-V and MBD models for the 4 loading scenarios (450, 900, 1800 and 3600 N) are presented in **Figure 4.7**. The CAs are clearly highlighted and show a close agreement between both numerical models.

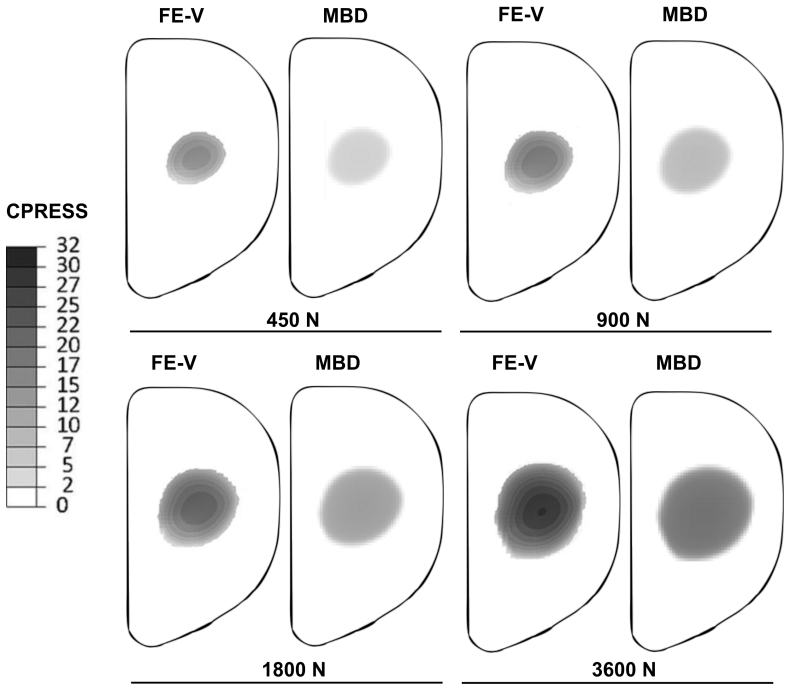

Figure 4.7: Contact pressure surface plots for the FE-V and MBD models for the 4 loading scenarios (450, 900, 1800 and 3600 N).

4.1.3 Discussion

Results of the FE analyses suggest that permanent plastic deformations (FE-P) and creep deformations (MBD and FE-V) are observed at all load levels and must be included in order to achieve qualitative agreement with the experimental measurements. Furthermore, creep may dominate as all residual deformations for the viscoelastic model (FE-V) are higher than those for the elastoplastic model (FE-P). It is worth reiterating that the constitutive parameters for the creep formulation for both MBD and FE-V models were based on published data. No attempt was made to tune any of the numerical models; nevertheless they predicted results showing a very good qualitative agreement with the experiment for maximum deformations and CAs. However, there is a need to conduct a sensitivity study on the constitutive properties used in current simulations to quantify the deviation between predicted and experimental results. A closer agreement between the numerical models and the experiment could be forced by tuning the mechanical properties used for the constitutive models at the expense of a loss of generality for the conclusion of the numerical study.

The FE simulations demonstrated that uncoupled inelastic effects (creep and plasticity) lead to larger deformations at the surface of the UHMWPE component (as compared to the purely elastic response) not only after removal of the compressive creep load (during the recovery phase) but also immediately after application of the load. Viscoelastic creep deformations are dominant compared to plastic deformations. These are important results in connection with computational approaches for wear simulation. Moreover, in reality, creep and plastic deformations may occur simultaneously as part of a complex time-dependent non-linear feedback mechanism which finds its origins in the semi-crystalline and polymeric nature of UHMWPE (Bergström and Bischoff, 2011). Archard's law of wear (see section 1.1) has been widely used in recent years to quantify the production of wear debris in prosthetic implants. It assumes the wear depth to be linearly proportional to a "wear factor", CP, and sliding distance. Then, to calculate the wear volume, the wear depth is integrated across the contact area, accounting for variation in CP and cumulative sliding distance. However, the contribution of each of the previously mentioned parameters on implant wear is still not clear. Using pin-on-disk testing, Mazzucco and Spector (2003) suggested that there was not a clear relationship between wear depth and CP, while Kang et al. (2008) hypothesised an inverse relationship between wear and CP. Conversely, and based on clinical retrieval studies, some authors (Atkinson et al., 1985; Mazzucco and Spector, 2003) suggested that CA may play an important role in arthroplasty wear, observing an increase in percentage of volumetric wear for larger femoral head sizes (i.e. larger CA).

As expected, and by design because of its inability to account for inelastic deformations the FE-E model was clearly unable to predict the experimental data; however it provides a good benchmark for the FE-V and FE-P models. The corroboration with idealised analytical Hertzian contact models generally compared favourably with the elastic FE-E model. Furthermore, the Hertzian theory predicts a linear relationship between the contact area and the indentation depth, a fact that is corroborated by the results obtained from both numerical models and the physical experiments, as shown in **Figure 4.8**.

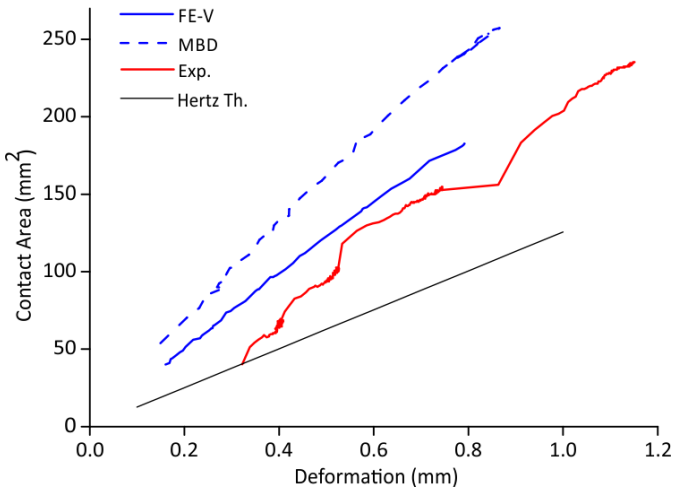

Figure 4.8: Relationship between CAs and deformations for both numerical models (FE-V and MBD), and experiments and for 4 different loads (450 N to 3600 N).

It is noteworthy that any Hertzian solution is only an approximation, for three principal reasons: (1) the model assumes a perfect half-space geometry, whereas in practice the UKR components have finite geometry, and are in fact quite small relative to the contact region; (2) the model assumes a perfectly ellipsoidal geometry; in practice the radii of curvature of the UKR components are variable, and an approximate ellipsoidal fit is used; and (3) the Hertz theory assumes that the contact is entirely elastic (i.e. there is no plastic deformation and time-dependent effects); in reality for the load levels applied in this test, it is observed that there will certainly be some plastic behaviour.

There are few studies in the literature comparable to that presented in this paper. As would be intuitively expected, it has been demonstrated through static simulations of compression tests on total knee / hip implants that as CA (Gomaa, 2011; Rullkoeter and Gabriel, 2000) and displacements (Rullkoeter and Gabriel, 2000) increased, the CP decreased over time (Gomaa, 2011; Rullkoeter and Gabriel, 2000). Moreover, the higher the applied load, the greater the CA (Carr and Goswami, 2009; Krichen et al., 2006; Zdero et al., 2001), and CP (Gomaa, 2011). These obvious and intuitive observations were in accordance with results from both experiments and simulations presented in the present study. The tibial insert in both simulations (specifically MBD and FE-V models) and experiments deformed more than 50 % of the maximum measured displacement within 100 s over a total loading / holding time of approximately 20 000 s for all loads. Within the first 100 s, the CP had reduced between 7.5 % and 40 % in both simulations for all loads. The FE-P model exhibited similar CA, displacements, and CP at 450 N as the FE-E model; but the behaviour of the two models diverged at higher loads. In both models the 450 N applied load generated a 15 MPa mean contact stress at the surface of the insert, a value lower than the 16 MPa yield stress used in the FE-P model (Godest et al., 2002).

At applied loads higher than 450 N the linear elastic constitutive model for the tibial insert tended to overestimate mean and maximum CP and to underestimate CA and vertical deformation of the surface of the insert. These results therefore do not give a true picture of the real contact stresses and deformations occurring in the (now plastically-deforming) UHMWPE tibial insert. Liau et al. (2002) studied the changes in CA and CP occurring at the articulation of a total knee replacement (TKR) due to the presence or absence of a Fuji pressure sensitive film, when a compressive load of 3000 N was applied.

The tibial insert was modelled as an elastic material (with a 910 MPa Young's modulus and a 0.46 Poisson's ratio). The compressive load generated a contact area twice as large as that found in the present elastic FE model for a compressive load of 3600 N which is not surprising considering that the CA of a TKR system is likely to be larger than that of a UKR system. Differences in results can also be explained by different mechanical properties, implant conformity and the use of pressure film devices.

In a FE study looking at the influence of time dependent deformation on the contact mechanics of TKR, Gomaa (2011) calculated CA values of about 160 mm^2, 120 mm^2, and 80 mm^2 with applied compressive loads of 1500 N, 1000 N, and 500 N. The UHMWPE tibial insert was modelled as a elasto-viscoplastic material model using the constitutive law developed by Bergström and Bischoff (2011). In the present study for both viscoelastic and MBD models, at the end of the load holding phase for the 1800 N, 900 N, 450 N applied loads, CA values of 125 mm^2, 89 mm^2, 59 mm^2 (FE-V), and 192 mm^2, 142 mm^2, 103 mm^2 (MBD) were observed. These values have a comparable magnitude to those found by Gomaa in his computational analysis. Moreover the relative difference in maximum CP between current creep models and the computational work of Gomaa ranged between a maximum of 45 % to a minimum of 9 %. This difference in CA and CP could be attributed to a number of factors including implant size, material model and implant conformity; further, in the present study a unicondylar insert was used while Gomaa used a TKR implant.

A good agreement in results for CP values was found between the MBD creep model presented here and the work of Fregly et al. (2003). They performed a compressive test on a TKR implant and used a hybrid computational method combining MBD to predict the position and orientation of the bodies, and elastic foundation theory to predict CP. It was assumed that the material was elastoplastic with a 400 MPa Young's modulus, 0.46 Poisson's ratio and 15.9 MPa yield stress. They simulated mean and peak CP for different flexion angles (from 0 °C to 90 °C) and applied loads (from 750 N to 3000 N). The MBD model showed similar mean and peak contact pressures values for all load cases in the 0 °C flexion case: from 5 to 10 MPa (mean CP) and from 11 to 22 MPa (peak CP).

Villa et al. (2004) presented comparable results to this work, although they used a static FE simulation of a TKR which, by design, could not capture time-dependent effects such as creep. They treated the UHMWPE insert as a nonlinear elastic material (the tangent modulus had a fourth-order dependency on von Mises stress) with a Poisson's ratio of 0.45. These authors simulated a series of vertical loads (2200, 2800 and 3200 N) applied to the femoral component (therefore transmitted through two condyles) at different flexion angles (15, 45 and 60 °C). For the 60 °C flexion angle / 3600 N load case, they calculated a maximum CP of 24.6 MPa while, in the present study, for the 0 °C flexion angle case and an applied load of 1800 N (which would approximately be equivalent to a 3600 N load if considering two unicondylar components), the FE-E model predicted mean and maximum CP values of respectively 26.9 MPa and 45.3 MPa.

There are limitations and issues to be aware of in the present study, in terms of both the experimental and computational aspects. Although a TekScan sensor was used in this experiment to monitor the CA, it was not possible to accurately calibrate the sensor in a manner which would adequately capture the spatio-temporal-varying characteristics of load in the contact region. Therefore, the TekScan data was considered as a reliable indicator of only the total contact area and contact region morphology, but not as a quantitative indicator of contact pressure.

Calibration is an important consideration not only for the TekScan data but also for the force-feedback and displacement-feedback sensors used on the MTS platform; creep-related phenomena are relatively difficult to measure (due to their small relative magnitudes), and because of the time-varying nature of the effect, any drift in the sensor calibration will induce unwanted artefacts into the measurement process.

Although this experiment was designed to characterise creep by using a simplified loading profile, with physiological loading magnitudes, the time-scales of this profile are not physiological; the rate-of-change of loading *in-vivo* is much higher, with loading and unloading occurring within a sub-second time-scale, rather than over thousands of seconds. However, the long time-scale of creep experiments is justified since it approximates the *in vivo* load profile over thousands of sub-second loading and unloading cycles.

This experimentation has clearly shown that although there is a high initial creep-response even within the first few seconds, there is still a significant response over the longer time-scale. The interactions caused by rapid loading and unloading could invoke a different wear-response over the longer-term. This may be an important factor to consider when assessing different groups of TKR patients: for example, those who may take extensive periods of rest and those who don't. To a first approximation, the joints of the lower-limb may be considered as constantly in compression, and such simplifying assumptions were used in early modelling and creep-prediction work. However, in reality there is always an element of unloading in the cyclic loading profiles of human gait, and the precise influence of this transient unloading behaviour on the material is not fully understood.
In the physical experiment, a key challenge is the high initial rate of the dynamic response to both loading and unloading. In this experiment, the data was sampled at a rate of 1 Hz (to limit the total data collected over the $> 60\ 000$ second duration of the test). However, even within the first second, the predicted dynamic response was already close to or over half of the "stead-state" value after several thousand seconds. The immediate, short-timescale transient response of the polymer is therefore not well-characterised in this experiment. Given that this is precisely the time-scale of the response which would occur in a sub-second gait-cycle profile, future studies could investigate these aspects further.

Significant variations of the deviation angle for the CAs measured in the physical experiment (**Figure 4.4**) could indicate misalignment of the tibial and femoral components or mechanical artefacts introduced by the presence of the pressure-sensitive film. Custom fixturing was used to mitigate issues of misalignment of the UKR, but no fixturing was used to locate and align the TekScan sensor due to concerns of creating multiple contacts and buckling.
All of the numerical models (FE and MBD) in the present study used constitutive data from publicly-available academic literature (as opposed to restricted proprietary data). Consequently, there is potential for a mismatch between the UHMWPE employed in experiments and the UHMWPE characteristics modelled in simulations. Despite these "by-design" limitations, the numerical models (FE-V and MBD) were able to capture the experimental contact region morphology with different degrees of accuracy, as indicated by the AR metric and the deviation angle in **Figure 4.4**. These models provide general information on regions of the joint in contact that could be used to inform the test regime for experimentation (i.e. test duration, joint components alignment, etc).

Although different numerical models were used, similar values of mean and maximum CPs were obtained for those simulations that accounted for time-dependent material behaviour (FE-V and MBD); the CPs along with deformations provided an insight into the load magnitudes that induce inelastic deformations on the UHMWPE tibial insert by way of cross-referencing results (**Figure 4.2** and **Figure 4.5**).
A future model intended for accurate predictive work would of course need to be tuned to the specific polymer composition under test. However, it is encouraging to note that the use of "generic" polymer properties based on literature values can give a good approximation to the dynamic creep response, as evidenced by this study. For the FE and MBD models, the simulated maximum vertical deformation, CA and CP at the surface of the tibial insert are all affected by the nature of the discretisation techniques and contact algorithms. As usual with computational models, these limitations need to be kept in mind. In that respect, FE models can be used for what they do best, comparing (implant) designs. In that case, capturing the exact magnitude of response variables such as maximum CP is not as essential as capturing their correct trend. This type of computationally-based approach can be used to screen a large number of implant design variations and select the most promising.

4.1.4 Conclusions

The objective of this study was to characterise the elastic, viscoelastic, and plastic mechanical response of UHMWPE unicondylar tibial inserts subjected to various levels of compressive loads with special emphasis on providing an insight into the long-term creep and recovery response. The working hypothesis was that creep deformations and subsequent recovery can significantly affect the surface geometry of the UHMWPE component (and so the contact pressure) as compared to a purely elastic or elastoplastic response. The study was based on a series of physical experiments and two numerical approaches were used to model the mechanical response of polyethylene, using data available in the literature. It was shown that different modelling methods (FE and MBD) can be used to approximately predict dynamic creep behaviour even using simplified models and generic literature data. However, the accuracy of the results will of course depend upon both the quality of the tuning data, and the fidelity of the constitutive model used to represent the complex behaviour of UHMWPE. From the study, one can conclude that:

- Creep deformations have a significant effect on the contact pressure measured (experiment) and calculated (FE and MBD models) at the surface of the UHMWPE unicondylar insert. In the context of Archard's law-based wear modelling, failure to account for creep deformation effects via appropriate constitutive models would likely result in under/over-prediction of wear volume depending on whether the pressure is predicted in the creep or recovery phase.
- The use of a purely elastoplastic constitutive model for UHMWPE lead to compressive deformations of the insert which are much smaller than those predicted by a creep-capturing viscoelastic model (and those measured experimentally). This shows again the importance of including creep behaviour into a constitutive model in order to predict the right level of surface deformation on a tibial insert.
- At high compressive loads, inelastic deformation mechanisms (creep and plasticity) dominate the mechanical response of UHMWPE components by altering the surface geometry (penetration depth and so contact area) and therefore the contact pressure.

These observations are very relevant for computational wear predictions based on Archard's law which rely on contact pressure to calculate wear volume. This reinforces the message that creep deformations should be accounted for in any Archard law-based computational model of UHMWPE. Future work will attempt to accurately characterise and predict these aspects of creep deformation by using test-data tuned to the specific polymer under test, and integrating both the plastic and viscous-response into a single numerical modelling framework.

Ultimately, the final focus of such models is not the dynamic creep response itself, but the influence this response is having on wear of the polymer. The final purpose of any such creep model is therefore to be integrated into a more complete numerical platform for wear-prediction of future orthopaedic implant devices.

Wear of UHMWPE is the result of a series of simultaneous and cascading multiphysical events which alter the multiphasic structure of the polymer at several spatial and temporal scales. It is believed that the complex time-dependent interactions of the amorphous and crystalline phases of this semi-crystalline polymer are key in understanding creep effects and, how damage and ultimately wear is initiated and propagated in response to macroscopic forces which are not necessarily purely mechanical but also thermal and biochemical. On-going parallel work (Dressler et al., 2011; Gomaa, 2011) is focused on the development of a modular micromechanically-based continuum constitutive model of UHMWPE able to capture its finite strain multiphasic viscoplastic behaviour. The model will be used in conjunction with physical experiments to explore correlations between wear mechanisms and evolution of the microstructure of the polymer.

4.1.5 Conclusive remarks

The computational studies presented in chapter 3 and chapter 4, which focused on characterising the visco-dynamic behaviour of UHMWPE, pave the way for more advanced constitutive approaches. This led us to to select the micromechanically-based constitutive model developed by Bergström and Bischoff (2011), the so-called three network model (TNM). As it will be presented in chapter 5, the constitutive model is used in the context of simulated literature-based experiments to explore possible correlations between multidirectional sliding and microstructure evolution of UHMWPE.

Chapter 5

Micromechanical modelling of UHMWPE chain realignment in multi-directional sliding

Ultra-high molecular weight polyethylene (UHMWPE) is widely used as standard bearing material for total joint replacements due to its excellent properties such as biocompatibility, and resistance to wear/impact. Over the last decade, considerable progress has been made in understanding the conditions that lead to wear of UHMWPE components and a number of strategies have been proposed to enhance UHMWPE wear-resistance properties. Wear performance of UHMWPE components is typically assessed through pin on disk (POD) experiments conducted over a large number of sliding cycles. This type of experiment and its derivatives have been successful in measuring wear rates and unravelling key mechanism and/or factors responsible for wear such as cross-shear motions.

However, POD tests present a crucial limitation that lies in their empirical nature, since they do not provide a direct understanding of the microstructural deformation mechanisms responsible for wear debris formation/release from the contact surface of UHMWPE during articulating motions. In the present study, it is postulated that the evolution of the UHMWPE microstructure during multidirectional sliding can provide information on possible correlations between wear, sliding track shapes, and micromechanics of UHMWPE. The effects of different motion paths on metrics related to the mechanical response of UHMWPE, and particularly to the evolution of molecular chains realignment were investigated through dedicated *in silico* POD tests. In these tests, a UHMWPE pin slid over a stiffer counterbearing made of CoCr. The concept of *anticoaxiality* as a measure of molecular chain realignment (or anisotropy) was introduced to quantify deviation from mechanical isotropy of UHMWPE microstructure. Results from these metrics support the hypothesis that multidirectional sliding as well as long sliding distances produced microstructural changes in UHMWPE, resulting in an enhanced likelihood of material damage, and so wear.

5.1 Introduction

Despite the excellent mechanical performance of UHMWPE as a bearing material of choice for TJR since the 60's (Kurtz, 2009), reports indicate an average total knee replacement (TKR) survivorship of 90 % after 10−15 years from implantation (Woolf and Pfleger, 2003). The main factor limiting the life span of TJRs is the wear of UHMWPE components which results in diminished mechanical performance but, more importantly, leads to the release of sub-micron UHMWPE particles in the periprosthetic tissues. In turn, this triggers an immune response of osteoclast cells, first leading to osteolysis and, ultimately, periprosthetic implant loosening (Barbour et al., 1995).

The wear resistance of UHMWPE has been improved, for instance, by either crosslinking the polymer with γ-ray irradiation (50−150 kGy) followed by heat-treatments (Edidin et al., 1999; Muratoglu et al., 2001; Sobieraj and Rimnac, 2009) and antioxidants such as vitamin-E (McKellop et al., 1999; Renò and Cannas, 2006), or fabricating composites like self-reinforced UHMWPE (UHMWPE fibers within a UHMWPE matrix) (Deng and Shalaby, 1997). Improvement of the UHMWPE chemical formulation is one way to improve its wear resistance.

Another avenue followed by researchers (Saikko et al., 2001) is to focus on TJRs system properties rather than material properties. For example, one strategy consists in reducing the friction between the two counterbearing surfaces of a TKR system by selecting appropriate material combinations. The vast variety of materials and designs has raised the need for simple wear devices to efficiently screen and then identify the best bearing materials to be subsequently tested in full joint simulators (Garvin, 2008; Knight et al., 2007) which present the drawback of being more costly and time consuming. Simple wear testers such as pin on disk systems (POD), offer an efficient way to conduct wear tests over a large number of cycles ($>$ 15 million).

POD devices with a motion track defined by a line such as the reciprocating POD and pin-on-plate (POP) (Barbour et al., 1999), create unidirectional tensile and shear forces at the articulating surface of UHMWPE. The wear rates produced are two to three times lower than *in vivo* measurements (Baykal et al., 2013; Bragdon et al., 1996; Saikko and Ahlroos, 1999). It is believed that these differences are due to the lack of cross-shear solicitations in the *in vitro* case (Wang et al., 2012a). The design of POD testing devices that include multidirectional motions is more challenging since to reproduce the range of trajectories at the articulating surface of TKRs, complex motions/control systems must be devised. The existing link between multidirectional motions and wear rates dates back to the 70's (Charnley, 1976). Moreover, the characteristics of the *in vivo* relative motions of UHMWPE components and their counter face have not been fully quantified yet. A study conducted by Banks and Sawyer (2005) on a TKR implant subjected to a limited number of daily activities, suggested a crossing angle motion ranging between 0 and 10 degrees, while other studies reported even wider ranges (DesJardins et al., 2005; Patten, 2012). In THRs, the motion loci of the femoral head against the acetabular cup might take, throughout a gait cycle, either a quasi-elliptical (Saikko et al., 2004) or a rectangular shape (Turell et al., 2003). However, trajectories of sliding tracks are highly variable from patient to patient due to factors such as posture and body weight (Bennett et al., 2000).

Only in recent years, the gap between wear rates measured *in vitro* and *in vivo* has been reduced (Bragdon et al., 1996; Wang et al., 1997) thanks to the development of a new generation of POD testing devices (Bragdon et al., 2001; Gevaert et al., 2005; Saikko and Ahlroos, 2000). For instance, the circularly translating POD (CTPOD) device (Saikko and Ahlroos, 2000) generates at the articulating surface of UHMWPE both tensile and shear forces in multiple directions (cross-shear) due to the underneath metallic disk that circularly translates at constant velocity. Conversely, the so-called "change-path" (i.e. squared and staircase-like wear tracks) POD device (Gevaert et al., 2005) creates tensile and shear forces only in two perpendicular directions (Dressler et al., 2011; Turell et al., 2003). Both CTPOD and "change-path" POD devices expose the UHMWPE pin to the highest wear, and because the pin is constantly loaded in compression, viscoelastic effects are mitigated. In order to account for creep effects between crossing points in multidirectional motions (i.e. 5 points star wear-track), Gevaert et al. (2005) suggested to use a POP configuration, with the metal pin in contact on the UHMWPE plate. Interestingly, Dressler et al. (2011) demonstrated by using a POD device that the wear rate of moderately crosslinked UHMWPE is not constant when a secondary sliding motion is introduced, which assertion is in stark contrast with the Archard's law of wear (Archard, 1953). This celebrated equation, widely used in tribology, predicts a linear relationship between volumetric wear and sliding distance. In their experiment, Dressler et al. (2011) found that the wear rate was high in the proximity of a change in sliding direction, but after sliding 5 mm the wear rate diminished to values encountered in reciprocating POD testing devices.

In the last decade, alongside with *in vitro* POD tests, a number of analytical wear models have been conceived to account for the effects of cross-shear on wear rates of UHMWPE. A landmark theory for cross-shear-induced wear the so-called "unified theory of wear" was proposed by Wang (2001). In this analytical model, the cross-shear wear is based on the deviations in sliding path from a principal molecular orientation PMO (or alternatively principal sliding direction), and the amount of volumetric wear is proportional to the frictional work generated in the direction perpendicular to the PMO (orientation softening). Generally, the trajectories of the motion loci are identified by means of an aspect ratio (AR), and the worst case of wear damage occurring in UHMWPE is predicted by Wang's theory for an AR of 1 that correspond to a square-shaped motion. This theory has been widely supported, with some exceptions, by *in-vitro* POD tests. For instance, the results obtained by Saikko et al. (2004) in a CTPOD that used an elliptical sliding motion with different ARs as input, confirmed the validity of the unified model because the measured k factor was found to decrease with increasing ARs in the range of 1-5.5, above which the wear rate dropped to very small values. On the contrary, Turell et al. (2003) obtained the highest wear factor k for an AR of 2.33 instead of 1 as predicted by the unified model, however, for ARs above 2.33 the k factor dropped to values predicted by Wang's model. The foundations for this theory rely on the results obtained from a tensile test (Wang et al., 1997) where a sample of conventional UHMWPE presented an enhanced rupture strength along the stretching direction, and a lower rupture strength in the perpendicular direction. Moreover, scanning electron microscopy (SEM) images revealed the tendency of polymeric chains to align along the stretched direction. A way to attenuate the detrimental effects of orientation softening on the wear resistance of UHMWPE is to crosslink it, since the higher number of carbon-carbon chemical bonds between adjacent molecules will hinder more effectively the reorientation of polymeric chains (Edidin et al., 1999; Korduba and Wang, 2011; Saikko and Ahlroos, 1999).

Wang's unified model together with more recent and novel theories that comprise new cross-shear formulations (Strickland et al., 2012) have been implemented into numerical platforms such as finite elements (FE) or multi-body dynamics (MBD). Kang et al. (2008) implemented Wang's theory into a FE model with the scope of reproducing a POP test where the multidirectional motion of the pin lay in the range of $\pm$ 55°. The computed cross-shear was then linked to the experimental wear factor k by using a logarithmic relationship. Besides, this logarithmic relationship was used by Goreham-Voss et al. (2010) to study the wear of an intervertebral total disk replacement (TDR). Banks and Sawyer (2005) developed a model in which the cross-shear was estimated as a "spread" of sliding directions, where input parameters such as contact pressures and sliding directions were obtained from a MBD simulation of a POD device. Basically, the model gives a standard deviation of the spread of sliding directions normalised by the "worst case" of sliding motion (circular rotation). In a notable recent study, Petrella et al. (2012) have proposed a novel approach where the cross-shear is calculated incrementally during the cycle, and the intensity of cross-shear depends on the incremental changes in sliding direction. Their model differs from previous formulations in terms of its ability to distinguish between wear tracks similar in shape, and the no need to define a PMO as in Wang's model.

Intuitively, and as established by physical experimental observations, one would naturally expect that the multiscale semi-crystalline structure of UHMWPE (McGloughlin and Kavanagh, 2000) plays a significant role on its wear properties. POD wear tests (and their variants) have been very useful in unravelling some aspects of wear such as the critical effects of cross-shear motions or rate of change of curvature of the sliding path. Although POD tests can be used to infer certain hypotheses concerning damage and wear mechanisms in UHMWPE (Wang, 2001; Wang et al., 1996, 1997), they are, by nature, empirical and do not provide a direct understanding and mechanistic insight into the potential nano-/microstructural elastic and inelastic deformation mechanisms responsible for the observed wear rates or wear volume produced.

The aim of the present study is to assess, through FE-based *in silico* POD tests, the effects of motion paths in simulated multidirectional sliding motions on certain metrics related to the mechanical response of UHMWPE, and more particularly to the evolution of molecular chain alignment. To this end, an advanced microstructurally-motivated constitutive model of UHMWPE −the so-called Three Network Model (TNM) of Bergström and Bischoff (2011)− was implemented in a non-linear finite element environment capable of handling complex materials and contact conditions. This model, valid for arbitrary kinematics, accounts for the elastic and inelastic (i.e. viscoplasticity, cyclic plasticity) behaviour of UHMWPE. The concept of *anti-coaxiality* (explained in the next section) as a measure of deviation from mechanical isotropy of the molecular chains is introduced. Although no wear modelling is conducted in our study, the working hypothesis is that the evolution of the UHMWPE microstructure during multisliding POD tests can inform us on possible correlations between wear, sliding track characteristics and the micromechanics of UHMWPE. Ultimately, this information is meant to be exploited for the development of wear simulation tools with real *predictive* capabilities.

5.2 Materials and Methods

5.2.1 The Three Network Model

To describe the mechanical response of thermoplastic materials such as UHMWPE subjected to arbitrary deformations, Bergström and Bischoff (2011) developed an advanced microstructurally based constitutive model, the so called "Three Network Model". Its rheological representation includes three molecular networks A, B and C arranged in parallel. The description of the constitutive parameters of the model and the particular values used in the present study are provided in **Table 5.1**.

Table 5.1: List of input calibrated parameters of the TNM, which values refer to a ram-extruded GUR 1050 that was heat treated at 110 °C for 2 hours (Bergström and Bischoff, 2011)

TNM parameters	**Assigned value**	**Units**	**Description**
μ_A	200	MPa	Shear modulus of network A
λ_L	3.25	/	Locking stretch
k	6000	MPa	Bulk modulus
$\hat{\tau}_A$	3.25	MPa	Flow resistance of network A
a	0.073	/	Pressure dependence of flow
$m_a = m_b$	20	/	Stress exponential of network A
μ_{Bi}	293	MPa	Initial shear modulus of network B
μ_{Bf}	79.1	MPa	Final shear modulus of network B
β	31.9	/	Evolution rate of μ_B
$\hat{\tau}_B$	20.1	MPa	Flow resistance of network B
μ_C	10.0	MPa	Shear modulus of network C
q	0.23	/	Relative contribution of I_2 of network C

The initial viscoplastic response of network A (*amorphous* phase) and network B (*crystalline* phase) is activated through two separate energy mechanisms, and the large strain response is controlled by entropic resistance in network C. It is noteworthy that network C does not represent a particular material phase, but rather is part of the mechanical response of the material. Borrowing from finite plasticity concepts (Lubarda, 2004), the deformation gradients in networks A and B are multiplicatively decomposed into elastic and viscoplastic components, respectively as $\mathbf{F} = \mathbf{F}^e_A\mathbf{F}^\nu_A$ and $\mathbf{F} = \mathbf{F}^e_B\mathbf{F}^\nu_B$. The Cauchy stress in the non-linear entropic spring of network A is derived from a temperature-dependent version of the eight-chain model that was developed by Arruda and Boyce (1993):

$$\sigma_A = \frac{\mu_A}{J^e_A}\left(1 + \frac{\theta - \theta_0}{\hat{\theta}}\right)\frac{\mathfrak{L}^{-1}\left(\bar{\lambda^{e^*}_A}/\lambda_L\right)}{\mathfrak{L}^{-1}\left(1/\lambda_L\right)} dev\left(\mathbf{b}^{e^*}_A\right) + k\left(J^e_A - 1\right)\mathbf{1} \tag{5.1}$$

Where J^e_A, $dev\left(\mathbf{b}^{e^*}_A\right)$, $\bar{\lambda^{e^*}_A}$ are respectively the Jacobian of the elastic deformation gradient, deviatoric left Cauchy-Green deformation tensor and the effective elastic chain stretching of network A defined as :

$$J^e_A = det\left[\mathbf{F}^e_A\right] \qquad dev(\mathbf{b}^{e*}_A) = J^{e-2/3}_A\mathbf{F}^e_A\mathbf{F}^{eT}_A \qquad \bar{\lambda^{e*}_A} = \sqrt{tr(\mathbf{b}^{e*}_A/3)} \tag{5.2}$$

$\mathfrak{L}^{-1}$ is the inverse of the Langevin function $\mathfrak{L}^{-1} = coth\,(x) - 1/x$. The rate kinematics of network A is necessary to complete its constitutive description. The total velocity gradient of network A $\mathbf{L} = \dot{\mathbf{F}}\mathbf{F}^{-1}$ is decomposed into elastic and viscous contributions $\mathbf{L} = \mathbf{F}^e_A + \mathbf{F}^e_A \mathbf{L}^\nu_A \mathbf{F}^{e-1}_A = \mathbf{L}^e_A + \tilde{\mathbf{L}}^\nu_A$, where $\mathbf{L}^\nu_A = \dot{\mathbf{F}}^\nu_A \mathbf{F}^{\nu-1}_A = \mathbf{D}^\nu_A + \mathbf{W}^\nu_A$ and $\tilde{\mathbf{L}}^\nu_A = \tilde{\mathbf{D}}^\nu_A + \tilde{\mathbf{W}}^\nu_A$ and $\tilde{\mathbf{W}}^\nu_A$ being respectively the rate of deformation and spin tensors in the intermediate configuration. The spin tensor is prescribed ($\tilde{\mathbf{W}}^\nu_A = 0$) (Boyce et al., 1989) to remove ambiguity stemming from the non-unicity of $\tilde{\mathbf{L}}^\nu_A$ in the intermediate configuration. The rate of viscoplastic flow in network A is constitutively prescribed as $\tilde{\mathbf{D}}^\nu_A = \dot{\gamma}_A \mathbf{N}_A$ where $\dot{\gamma}_A$ is the deviatoric flow rate flowing in the direction $\mathbf{N}_A$ defined as:

$$\mathbf{N}_A = \frac{dev\,(\sigma_A)}{\sqrt{dev\,(\sigma_A : \sigma_A)}} = \frac{dev\,(\sigma_A)}{\tau_A} \tag{5.3}$$

where $dev\,(\sigma_A)$ is the deviatoric part of the Cauchy stress in network A ":" represents the double contracted product of two tensors. The flow rate is defined through a power law equation:

$$\dot{\gamma}_A = \dot{\gamma}_0 \left(\frac{\tau_A}{\hat{\tau}_A + aR\,(p_A)} \right)^{m_A} \left(\frac{\theta}{\theta_0} \right)^n \tag{5.4}$$

where $\dot{\gamma}_0$ is a term included for dimension consistency, $p_A = -dev\,(\sigma_A) : \mathbf{1}$ is the hydrostatic pressure, $\mathbf{1}$ is the second-order identity tensor, $R(x) = (x + |x|)/2$ is the ramp function, and $\hat{\tau}_A$, m_A, n are material parameters. Then, the velocity gradient of the viscoelasticity flow of network A is defined as:

$$\dot{\mathbf{F}}^\nu_A = \dot{\gamma}_A \mathbf{F}^{e-1}_A \mathbf{N}_A \mathbf{F} \tag{5.5}$$

The constitutive equations describing network B are similar to those presented for network A:

$$\sigma_B = \frac{\mu_B}{J^e_B} \left(1 + \frac{\theta - \theta_0}{\hat{\theta}} \right) \frac{\mathfrak{L}^{-1}\left(\bar{\lambda^{e^*}_B} / \lambda_L \right)}{\mathfrak{L}^{-1}\left(1/\lambda_L \right)} dev\left(\mathbf{b}^{e^*}_B \right) + k\,(J^e_B - 1)\,\mathbf{1} \tag{5.6}$$

However, the initial shear modulus μ_B in the Cauchy stress in **equation 5.6** evolves with plastic strain from an initial value of μ_{Bi} to a final value of μ_{Bf}, as formulated in the following equation:

$$\dot{\mu}_B = \beta\,[\mu_B - \mu_{Bf}]\,\dot{\gamma}_A \tag{5.7}$$

The Cauchy stress in network C is still based on the eight-chain unit cell topology of the Arruda-Boyce model (Arruda and Boyce, 1993), but with a first order $I^*_2 = \left[(\mathbf{b}^* : \mathbf{1})^2 - \mathbf{b}^{*\mathbf{2}} : \mathbf{1} \right] /2 = \left(I^2_1 - \mathbf{b}^{*\mathbf{2}} : \mathbf{1} \right) /2$ dependency:

$$\begin{aligned} \sigma_C = \frac{1}{1+q} \left\{ \frac{\mu_C}{J\lambda_{chain}} \left[\frac{\theta - \theta_0}{\hat{\theta}} \right] \frac{\mathfrak{L}^{-1}(\lambda_{chain}/\lambda_L)}{\mathfrak{L}^{-1}(1/\lambda_L)} dev\,[\mathbf{b}^*] + k(J-1)\mathbf{1} \right\} + \\ \frac{1}{1+q} \left\{ q \frac{\mu_C}{J} \left[I^*_1 \mathbf{b}^* - \frac{2I^*_2}{3} I - (\mathbf{b}^*)^2) \right] \right\} \end{aligned} \tag{5.8}$$

where $J = det\,[F]$, $dev\,(\mathbf{b}^*) = J^{-2/3}\mathbf{F}\mathbf{F}^T$ is the Cauchy-Green deformation tensor $\lambda_{chain} = \sqrt{\mathbf{b}^* : 1/3}$ the stretch of the entropic chains in network C, and q a parameter controlling the magnitude of the I_2-dependency. Because of the parallel network rheological arrangement the total Cauchy stress in the material is computed as the sum of the stress in each network $\sigma = \sigma_A + \sigma_B + \sigma_C$. The TNM is able to capture the strain-rate dependence, stress relaxation, creep and the energy loss during cyclic loading.

5.2.2 Molecular chain reorientation and concept of anticoaxiality

In an isotropic linear elastic material the strain and stress tensors are always coaxial (i.e. they have the same principal directions) (Vianello, 1996a). Vianello demonstrated that coaxiality of stress and strain tensors for all deformation was a sufficient condition for isotropy of hyperelastic materials (Vianello, 1996b). This result was exploited by Menzel (2007) to model and characterise remodelling anisotropic microstructural evolution in biological soft tissues. Menzel (2007) introduced a metric that quantifies the non-coaxiality of conjugated stress and stretch tensors:

$$A = \frac{||\,(\mathbf{S}\cdot\mathbf{C}) + (\mathbf{S}\cdot\mathbf{C})^T\,||}{||\mathbf{S}\cdot\mathbf{C}||} \tag{5.9}$$

where $\mathbf{S}$ is the second Piola-Kirchoff stress, $\mathbf{C}$ is the right Cauchy-Green deformation tensor and $skew\,(\bullet) = 1/2\left(\bullet - \bullet^T\right)$ represents the skew-symmetric part of a second-order tensor. In the case of isotropy strain and stress tensors are coaxial (i.e. their principal direction coincide) and $A = 0$, otherwise A is non null.

5.2.3 Finite element modelling of POD tests

Two series of virtual POD tests (studies 1 and 2) were considered in this work. The FE models were developed in a symbolic/numeric non-linear FE environment, AceGen/AceFEM (Korelc, 2002; Korelc et al., 2010) integrated in Mathematica ® (Wolfram Research, Inc., Champaign, IL, USA). First, the TNM (Bergström and Bischoff, 2011) was implemented as a user 8-noded trilinear interpolation element with a decoupled treatment of deviatoric and volumetric responses (de Souza Neto et al., 1996). Second, the POD setups were created using simple geometric descriptions and meshed as brick elements. Each POD setup consisted of a cylindrical UHMWPE pin sliding on a CoCrMo counterface under a constant compressive load (**Figure 5.1**). In the numerical studies, the mechanical response of UHMWPE to external loads was described by the TNM, where its 15 input parameters were calibrated for a GUR 1050 that was heat-treated at 110 °C for two hours (Bergström and Bischoff, 2011). Because of the low level of stress experienced, the metal counterface was assumed to be linear elastic with a Young's modulus of 200 GPa and a Poisson's ratio of 0.3 (Bitsakos et al., 2005).
The role of material texturing (anticoaxiality) on wear resistance of UHMWPE was investigated by means of *in silico* POD tests, where simulation input parameters such as shape of wear track, sliding velocity (**Figure 5.1**-a) and sliding distance (**Figure 5.1**-b) were varied.

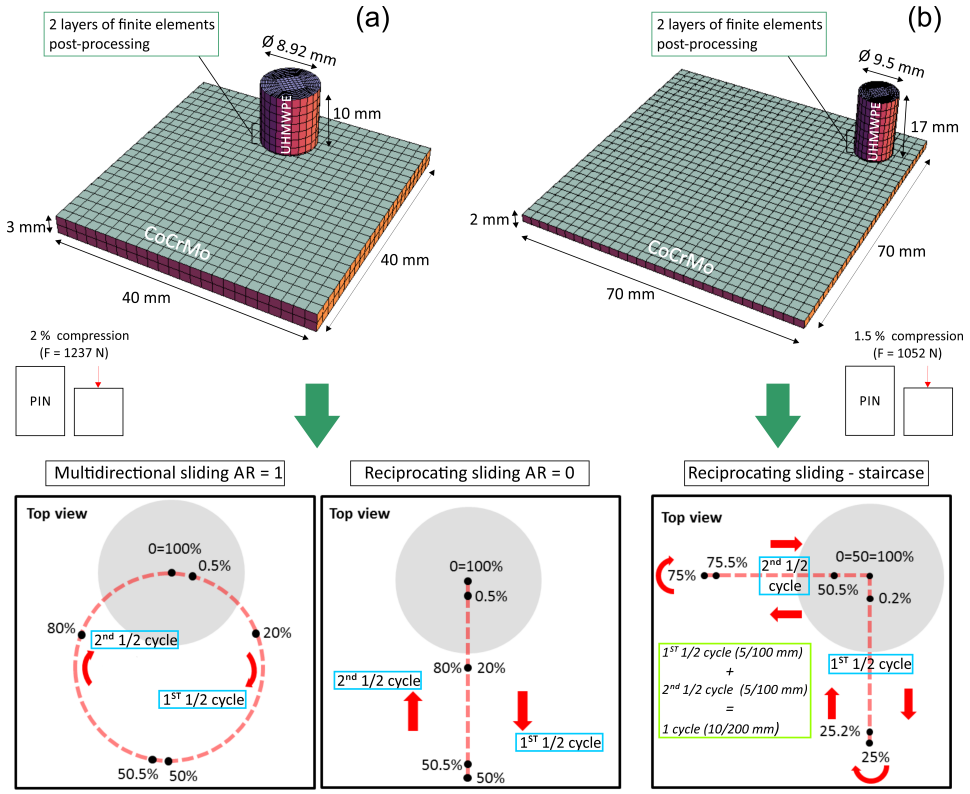

Figure 5.1: Finite element models to study the effects of different motion tracks, sliding velocities (a, study 1), and sliding distances (b, study 2) on the mechanical response of UHMWPE. Two finite elements layers of the UHMWPE pin are used for data post-processing. Bottom insets (a) and (b) illustrate the motion tracks input in study 1 and study 2, respectively. In both studies, the cylindrical pin is made of UHMWPE, while the counterbearing of CoCr.

5.2.3.1 Study 1

The first computational study (from now on referred as study 1) is based on the work of Saikko et al. (2004), who investigated the relationship between sliding track shape and wear of UHMWPE pins by varying the aspect ratio (AR) of an elliptical wear track. The extreme sliding scenarios were a circle (AR = 1) and a nearly straight line (AR = 388). The CTPOD test was conducted under lubricated conditions with cylindrically-shaped UHMWPE pins (8.92 mm in diameter) pressed by a vertical constant force of 70.7 N against circularly translating CoCr disks (30 mm in diameter and 10 mm in thickness). In each test, the cycle frequency was 1.02 Hz (0.98 s per cycle) while the maximum sliding velocity was 32 mm/s (**Table 5.2**, *Exp-1*). Since the track length per cycle varied according to the AR, different sliding velocity profiles were generated. For instance, the sliding velocity per cycle was held constant for an AR of 1, while it varied for an AR of 388 due to accelerations and decelerations of the pin occurring in proximity of changes in sliding direction. The total number of cycles in each test was $3 \cdot 10^6$ (**Table 5.2**, *Exp-1*).

Table 5.2: The parameters used in current simulations (*Sim-1a*, *Sim-1b*, and *Sim-2*) were taken from the published works of Saikko et al. (2004) (*Exp-1*) and Dressler et al. (2011) (*Exp-2*). The acronym AR stands for aspect ratio of the motion loci, while μ is the coefficient of friction. Sliding distance, sliding velocity, displacement, reference group, and rotation were abbreviated with Sl. dist., Sl. Vel., Displ., G., and R., respectively.

Type of study	**Wear track shape**	**Type of Load**	μ	**N. of cycles**	**Time per cycle (s)**	**Total time (s)**	**Sl. Vel. (mm/s)**
Exp-1	Circle (AR = 1)	Force 70.2 N	n/a	$3 \cdot 10^6$	0.98	$2.9 \cdot 10^6$	32 const.
(*curvature*)	Line (AR = 388)	Force 70.2 N	n/a	$3 \cdot 10^6$	0.98	$2.9 \cdot 10^6$	32 var.
Sim-1a	Circle (AR=1, R1)	Displ. 2 %	0.12	$1 \cdot 10^2$	0.98	98	32 const.
(*curvature*)	Line (AR=0, R0)	Displ. 2 %	0.12	$1 \cdot 10^2$	0.98	98	32 const.
Sim-1b	Circle (AR=1, R1)	Displ. 2 %	0.12	$1 \cdot 10^2$	0.49	49	64 const.
(*slid. vel.*)	Line (AR=0, R0)	Displ. 2 %	0.12	$1 \cdot 10^2$	0.49	49	64 const.
Exp-2	Line+90 °R(G5mm)	Force 330 N	n/a	$7.2 \cdot 10^5$	0.15	$1.1 \cdot 10^5$	64 const.
(*slid. dist.*)	Line+90 °R(G100mm)	Force 330 N	n/a	$2.4 \cdot 10^5$	3.12	$7.5 \cdot 10^5$	64 const.
Sim-2	Stair.- 10 mm	Displ. 1.5 %	0.08	72	0.15	11	64 const.
(*slid. dist.*)	Stair.- 200 mm	Displ. 1.5 %	0.08	24	3.12	75	64 const.

In order to fit the purposes of current computational studies, some experimental inputs were modified. The UHMWPE pin was compressed by a vertical displacement (displacement-driven simulation) of 2 % of its total length, which correspond to an applied force of 1237 N (**Figure 5.1**-a) if assuming a Young's modulus of 990 MPa (Kurtz, 2009; Bergström and Bischoff, 2011). This high deformation was applied with the aim of inducing an inelastic response of UHMWPE from the first sliding cycle, since only a limited number of cycles (100) were simulated due to high computational costs (**Table 5.2**, *Sim-1a*). The load was ramped in 10 steps of 0.1 s each for a total time of 1 s. Two wear tracks, a circle (R1) and a straight line (R0) with equal sliding distances of 31.4 mm, were simulated to study the relationship between sliding track shapes and changes in the stress response and microstructural properties of UHMWPE. The sliding distance and the sliding velocity (32 mm/s) were kept constant in both wear tracks.

An advanced smooth contact algorithm based on third-order Bézier patches (Lengiewicz et al., 2011; Stupkiewicz et al., 2010) was used to simulate the contact between the UHMWPE pin and the CoCr counterbearing.

To transmit enough force from the moving counterbearing surface to the UHMWPE wear surface so as to produce detectable chains realignment, a coefficient of friction three times higher than the conventional value of 0.04 (Godest et al. (2002)) for the couple UHMWPE/CoCr was applied (**Table 5.2**, *Sim-1a*). In reality, adhesive phenomena enhanced by the biological environment, not modelled here, would likely increase the apparent coefficient of friction between UHMWPE and CoCr. The trajectory of the motion loci was discretised into 200 points, where each point identified a precise spatial position (as a percentage of the track length) of the moving pin. However, following preliminary simulations, data were collected only at 6 locations, which were the most representative in terms of changes in material texturing due to chains realignment (**Figure 5.1**-a, bottom inset). The simulated CoCr counterface was a rectangle 40 x 40 x 3 mm in size rather than a disk as in the reference experiment (Saikko et al., 2004). The UHMWPE pin and CoCr counterbearing were respectively discretised into 1932 and 1152 elements, for a total of 3084 eight-noded hexahedral finite elements. Because wear is essentially a surface phenomenon, in the current studies only two FE layers (552 elements) of the base of the UHMWPE pin were used for data post-processing (**Figure 5.1**-a, top).

The effect of increasing sliding velocity on UHMWPE texturing was also investigated by using the same simulation set-up presented in study 1, but doubling the sliding velocity from 32 mm/s to 64 mm/s (**Table 5.2**, *Sim-1b*).

5.2.3.2 Study 2

The second computational study (study 2) is based on the experimental work of Dressler et al. (2011) where the variable nature of the wear rate measured in UHMWPE after a cross-shear event was demonstrated. Wear of two cross-linked UHMWPEs (GVF and XLK) was evaluated for similar motion tracks (**Figure 5.1**-b) having different sliding distances (groups 0 mm, 1 mm, 2 mm, 5 mm, 10 mm, 100 mm). The UHMWPE pins were cylinders 9.5 mm in diameter and 17 mm high, while the CoCrMo counterface was a disk 38.1 mm in diameter and 12.7 mm high. The pin slid at a speed of 64 mm/s in segments not longer than 5 mm under a compressive load of 330 N (**Table 5.2**, *Exp-2*). In the first half cycle, it reciprocated for n times to reach the targeted sliding distance, and immediately after it was sequentially stopped, unloaded from 330 N to 30 N, rotated by 90 degrees, and reloaded to 330 N. Once these operations were completed, the pin was ready to recommence sliding for n times in order to complete the second half cycle. For instance, in group 100 mm (Dressler et al., 2011) the pin covered a sliding distance of 100 mm in the first half cycle by reciprocating for 20 times in 5 mm increments (20 x 5 mm = 100 mm). When it was rotated and the load restored, it recommenced sliding for 20 times in 5 mm increments to complete the second half cycle (20 x 5 mm = 100 mm), for a sliding distance totalling 200 mm per cycle (1 cycle = $1^{st}\frac{1}{2}$ cycle + $2^{nd}\frac{1}{2}$ cycle = 100 mm + 100 mm = 200 mm), as shown in **Figure 5.1**-b (bottom inset). The experimental time, without accounting for the time spent in stopping and restarting the motion of the pin, was $1.1 \cdot 10^5$ s and $7.5 \cdot 10^5$ s for the 5 mm and 100 mm sliding cases, respectively (**Table 5.2**, *Exp-2*).

To the aims of the current study, both the kinematics and the set-up of the physical POD test were slightly modified in the FE model, and only the experimental groups of 5 mm and 100 mm were simulated. Besides, in order to faithfully replicate the physical experiment, but without adding complexity to the FE model, the input sliding motion took a "staircase" shape, which eliminated the 90 °C rotation and the load lift-off (**Figure 5.1**-b). Due to the abovementioned stop and restart phases occurring in the physical test, the pin experienced accelerations and decelerations that resulted in changes of sliding velocity at both beginning and end of a cycle. Again, in order to avoid unnecessary complexity for the purposes of the current study, the stop and restart phases were not included in the FE model, and the sliding velocity of 64 mm/s was assumed to be constant throughout the cycle. In the numerical model, the UHMWPE pin of 9.5 mm in diameter and 17 mm in height was compressed by vertical displacement equal to 1.5 % of its total length (applied force of 1052 N, see sub-subsection 5.2.3.1) against a rectangular counterface sized 70 x 70 x 2 mm (**Figure 5.1**-b). The trajectory of the motion loci of simulations 10 mm and 200 mm were discretized into 40 and 480 points, respectively. However, only the most representative locations (8 points) in the wear track in terms of changes in material texturing were reported, as depicted in **Figure 5.1**-b, bottom inset. The third-order Bézier contact algorithm was again used to enforce the contact between the pin and the counterface, but using a coefficient of friction of 0.08 for the couple UHMWPE/CoCrMo (**Table 5.2**, *Sim-2*). The experimental groups of 5 mm and 100 mm were replicated in current FE simulations, with limitations in the number of cycles due to highly computational cost. In the former study-case the pin covered a sliding distance of 720 mm (72 cycles), while in the latter case the distance was 4800 mm (24 cycles), as illustrated in **Table 5.2**, *Sim-2*. The FE model had a total of 3108 eight-noded hexahedral elements, which were distributed between the pin and the counterface into 2208 and 900 elements, respectively. For the reasons already mentioned for study 1, two FE layers (552 elements) of the pin in the immediate proximity of the contact surface were used for data post-processing (**Figure 5.1**-b, top inset).

5.3 Results

The focus of the present study is on the micromechanical/microstructural evolution of UHMWPE in relation to multidirectional sliding. The objective was to study how multidirectional sliding in POD experiments affects the micromechanics of UHMWPE macromolecular chains using an advanced constitutive model accounting for time-dependent elastic and inelastic deformations. In order to examine the effects of multidirectional sliding several *metrics* (or *response variables*) were chosen:

- von Mises stress: this a scalar quantity reflecting the level of stress at any point within the material and can also be viewed as a tensorial norm for the particular measure of stress under consideration. If σ_1, σ_2 and σ_3 are the principal values of the Cauchy stress then the von Mises stress is:

$$\sigma^{vonMises} = \sqrt{\frac{1}{2}[(\sigma_1 - \sigma_2)^2 + (\sigma_2 - \sigma_3)^2 + (\sigma_3 - \sigma_1)^2]} \tag{5.10}$$

  This quantity is relevant as it is an indication of whether the material is likely to go into the plastic regime or not, and, in a real world context, indicates likelihood of material failure.

- The plastic multiplier (or plastic strain) γ_A in the rheological network A (amorphous phase).
- The plastic multiplier γ_B in the rheological network B (crystalline phase).
- Anticoaxiality of the stress and deformation tensors A which is a measure of structural anisotropy (see previous section).

For each series of multidirectional sliding finite element analyses the four metrics were assessed at specific points of the sliding tracks (i.e. 0.5, 20, 50, 50.5, 80 and 100 % of the path) and for the two layers of finite elements constituting the base of the UHMWPE pin (i.e those elements experiencing significant stress and strain). These particulars points of the sliding track were chosen as it was at those points that significant variations in the metrics were observed. Instead of only reporting peak values, each metric statistics was assessed (mean, median, minimum, maximum and interquartile ranges) and reported in box-and-whisker plots.

5.3.1 Study 1

In **Figure 5.2** the statistics for each sliding test (R0: aspect ratio of the wear track = 0; R1: aspect ratio of the wear track = 1) are reported for the four kinetic ($\sigma^{vonMises}$), kinematic (γ_A and γ_B) and microstructural (A) metrics.

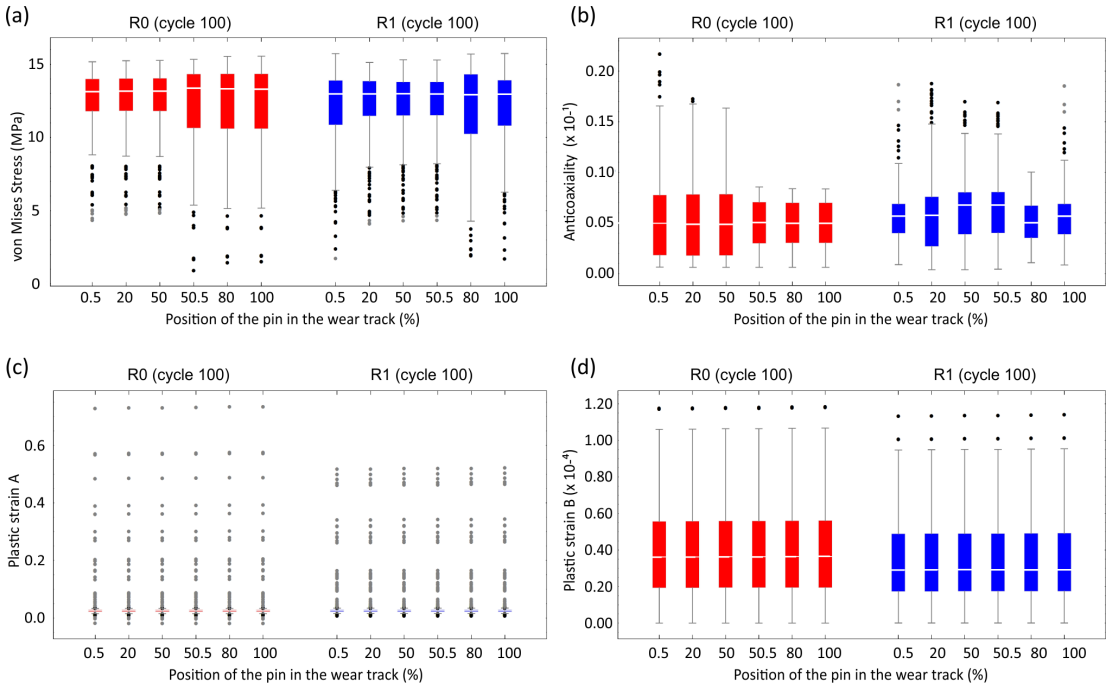

Figure 5.2: Box-and-whiskers plots of metrics for the UHMWPE pin subjected to reciprocate (R0) and multidirectional (R1) sliding. The horizontal axis indicates the position of the pin in the wear track, which is given in %. Minimum, maximum, second and third quartiles of the metrics are reported together with the median. These data refer to cycle 100 of study 1.

The median and maximum value of the von Mises stress (about 15 and 13 MPa respectively) are very similar in both tests (R0 and R1) and all along the sliding track (from 0.5 to 100 %) (**Figure 5.2**-a). However, the minimum values are not so homogeneous within and between each test. For the R0 test, in the first half of the sliding track the von Mises stress values hardly drop below 5 MPa while they drop to about 1 MPa in the other half. This seems to indicate that the reciprocating rectilinear sliding induces a radical stress relaxation in the polymer when the direction of sliding is reversed. The inter-quartile range is also larger in this case. However, at cycle 100 one would expect no differences in stress distribution between the first half cycle (0.5−50 %) and the second half cycle (50.5−100 %). This could be attributed to variations in the elastic response of the UHMWPE pin when it reciprocates back (change in sliding direction of 180 °), resulting in a "stepwise" stress response at these specific points (**Figure 5.2**-a, **Figure 5.3**-a).

There is more noticeable difference in anticoaxiality median and maximum values when comparing the two tests R0 and R1 (**Figure 5.2**-b) and this clearly highlights the fact that the different geometric characteristics of the sliding track have an effect on the UHMWPE microstructure. For the rectilinear track (R0) the median and minimum anticoaxiality values are fairly constant. Like for the von Mises stress there is a distinct behaviour of the extreme values (here it is the maximum instead of the minimum) between the first and second half of the sliding path. Higher maximum anticoaxiality values (double) are obtained in the first half when compared to the values sampled between 50 and 100 % of the sliding path.

For the R1 test mean anticoaxiality values significantly increase at the transition between the two half of the track (before 50 %) and then decrease. When compared to the R0, this result demonstrates that anticoaxiality is a good candidate metric to pick up differences in the evolution of the microstructure of UHMWPE according to the type of sliding motion (and so the type of deformation history) experienced by the polymer pin.

The median and minimum values of the plastic deformation in network A are virtually identical in both tests R0 and R1 and are fairly constant along the sliding path (**Figure 5.2**-c). Higher maximum plastic deformations in network A are observed for test R0 when compared to test R1 showing that a zero curvatures sliding path produces a state of deformation more likely to produce plastic flow in UHMWPE when compared to a non-zero constant curvature sliding path (R1). Overall, plastic deformations can exceed 0.7.

Plastic deformations in network B (crystalline phase) are very small, in the order of 10^{-5} (**Figure 5.2**-d). For both experiments, the 25 to 75 percentile values are constant along the sliding path but, in the case of R1, the median values are over 20 % smaller that for the R0 case. Higher maximum plastic deformations are also observed for the R0 case.

Similarly to **Figure 5.2**, the four response variables of interest (von Mises stress, plastic deformations and anticoaxiality) are reported in **Figure 5.3**. The main difference is that instead of reporting the complete distribution (mean, quartiles, extrema) only the trimmed means are reported and, instead of one, two sliding rates are considered (32 and 64 mm/s) so that any rate sensitivity of those metrics could be captured. Overall, in the four plots (in **Figure 5.3**-a-b-c,-d) the trend of the variations along the sliding path is not affected by the sliding rate, only the magnitude is. However, anticoaxiality is weakly affected by sliding rate.

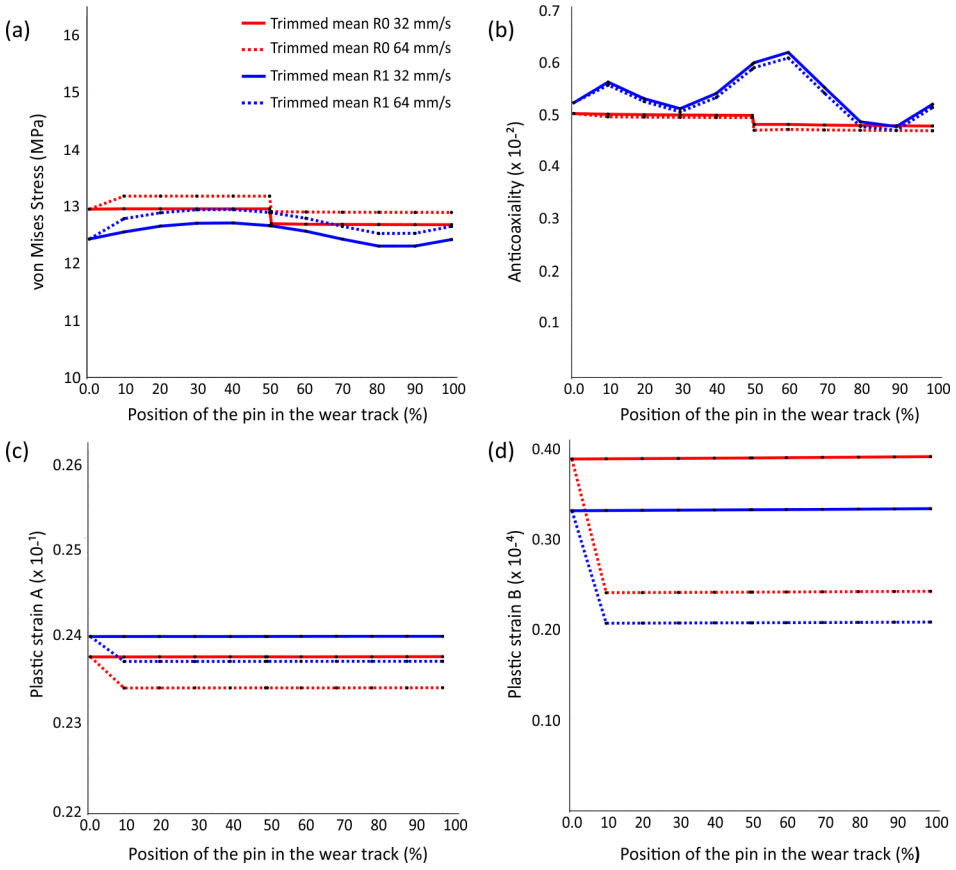

Figure 5.3: Plots of metrics for the UHMWPE subjected to reciprocate (R0) and multidirectional sliding (R1), and sliding velocities of 32 mm/s and 64 mm/s. The data in figure, in terms of trimmed mean, refer to cycle 100 of study 1 (**Figure 5.1**-a).

The evolution of the trimmed mean for the four output metrics as a function of number of sliding cycles is presented in **Figure 5.4**. For both tests (R0 and R1) von Mises stress decreases as the number of sliding cycles increases (**Figure 5.4**-a) and so are plastic deformations in both rheological networks (**Figure 5.4**-b, **Figure 5.4**-c). However, networks A and B exhibit different behaviours: plastic deformations in network A reach a slowly increasing plateau after 25 cycles while plastic deformations in network B don't reach a similar steady state even after 100 sliding cycles. The evolution of anticoaxiality seems to be positively correlated with that of plastic deformations in network A (**Figure 5.4**-d).

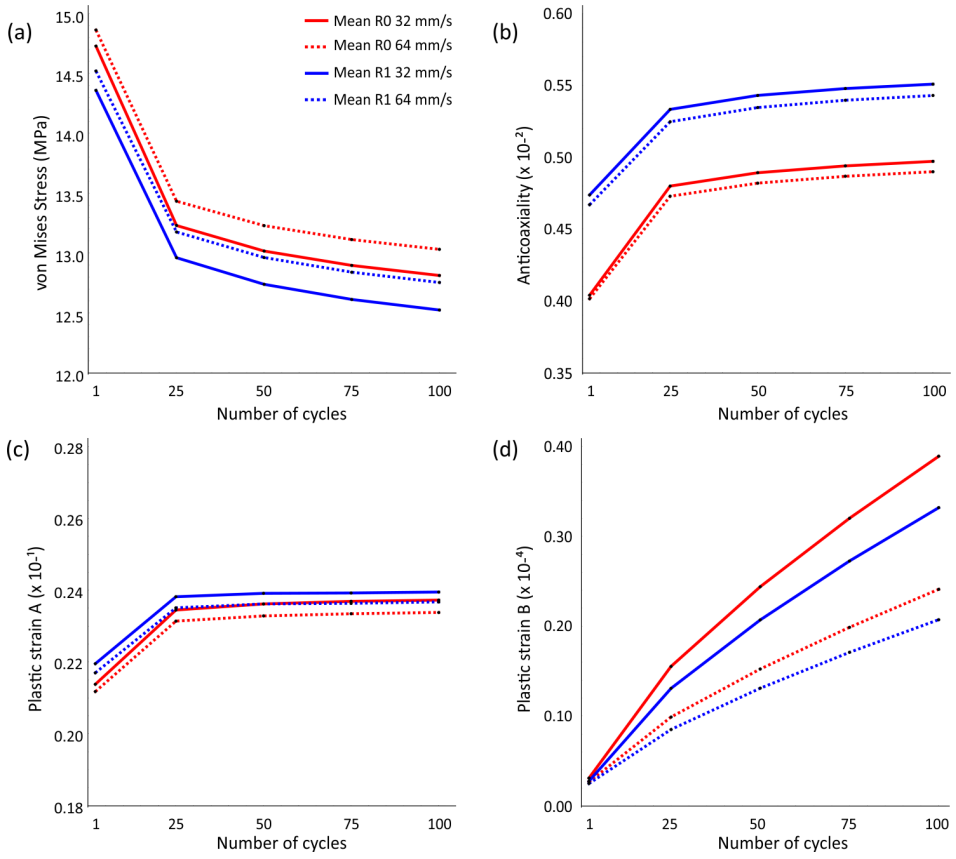

Figure 5.4: Evolution of metrics with increasing number of cycles (or time) for UHMWPE samples subjected to sliding velocities of 32 mm/s and 64 mm/s. The curves are obtained by computing the mean of the trimmed means per cycle (each point of a curve correspond to a trimmed mean value computed in a single cycle).

5.3.2 Study 2

Similarly to **Figure 5.2**, the four response metrics are reported as a function of the position in the sliding path for both the 10 and 200 mm sliding paths (**Figure 5.5**). Overall, both tests exhibit the same degree of skewness. This is expected as the motion paths differ only on their length, not shape (see **Figure 5.1**-b, bottom inset). Higher von Mises stresses are observed for the 10 mm path (**Figure 5.5**-a). There are noticeable differences in the anticoaxiality values between both tests from the first to the fourth quartile (**Figure 5.5**-b). Fluctuations in anticoaxiality are more extreme for the 200 mm sliding path suggesting that the sliding distance may play a role in molecular chain realignment for the particular type of sliding track considered in the computational experiment. In both tests the four quartiles of the value of plastic deformation in network A remains virtually constant along the sliding path and nearly identical in both cases. In the 200 mm track higher maximum values are consistently observed (**Figure 5.5**-c). More drastic differences between the two tests are obtained for the plastic deformations in the crystalline phase of UHMWPE (rheological network B) where values three times higher are observed for the 200 mm sliding motion. In both cases the distribution of plastic deformation in network B are mostly constant along the sliding track.

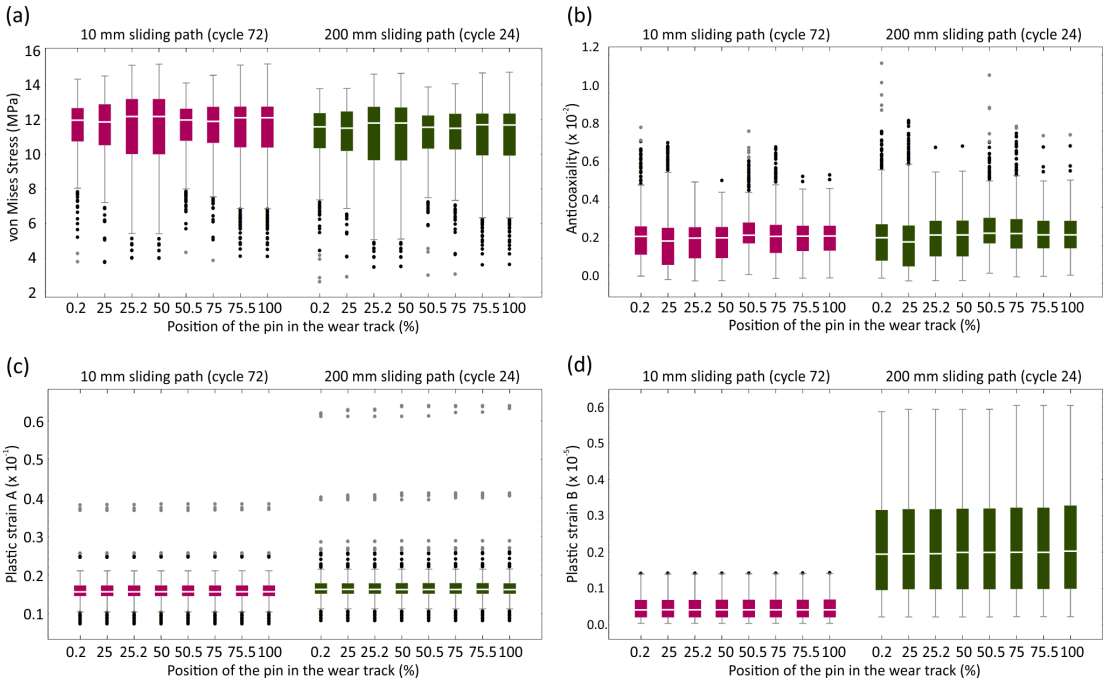

Figure 5.5: Box-and-whiskers plots of metrics for UHMWPE samples sliding in similar articulation paths (staircase-shaped wear track) having sliding distances of 10 mm and 200 mm. Quartiles, outliers, and far outliers are reported in figure.

The trimmed mean values of the four output responses as a function of the number of sliding cycles for both tracks (10 and 200 mm) are depicted in **Figure 5.6**. Each plot is augmented by an inset bar chart representing the same respective metric averaged over the total number of cycles (72 and 24 cycles for respectively the 10 and 200 mm tracks). Bar charts representing the same quantities but averaged over the total cumulative sliding distance (720 and 4800 mm for respectively the 10 and 200 mm tracks) rather than the number of cycles are provided in **Figure 5.7**.

It is noteworthy that the cumulative sliding distance refers to the sliding distance covered by the UHMWPE pin in 1 cycle multiplied by the total number of cycles (i.e. cumulative sliding distance = 10/200 mm x 72/24 cycles = 720/4800 mm), while the distance between reversal is half the cycle (i.e. 5/100 mm).

For the four metrics, apart from the von Mises stress (**Figure 5.6**-a), the longest motion path (200 mm) produces the largest values (**Figure 5.6**-b,-c,-d) as a function of the number of cycles. This is also reflected in the associated inset bar charts. All metrics display a notable change in slope occurring at cycle 18 and 6 for respectively the 10 and 200 mm sliding tracks apart from the plastic strain in network B (**Figure 5.6**-d). The distance between turns in the sliding path has a dramatic effect on this output response. Deviation from a state of coaxiality between stress and strain tensors (indicating evolution from mechanical isotropy to anisotropy) increases with the sliding distance between turns (**Figure 5.6**-b).

The von Mises stress, plastic strains in the amorphous (network A) and crystalline (network B) phases and the anticoaxiality are inversely proportional to the cumulative sliding distance, or more probably correlated to it. The distance between turns of the sliding path might be the causal factor rather than the sliding distance.

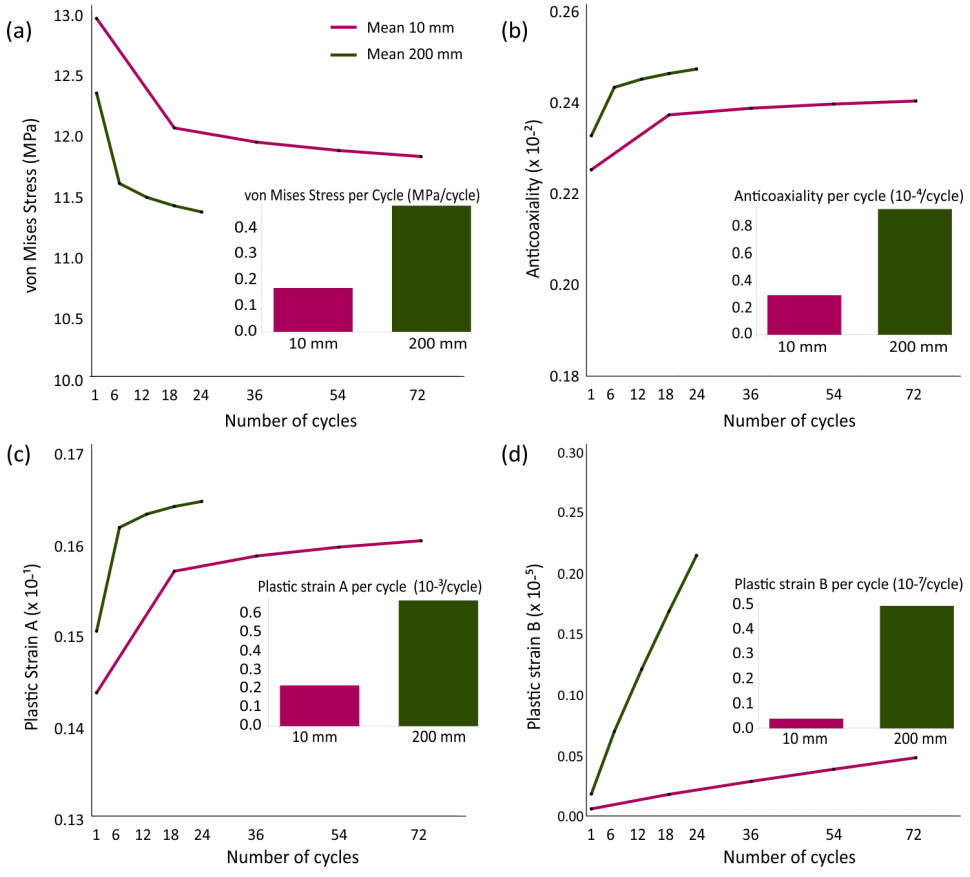

Figure 5.6: Evolution of metrics with increasing number of cycles (or time) for a UHMWPE pin subjected to siding distances of 10 mm and 200 mm. Bar charts were obtained as the ratio between the average of the means that define the trend of a single cycle in (each point in the curves), and the total number of cycles, which were 72 and 24 for cases 10 mm and 200 mm, respectively.

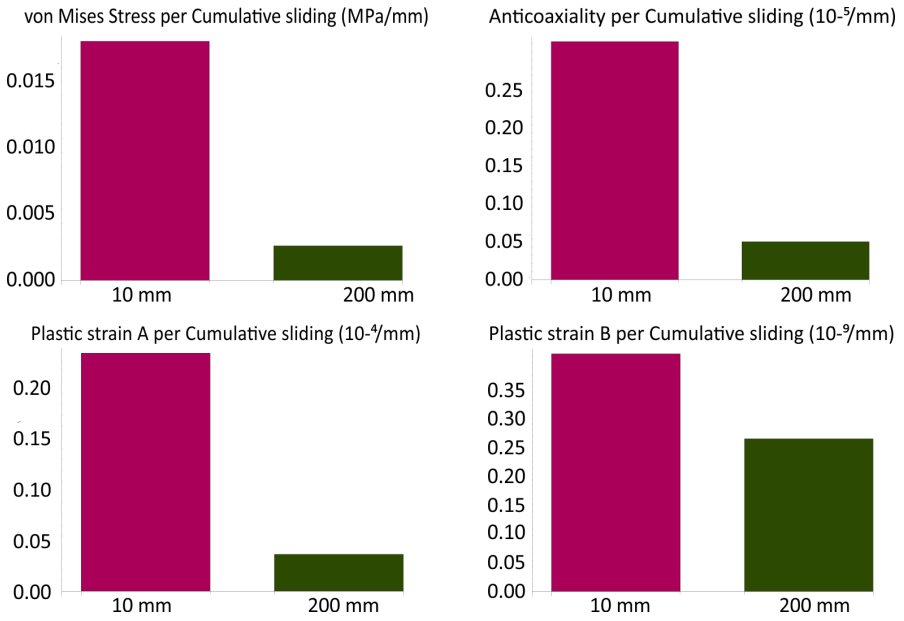

Figure 5.7: Bar charts representing each metric with respect to the cumulative sliding. They were obtained as the ratio between the average of the means that define the trend of a single cycle (each point of curves in **Figure 5.6** correspond to a cycle), and the total sliding distance, which were 720 mm and 4800 mm for the cases of 10 mm and 200 mm, respectively.

5.4 Discussion

For the linear path sliding motion, unlike the circular path, the maximum principal strain vector which represents the first eigenvector of the strain tensor is characterised by a constant (unsigned) direction. In the literature, this vector has also been termed "shear vector" because of its mechanical nature and role in cross-shear motions (Davey et al., 2004) in the context of UHMWPE wear (Wang, 2001; Wang et al., 1997). As intuitively hypothesised by several researchers and verified experimentally, linear sliding motions have the effect of inducing UHMWPE polymer chain realignment which increases the degree of anisotropy in the material microstructure. In turn this results in strain hardening (Wang, 2001; Wang et al., 1995, 1997) which correlates with low wear rates.

For the linear sliding track median values of anticoaxiality are pretty constant over each half-length of the cycle (**Figure 5.2**-b). The spread of anticoaxiality values is higher in the first half of the cycle suggesting that this is the part of the cycle where the molecular chains are recruited to resist the load applied to the UHMWPE pin. At 50 % of the sliding motion a drop in the trimmed means of von Mises stress (**Figure 5.3**-a) and anticoaxiality (**Figure 5.3**-b) indicates that there is an elastic stress relaxation mechanism at play when the shear vector reverses its direction. For the linear path the rate of variation of the velocity vector of the pin is zero (infinite radius of curvature, zero curvature) except at 0 and 100 % when the sliding direction is reversed while the variation is a non-zero constant for the circular sliding track. In this latter case, the shear vector acting on the contact surface of the UHMWPE pin is constantly changing inducing cross-shear motions which are known to lead to strain softening (Wang, 2001; Wang et al., 1995, 1997, 2012a). Moreover, given the time-dependent nature of the constitutive formulation of the TNM, the response of the material is conditioned by non-instantaneous activation mechanisms: it takes a finite amount of time for molecular chains to stretch/contract and deform the basic micromechanical unit cells of the eight-chain model (Arruda and Boyce, 1993). Coaxiality or anticoaxiality of the strain and stress tensors are therefore transient phenomena that evolve along the sliding path. If the shear vector varies continuously (Test R1) these two metrics will also exhibit a transient response as observed in the finite element simulations (**Figure 5.2**-b, **Figure 5.3**-b).

When the pin reaches 50 % of the path the shear vector experiences a 180 degrees phase shift compared to its direction at 0 %. This is therefore a significant mechanical event acting on the UMWPE microstructure. As the pin slides from 0 to 50 % the molecular chains progressively deviate from a state of initial quasi-isotropy (anticoaxiality monotically increases to reach a maximum value at 50 %) and then get back to their initial value of anticoaxiality. This is clearly evidenced in **Figure 5.2**-b. Plastic deformations (**Figure 5.2**-c, **Figure 5.2**-d) don't seem to be sensitive to the position along the sliding path except in the first 10 % of the sliding track if the sliding rate is doubled (**Figure 5.3**-c, **Figure 5.3**-d). This suggests that, for the particular conditions simulated, anticoaxiality mainly arises from elastic deformations or that small plastic deformations are sufficient to trigger noticeable microstructural rearrangements.

Wear of UMWPE is correlated with the curvature of the sliding track (Wang et al., 2012a): increasing the radius of curvature (i.e. decreasing the curvature) will result in reduced wear rate per sliding distance. However, as pointed out by Wang et al. (2012a), decreasing the curvature of the sliding path linearly increases the sliding distance per motion cycle, and in turn, this causes a proportional increase in the wear per cycle (Dressler et al., 2011). This implies that caution is required in interpreting *in vitro* an *in silico* tests examining wear or, like in the present study, micromechanical deformation mechanisms that could be correlated to wear. Results illustrating this concept are provided in **Figure 5.6** and **Figure 5.7** where the bar chart trends are reverse depending on whether they represent data per number of cycles or per sliding distance.

Figure 5.6 highlights the evolution of the response variables with the number of sliding cycles. The mechanical behaviour of UHMWPE (in reality and in the TNM formulation) is governed by inelastic phenomena which depend on the stress/strain history of the material. For the particular conditions tested in the computational analyses, it appears that the evolution of stress and deformation mechanisms can be broken in two stages : (1) a sharp increase (**Figure 5.6**-b, **Figure 5.6**-c) / decrease (**Figure 5.6**-a) followed by respectively a very moderate increase/decrease exhibiting a plateauing response. The first few sliding cycles (before the trend transition) are critical to condition the subsequent response of the material.

In the second computational study, the two sliding track differ by their length but both feature the same number of turns (90 degrees rotation) per cycle (**Figure 5.6**). When compared to the results of the 200 mm track the four output responses are smaller for the 10 mm track when normalised by the number of cycles but larger when normalised by the cumulative sliding distance.

In their experimental study, Dressler et al. (2011) found that the average wear per cycle increased with the sliding distance between turns up to 5-10 mm for both GVF^{TM} and XLK^{TM}, after which the trend plateaued. The authors provide evidence that the wear of moderately crosslinked UHMWPE varies along a sliding path. This is in contrast to the premises of the Archard's law of wear which states that wear is linearly related to sliding distance (Archard, 1953). The computational results corroborate the increase in wear rate per cycle with increasing sliding distance.

The unified theory of wear proposed by Wang (2001) predicts the transverse intermolecular splitting or rupture of oriented UHMWPE fibrils occurring as soon as a secondary motion is introduced. For example, if a UHMWPE sample slides against a CoCrMo counterbearing along a squared sliding path A x B, frictional energy is dissipated in both A and B directions. When A $<$ B, accordingly to Wang's theory, direction B becomes the principal sliding direction of motion, while A the secondary. The motion along the direction B leads to material hardening (molecular chains realignment) and low rates of wear, while motion in the secondary direction leads to material removal by intermolecular splitting (Turell et al., 2003). In the case of hip and knee joints these secondary motions are respectively abduction/adduction and internal/external rotation.

Higher von Mises stresses are produced for the 10 mm track (**Figure 5.6**-a). Several reasons can be attributed to this observation. The distance between turns for the 10 mm sliding track is smaller than that of the 200 mm. This means that molecular chain realignments and stress relaxation effects have less distance (and so time) to develop which leads to a lower mismatch between the principal axes of the stress and strain tensors (i.e. decreased anticoaxiality).

This presents an interesting parallel with the hypothesis of Wang et al. (2012b) in a paper looking at wear induced by multidirectional sliding, from a modelling and experimental viewpoints.

The authors propose that the curvature of the sliding circle acts as a cross-shear multiplier for *instantaneous* wear rate. The TNM features a critical micromechanical constitutive parameter, the so-called *locking stretch*, which correspond to the stretch at which molecular chains have reached their *contour* (or maximum) length, beyond which no further extension is possible (see **Table 5.1**). In all the simulations, the locking stretch was never reached but as the stretch in the material monotically increases towards the locking stretch there is a substantial strain hardening effect (Arruda and Boyce, 1993; Bergström and Bischoff, 2011) which could be magnified by change of direction over a smaller distance (10 mm).

The cross-shear events (90 and 180 degrees turn) are noticeable in the response of the von Mises stress, plastic deformations and anticoaxiality as they occur at 25, 50 and 75 % of the sliding track (**Figure 5.5**). Each of these changes of sliding directions induces an immediate reorientation of the principal stress directions while the principal strain axes adapt more gradually.

In **Figure 5.6** one can observe that the von Mises stress, anticoaxiality and plastic deformations in both rheological networks A and B are higher when the UHMWPE pin covers longer sliding distances. Although a higher level of anisotropy (i.e. increased anticoaxiality) might be an indicator of greater wear resistance of UHMWPE (Wang et al., 2012b,a, 1997), the longer sliding distance covered in the 200 m track might enhance the likelihood of material damage through higher values of von Mises stress and so plastic deformations in both rheological networks.

In their experimental POD testing, Saikko et al. (2004) considered 10 ellipses (aspect ratio varying between 1.1 and 11), a circle and a straight line as sliding paths. These authors found that the wear factor of the Archard's law of wear (Archard, 1953) was maximum for a circular path (by about an order of magnitude) compared to a line path. Although, the computational study presented in this paper does not explicitly model the wear of UHMWPE some direct correlations between wear rate/volume and von Mises stress, plastic deformations and anticoaxiality could be established. After all, wear is a complex cascade of events driven by and affecting the microstructure and deformation modes of a given material.

Our results suggest that anticoaxiality is potentially a pertinent indicator of microstructural alterations of UMWPE in relations to sliding motions used to study wear. The measure of anticoaxiality was based on total deformation, but in a future study it would be interesting to separate out the elastic and plastic parts to quantify their relative contribution to material anisotropy in terms of molecular chains realignment.

Future studies should consider the design of relevant physical experiments that could validate micromechanical/molecular deformations mechanisms observed via the use of advanced numerical constitutive models such as the TNM. The true usefulness of these models will be ultimately put to the test by assessing their predictive capabilities.

It is in the authors' opinion that future wear simulation tools will consist of mechanistic physics-based computational algorithms accounting for the various structural scales of UHMWPE and their mutual interactions. Wear will be predicted not as a system property but rather as an intrinsic constitutive behaviour driven by the physics of the material and its loading history rather than by applying empirical rules which do not reflect the real physics of the problem (cf. Archard's law).

It has been demonstrated that chemical and mechanical interactions between the lubricating fluid and the contact surface of the UHMWPE component of joints prosthesis occur *in vivo* (Costa et al., 1998). For instance, substances contained in the synovial fluid such as proteins and lipids are absorbed at the articulating surface of UHMWPE, and then diffused inside.

The combined effect of mechanical stresses and lubricating fluid produces a series of chemo-physical alteration of the articulation surface of UHWMPE, resulting in chemical wear. All simulations presented in this work assumed a "dry" condition at the contact between the UHMWPE sample and the counterbearing. Therefore, it is desirable that future constitutive models look at the coupling between mechanics and chemistry for a better insight into the nature of wear mechanisms.

The computational models assumed a constant friction coefficient along the sliding path. Experimental work on UHMWPE suggested that the apparent coefficient of friction between UHMWPE and the counterbearing surface varies according to the curvature of the sliding motion (Dunn et al., 2008). It would be relevant to include this phenomenon as a physics-based feature in future constitutives model of UHMWPE. Moreover, the coefficient of friction could also be made dependent upon properties such as roughness, contact pressure and wear factor, as suggested by Wang et al. (2001).

The TNM is a highly nonlinear time-depended mechanistic model that requires a finite amount of time to produce microstructural changes in the contact surface of UHMWPE during sliding. If the number of sliding cycles is not sufficiently high, it is expected that the interplay between creep, relaxation and plastic deformation effects will not precisely capture microstructural changes in UHMWPE. Besides, excessively high deformations applied to UHMWPE crystallites leads to the formation/release of wear particles from the surface of UHMWPE. This type of damage mechanisms is currently not accounted for in the TNM formulation but could be implemented provided adequate experimental data are available. These aspects should be investigated in further studies.

5.5 Conclusions

In this work, the micromechanics of UHMWPE under various sliding motions was investigated through *in silico* POD tests featuring a microstructurally-motivated constitutive model capable of accounting for microstructural evolution of polymer chains. The objective was to explore possible correlations between wear, sliding track characteristics, and the micromechanics of UHMWPE by considering several response variables such as anticoaxiality, von Mises stress, and plastic strains of both crystalline and amorphous phases of the semi-crystalline polymer.

Results indicate that anticoaxiality is a metric capable of capturing differences in UHMWPE microstructure evolution according to the type of sliding motion experienced by the polymer. A critical factor associated with sliding motions is the instantaneous shear vector acting on the contact surface of the UHMWPE pin while sliding. The observed transient response under multidirectional sliding points towards the occurrence of a more substantial change in the microstructure of the articulating surface of UHMWPE than that during unidirectional sliding. Under this motion, molecular chains experience a constant change in orientation, which might ultimately reduce the UHMWPE resistance to wear and delamination. This is in agreement with the hypothesis of (Wang, 2001; Wang et al., 1997) where multidirectional sliding leads to orientation softening and so high wear rates. Our results also indicate that long motion paths increase the likelihood of UHMWPE damage through high values of von Mises stress and plastic deformations in both crystalline and amorphous phases. These findings need to be further investigated through dedicated physically-based tests.

Chapter 6

Discussion and conclusions

This chapter examines the outcomes of this PhD work, its limitations, and propose avenues for future research that will build upon this work.

6.1 Summary of the thesis outcomes

The main objective of this PhD work was to investigate the visco-dynamic properties of the UHMWPE component commonly used in partial and total knee replacements in order to gain a better insight into the micro-mechanisms of deformation that ultimately lead to wear.

The entire project has been tackled as a series of experimentally-based computational studies with increasing level of complexity.

The complex mechanisms of deformation occurring in UHMWPE are closely related to its semi-crystalline structure. The occurrence of mechanisms of deformation in the amorphous phase or in the crystalline phase depends on the level of strain applied to UHMWPE. In a controlled laboratory environment, UHMWPE behaves elastically at small strains, visco-elastically at moderate strains, and visco-plastically at large strains (Kurtz, 2009). Therefore, the nature and extent of changes in the characteristics of the articulating contact surface of the UHMWPE component in knee joints will depend on the level of deformation applied to it. Based on these observations, it was proposed to study the respective role of elastic, viscoelastic (creep), and plastic deformations of a UHMWPE tibial insert under compression on the CA characteristics and associated kinematic and kinetic quantities such as deformation and CP. This was investigated through the realisation of two different numerical studies corroborated by *in vitro* compression tests, which are described in chapter 3 and chapter 4.

Knee joints in young and active patients are normally subjected to higher frequency loading/unloading cycles than those of less active older patients. In the latter case, the UHMWPE components will experience longer resting periods over which the material recovers part of the deformation. It was observed in the study of chapter 3, that 900 s after removing the load on the UHMWPE tibial insert, residual deformations were still present. Therefore, UHMWPE requires periods longer than fractions of seconds to fully recover the deformation.

This implies that UHMWPE components implanted in young patients might experience a wider and stronger range of visco-dynamic effects altering inelastic deformations of the insert surface. These complex loading conditions and their effects on surface geometry might in turn lead to a higher likelihood of excessive stress in the material which, at last, will produce wear.

Results from these physics-based computational studies indicate that viscoelstic deformations strongly affect the extent of CA at the articulating surface of UHMWPE and for all physiological loads (Quinci et al., 2014). The predicted CA, and so the inelastic deformations on the contact surface of UHMWPE, increased when a time-dependent mechanism of deformation such as creep was included in numerical models. The majority of the area in contact between the UHMWPE insert and the femoral component was measured within the first second of loading, afterwards the CA slowly increased towards a constant value (**Figure 4.3**) over time. It can be assumed, from the previous observation, that the CA is a time-dependent quantity that constantly modify the geometry of the articulating surface of UHMWPE (Rullkoeter and Gabriel, 2000). This condition leads to knee kinematics that are different from those optimal which the knee implant was originally designed for, accelerating the wear process of UHMWPE. Therefore, failing to include creep deformations in computational models will lead to underestimating the effects of the joint kinematics on the wear damage of UHMWPE.
In the study reported in chapter 3, a difference in CA distribution was observed between condyles (**Table 3.2**), which is likely due to the pliancy effect on the femoral arm of the AMTI simulator. The FE model replicated as accurately as possible the exact dimensions and geometrical tolerances of the AMTI setup in order to obtain the same pliancy effect as that seen *in vitro*.
In the study of chapter 4, significant variations of the deviation angle for the CA were measured in the physical experiments (**Figure 4.4**), which could be explained by the misalignment of the tibial insert and the femoral component or artefacts introduced by the presence of the TekScan™ pressure film. Therefore, when designing a physical test, one must account for all those variables linked to both measurement system and force (or displacement)-feedback sensors that can either induce smaller/larger deformations on UHMWPE compared to those occurring *in vivo* or introduce artefacts in the measurements.

At high compressive loads inelastic deformation mechanisms dominate the mechanical response of UHMWPE components by changing the surface geometry (i.e. penetration depth and so CA) and therefore the CP. In all studies, viscoelastic models predict lower CPs than those of purely elastic and elastoplastic models, showing that creep deformations have a significant effect on the measured and computed CP at the surface of the UHMWPE component. However, one can deduce that viscoelastic deformations occurring on UHMWPE lead to two effects that work against each other.
On one hand, viscoelastic deformations leads to lower stresses at the contact surface of the UHMWPE tibial insert as a result of larger CAs. In a wear-prediction context this would mean that viscoelastic models would predict a lower wear volume. In fact, wear algorithms based on Archard's law of wear (Archard, 1953) link the volumetric wear (W) to an empirical factor (k), sliding distance (s), and CP (i.e. $W = k \cdot CP \cdot s$).
On the other hand, viscoelastic deformations will also change the conformity of the contact surface through these large deformations/CAs. As discussed in subsection 2.1.4, the conformity level of TKR implants is conditioned by the geometry of the UHMWPE tibial surface in contact with the double convex surface of the femoral condyles.

Any geometrical change of the articulating surface of UHMWPE will produce deviations of the knee joint kinematics from the optimal designed conditions, increasing the likelihood of abnormally high stress and, ultimately, to wear debris formation.
Accordingly, including creep and plasticity into a constitutive model would help the pre-clinical assessment of TKR designs, to improve their performance *in vivo* by accurately predicting the volumetric wear through the CP, which in turn is linked to variations in the knee kinematics due to changes in the contact surface geometry of the UHMWPE. It is noteworthy that creep and plasticity deformations occur simultaneously as a part of a complex time-dependent nonlinear mechanism related to the semi-crystalline nature of UHMWPE. Quantifying these effects experimentally is certainly very challenging.

These numerical models featuring relatively simple constitutive laws and used without "tuning" the constitutive parameters to fit a specific UHMWPE composition, have provided results in good agreement with experimental measurements. Indeed, a better fit between *in silico* and *in vitro* tests can be obtained by calibrating the constitutive parameters to the UHMWPE composition under test at the expense of a loss of generality for the conclusion of these numerical studies.

These physics-based computational studies presented in chapter 3 and chapter 4 have paved the way for considering more advanced constitutive approaches. This led us to select the TNM developed by Bergström and Bischoff (2011). The TNM was used in the context of simulated literature-based experiments to explore any possible correlation between multidirectional sliding and the microstructure evolution of UHMWPE. To this end, the concept of anticoaxiality (Menzel, 2007; Vianello, 1996a), which is a measure of the deviation between the principal directions of the stress and strain tensors, has been introduced to account for molecular chains realignment.

In this study, the effects of different simulated sliding motion paths on selected metrics related to the mechanical response of UHMWPE, and particularly to the molecular chain realignment, have been investigated through *in silico* POD tests.

It was found that the anticoaxility measure is sensitive to change in orientation of the shear vector acting on the surface of UHMWPE during reciprocating/multidirectional sliding. This metric, therefore, is capable of identifying different input sliding motion shapes. The transient response of anticoaxiality measured during multidirectional sliding, could be an indicator of a more substantial modification of the UHMWPE's microstructure at the contact surface than that under reciprocate sliding, where its response is almost invariant through the motion path. Under multidirectional sliding, the polymer chains will constantly deviate from the state of isotropy as the result of change in orientation of the shear vector, which condition can lead to their rupture with consequent damage initiation. This observation is in agreement with the "unified theory of wear" proposed by Wang (2001), where multidirectional sliding is proposed as the main factor that cause orientation softening in UHMWPE, resulting in high wear rates. Moreover, results indirectly indicate that long sliding distances might increase the likelihood of damage initiation in UHMWPE through higher values of von Mises stress and so plastic deformations in both rheological networks.

The knowledge gained and techniques developed in this PhD work will be exploited for the development of wear simulations tools with physics-based predictive capabilities.

6.2 Experimental and modelling simplifying assumptions

As it is always the case with experiments and computational models, a number of simplifying assumptions have to be made and the question is to establish what types of restrictions they place on the domain of validity of the result.

Both numerical models and experiments of chapter 3 did not include kinematic input motions such as V−V, M−L, I−E rotations, and A−P tilt, and unlike the experiment the FE model did not considered the sinusoidal F−E rotation since it was assumed that the CA remained almost unchanged during this motion. This might have led both physical experiments and numerical models to underestimate the *in vivo* deformations at the articulating surface of UHMWPE as the sliding and rocking motions of the femur could have generated shear forces that have not been accounted for. In addition, the tibial insert of the TKR in both *in silico* and *in vitro* tests was assumed to be constantly in compression, although, in reality lift-off frequently occurs in the knee, leading to cyclic transient unloading phases that likely affect the dynamic viscoelastic response of UHMWPE. It would be important to account for these aspects in future computational models and physical experiments.

The constitutive parameters used to define the mechanical response of UHMWPE in all computational studies of this PhD work were extracted from the literature. Tuning the constitutive parameters to the specific material used in the physical experiment would increase the fidelity of the computational model.

The *in vitro* AMTI wear simulator was not provided with a pressure measurement system, therefore simulated CPs measured at the TKR articulation were only compared to literature data, and it would be highly relevant to include these measurements in future physical experiments.

As highlighted in chapter 4, it was not possible to calibrate the TekScan sensor matrix used in the *in vitro* tests to obtain robust measurements of the articulating CP. As a result, it was possible to compare peak and mean CPs only between MBD and FE numerical models. The ability to develop accurate calibration protocols of both measurement system and force (or displacement)-feedback sensors will be important to consider in the future.

It has been demonstrated that chemical and mechanical interactions between the lubricating fluid and the contact surface of the UHMWPE component of joints prosthesis occur in vivo (Costa et al., 1998). For instance, substances contained in the synovial fluid such as proteins and lipids are absorbed at the articulating surface of UHMWPE, and then diffused inside. The combined effect of mechanical stresses and lubricating fluid produces a series of chemo-physical alteration of the articulation surface of UHWMPE, resulting in chemical wear. All simulations presented in this work assumed a dry condition at the contact between the UHMWPE sample and the counterbearing. Therefore, it is desirable that future constitutive models look at the coupling between mechanics and chemistry for a better insight into the nature of wear mechanisms.

The input loading profiles of studies in chapter 3 and chapter 4 were specifically designed to characterise both viscoelastic and viscoplastic properties of the UHMWPE tibial insert, resulting in deviations from *in vivo* conditions. The magnitude of applied loads fell within the physiological range as also reported in D'Lima et al. (2008), while the imposed loading and unloading rates were not physiological. During normal walking, the loading and unloading phases last fractions of seconds rather than thousand of seconds as in these experiments (see **Figure 3.5** and **Figure 4.1**-B). Since the rate of data-collection was set to 1 Hz (a measure per second), and observing that half of the total mechanical response of UHMWPE had already occurred within the first second of loading (see **Figure 4.2**), it can be concluded that the short-time scale transient response of the polymer is not adequately characterised in this experiment.

The study in chapter 5 accounts for only the two extreme sliding motions namely a line and a circle that accordingly to the work of Wang (2001) lead to the lowest and the highest wear rate, respectively. The experimental work of Turell et al. (2003), which considered a series of square sliding motions, each with a different AR, demonstrated that the maximum wear rate does not occur for a squared-shaped sliding motion (AR = 1) as predicted by the "unified theory of wear" proposed by Wang (2001), but rather for a rectangle-shaped sliding motion (AR = 2.33). The current study did not investigate that experimental evidence through tailored *in silico* and/or *in vitro* tests. However, preliminary results (not reported) of simulations using motions such as ellipses with different ARs suggest that the evolution of material anisotropy and the magnitude of inelastic deformations predicted by the TNM lie in between these two extremes.

The deformation mechanisms of UHMWPE from small to large strains depend on the level of stretch applied to the polymer chains. The simulations presented in chapter 5 did not directly used the stretch as metric for studying the chain realignment under multidirectional sliding, but this was captured through the evolution of plastic strain in networks A and B.

6.3 Future work

In this section we identify opportunities for further research that would enhance different aspects of the work presented in this thesis. From this perspective, the following studies for future research are proposed.

6.3.1 Experimental

The nonlinear mechanical response of different UHMWPE compositions could be characterised through mechanical tests such as monotonic and cyclic uniaxial and multi axial traction/compression (i.e. **Figure A.1**). The fracture properties of UHMWPE could also be investigated using the same mechanical tests, but with strains up to the material's fracture limit. The inelastic properties of these different UHMWPE compositions could be tested for strain-rate sensitivity, creep, relaxation, and frequency viscoelasticity. These mechanical tests will supply a set of 15 calibrated parameters of the TNM for each UHMWPE composition.

As highlighted in section 6.2, the physical experiment presented in chapter 4 did not characterise the short-time scale (i.e. subsecond) viscoelastic response of UHMWPE adequately. To bridge this gap, monotonic compressive tests on knee implants with loads lying in the physiological range could be designed (Quinci et al., 2014). In these tests, the nonlinear visco-dynamic response of UHMWPE would be recorded at a data-collection frequency > 1 Hz, perhaps recording 2/4 data points per second (2/4 Hz) at the expense of the total experiment time-length.

Part of the project was focused on possible relations between multidirectional sliding and molecular chains realignment (chapter 5) through finite element analysis, however, no physical experiments were conducted to investigate this material science aspect. To this end, channel-die compression and POD tests could be planned. The capability of the channel-die compression to induce/control the anisotropy in UHMWPE samples, particularly along the flow direction, is well-known (Boontongkong et al., 1998; Bartczak, 2005; Bartczak and Lezak, 2005; Bartczak, 2005). This mechanical test would produce oriented samples that would be used afterwards in a multidirectional (i.e. "staircase" track shape) POD test to study the relationship between crystallographic texture and wear-induced anisotropy. The orientation of crystallites (and so molecular chains) at the contact surface of UHMWPE samples could be measured through a wide-angle-X-ray scattering technique (WAXS).

Dunn et al. (2008) investigated the effect of normal and friction forces (through a "resolved *in situ* friction coefficient") at the articulating surface of UHMWPE samples that were tested under different complex motion paths through a POD device. They found that the apparent frictional coefficient increased with decreasing radius of curvature. The result is consistent with the softening effect proposed by Wang et al. (1997). Therefore, a set of POD tests, each featuring a different motion track shape (i.e. **Figure 6.1**), could be designed to establish the nature of the relation between normal/frictional forces and wear mechanisms through volumetric wear and friction coefficient measurements.

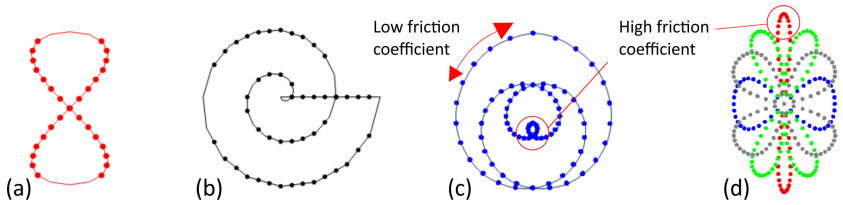

Figure 6.1: Lemniscate (a), Archimedes' spiral (b), double Fermat's spiral (c), Chirps (d) (Dunn et al., 2008).

6.3.2 System modelling

All studies presented in the current PhD work have used simplified assumptions in order to limit the number of variables in a specific system. For instance, computational models in chapter 3 and chapter 4 used simple constitutive laws to predict the mechanical response (i.e. penetration depth, CA and CP) of UHMWPE tibial inserts under compressive loads. While, the study described in chapter 5 used the TNM to investigate the occurrence of molecular chains realignment at the contact surface of cylindrical UHMWPE samples, which were tested in *in silico* POD devices featuring unidirectional/multidirectional sliding. Accordingly, to improve this work, the TNM should be used in simulations of TKR/UKR replicating the actual kinematics of the knee joint. The boundary conditions of the system could combine high frequency applied loads and complex sliding motions. This will render a more realistic picture of the operative conditions in which the UHMWPE tibial insert operates, therefore improving the predictions of its visco-dynamic behaviour and the occurrence of inelastic deformation phenomena.

At the initial stage of a POD test, the UHMWPE might experience a transitioning phase where its wear rate is highly variable. During this phase, which can last hundreds of sliding cycles, molecular chains just start to reorient along preferential directions. A constant wear rate, and presumably a permanent molecular realignment, would be reached after a number of sliding cycles in the order of $10^5/10^6$ (Dressler et al., 2011). In the study of chapter 5, the maximum number of simulated cycles was limited to 100 since the nonlinear nature of the TNM led to very high computational costs. Therefore, in a future work, these simulations should be optimised (i.e. artificially accelerated) so that the number of cycles is in the same order of magnitude as that of *in vitro* POD tests. This would avoid any uncertainty related to the transitioning phase in terms of wear rates and molecular realignment.

6.3.3 Material modelling

The role played by the degree of cross-linking on the molecular chains realignment could also be a subject of further studies. The individual cross-links prevent chain mobility and provide resistance to the cross shear forces, resulting in low wear rates (Sobieraj and Rimnac, 2009). Consequently, an increase in the number of cross-links between molecular chains due to irradiation leads to a grater resistance opposed by these chains to rotation, deformation, and ultimately wear. Therefore, the number of crosslinks could be included within the framework of the TNM as a parameter that accounts for different grades of UHMWPE. This parameter might relate the dose of irradiation to the density of cross-links in the material.

The possible relation between crystallographic mechanisms of deformation and wear could be further investigated *in silico* by argumenting the mechanistic formulation of the TNM, provided experimental data would be available. To this end, the transient and permanent molecular chain realignment would be a function of the particular slip system acting on UHMWPE, which in turn would depend on an energy-related factor. Precisely, the presence of one slip system rather than another will depend on the resistance to shear (i.e. activation energy) offered by that particular system. It is noteworthy that constitutive models accounting for crystallographic mechanisms of deformation already exists, and are classified as polycrystalline composite inclusion models (Van Dommelen et al., 2004, 2003). Crystallographic imperfections could be introduced through random variable obeying specific probability distribution.
The mechanism of molecular chain rupture as a consequence of excessively high deformations applied to crystallites is known to cause the formation/release of wear particles from the surface of UHMWPE (Meyer and Pruitt, 2001), and it can be included in the framework of the TNM by a probability of failure depending on critical stretch, or plastic deformation. The modified TNM should be then used in a simulation replicating a physical channel-die compression test (subsection 6.3.1) in order to verify its predictive capability in/for capturing the evolution of anisotropy in UHMWPE. Moreover, the previously mentioned tensile/compressive testing in which the UHMWPE is subjected to a controlled tension/compression until failure, can be replicated *in silico* in order to establish the ability of the TNM to predict material failure (i.e. wear). In a finite element context, it is well known that softening leads to a physiological mesh dependency. Special techniques such as strain gradient and non-local formulations can solve these issues (Cuvilliez et al., 2012; Pijaudier-Cabot and Bazant, 1987).

It can be assumed that the magnitude of the CP at the articulating surface of UHMWPE will depend upon the number of asperities in contact and their respective contact area, which relates to the type of active wear mechanisms. For instance, the adhesion wear mode dominates at low roughness and in the absence of lubricant, while the abrasive wear mode dominates at high roughness (Alhassan and Goswami, 2008). Wang et al. (2001), based on the Archard's law of wear, found a relation among the CP, coefficient of friction (μ), and the wear factor (κ) that looks like this: $\kappa \propto \mu^2 \propto CP^{-2/6}$. From these observations, parameters such as roughness/hardness of contact surfaces, κ, and CP seem to be linked to μ, and so wear. It would be interesting first to explore/establish the relations among these parameters through tailored *in vitro* tests, and afterwords implement them within the framework of the TNM. Then, the TNM would be used in physical-based simulations of POD tests to find, for instance, a correlation between wear mechanisms and μ (i.e. POD test/μ in subsection 6.3.1).

6.4 Conclusions

- Creep deformations alter the contact properties (CA and CP) of UHMWPE components used in joint implants. The continuous change of CA over time modifies the characteristics of the implant kinematics with deviations from an optimal condition, resulting in high CPs and wear rates. Therefore, it is mandatory to account for creep deformations in the constitutive model when predicting damage of UHMWPE under complex loading conditions or when assessing/comparing the performance of new different knee geometries.
- Under multidirectional sliding, the polymer chains constantly deviate from a state of isotropy (anticoaxiality) as the result of change in orientation of the shear vector, which condition can lead to their rupture and high wear rates.
- Long sliding distances generate high von Mises stresses and plastic deformations in both amorphous and crystalline phases, increasing the likelihood of damage initiation/propagation in the UHMWPE tibial insert of knee implants.

Appendix A

Mechanical tests on UHMWPE

In this appendix, specific mechanical tests such as monotonic and cyclic uniaxial traction/compression that were used to validate the TNM implementation are presented. The simulations, using the TNM, of a relation test at different engineering strain rates are also presented.

A.1 Uniaxial traction/compression, and cyclic tests

The TNM features 15 input parameters, which are obtained through specific mechanical tests such as monotonic and cyclic uniaxial traction/compression. Each set of parameters defines a specific polyethylene composition. The TNM model numerical implementation was validated against experimental data using the same input parameters as those identified in Bergström and Bischoff (2011). The particular type of UHMWPE tested was a ram-extruded GUR 1050 heat treated at 110 °C for 2 hours. In **Figure A.1**, a few examples of the fitting are reported on the left plots, while right plots are the results of the FE models.

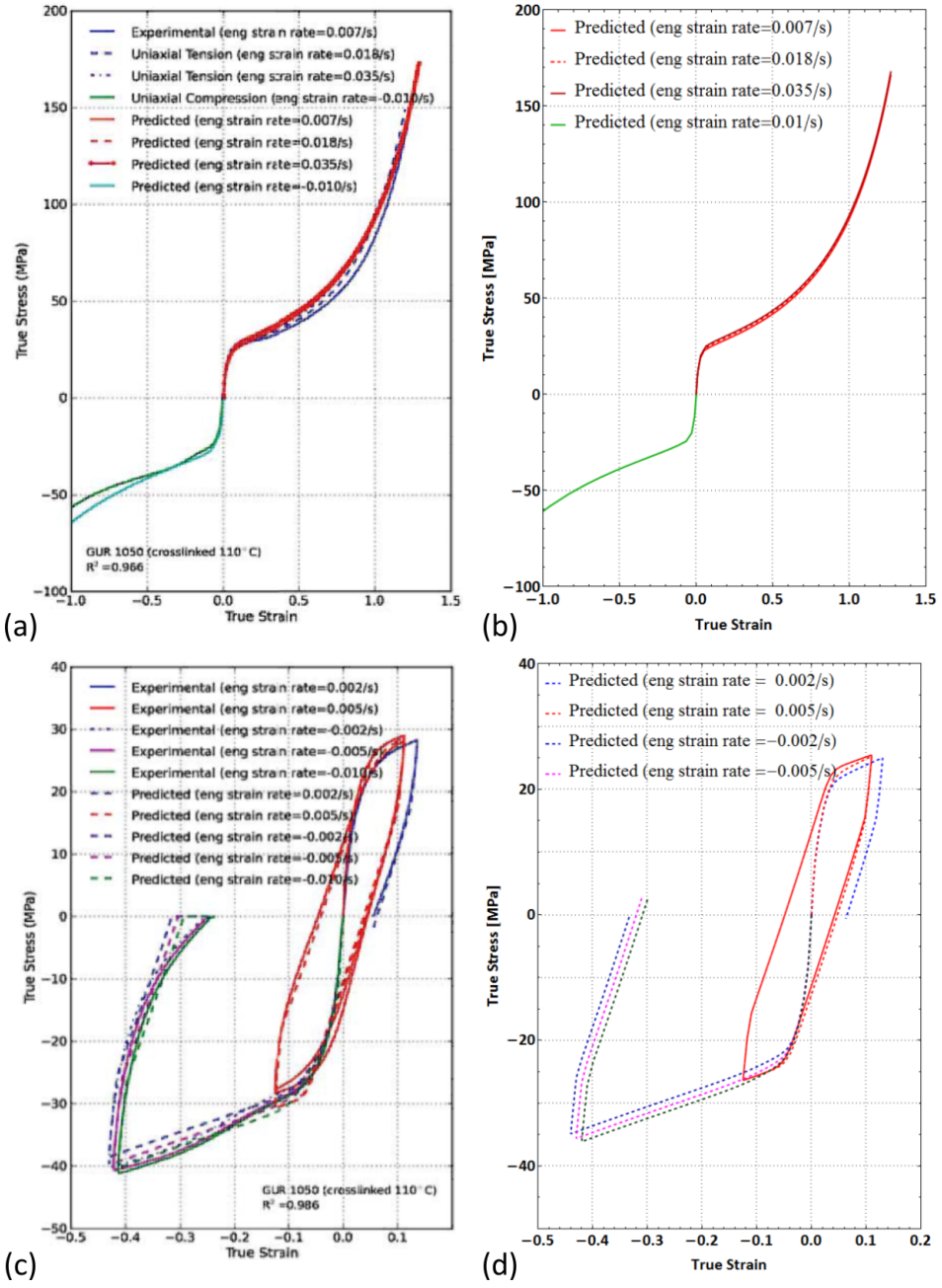

Figure A.1: Uniaxial traction/compression for monotonic and cyclic experimental tests are presented in panels (a) and (c) (reprinted with permission from Bergström and Bischoff (2011)), while results from the calibrated constitutive model in panels (b) and (d).

A.2 Stress relaxation test

The stress relaxation behaviour of UHMWPE was explored through simulations of strain-rate controlled experiments (Gomaa and Leisinger, 2010). The nonlinear behaviour of UHMWPE was modelled using the TNM. For this *in silico* relaxation study, tension tests were conducted using three different engineering strain rates, $1.0^{-3}s^{-1}$, $1.0^{-2}s^{-1}$ and $1.0^{-1}s^{-1}$. The duration of the *in vitro* test and its *in silico* replica was of 1 hour for specimen strained to 5 % strain. Although Gomaa and Leisinger (2010) used the TNM to characterise the nonlinear behaviour of a UHMWPE with brand name Marathon ®, the calibrated constitutive parameters for that specific composition were not available . Therefore, input parameters for the TNM were extracted from the published work of Bergström and Bischoff (2011). The TNM, although using generic data, was still able to closely replicate the general trend and also the shapes of the experimental stress relaxation curves (i.e. rates), as illustrated in **Figure A.2**.

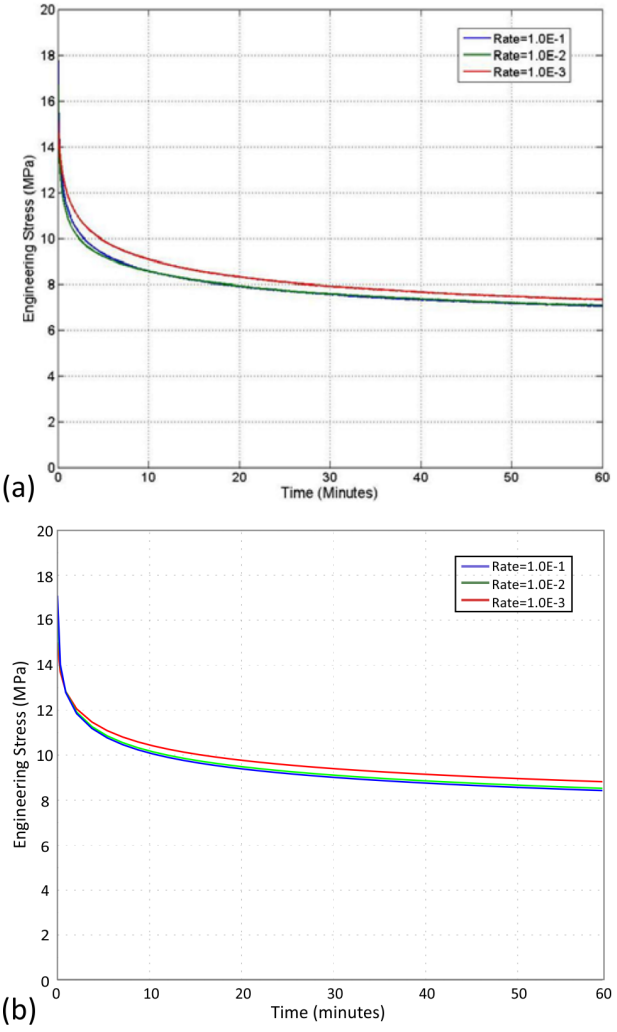

Figure A.2: Stress relaxation experimental data are shown in panel (a) (reprinted with permission from Gomaa and Leisinger (2010)), while results from simulations in panel (b).

Appendix B

Reference frames in the human body

This appendix reports the reference frames in the human body in terms of planes, translations, and rotations. The kinematics of the knee joint is also described.

B.1 Planes and translations

The human body can be sectioned through three orthogonal reference planes (Strickland, 2009).

- The **sagittal plane** is normal to the the Medial-Lateral (M−L) axis, and contains the Anterior-Posterior (A−P) and Inferior-Superior (I−S) axes. The mid-sagittal plane can also be termed *median* plane.
- The **coronal plane** is normal to the A−P axis, and contains the M−L and I−S axes.
- The **transverse plane** is normal to the I−S axis, and contains the M−L and A−P axes.

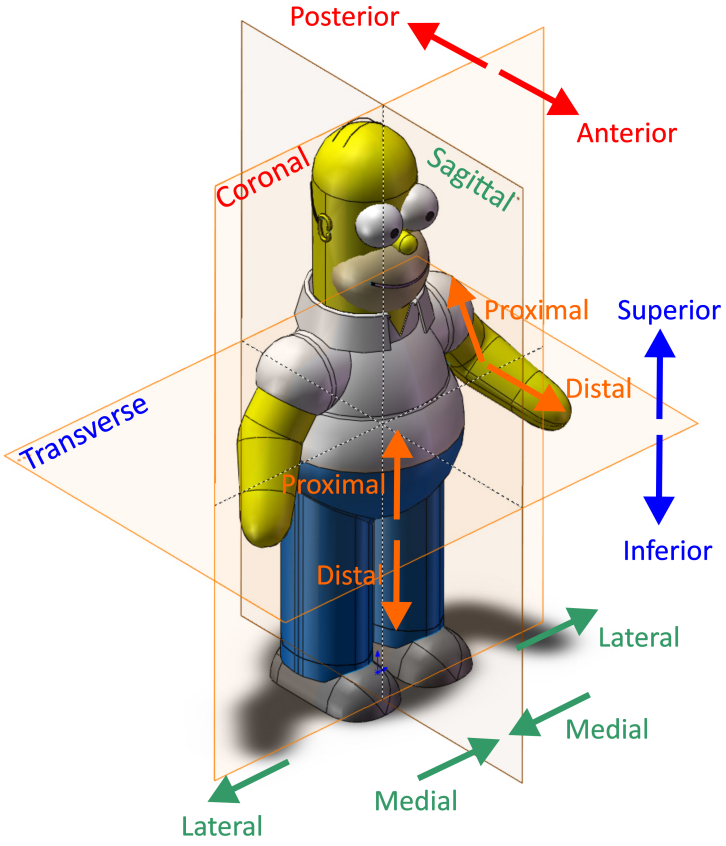

The *translational* terms can be described as follow (Strickland, 2009):

- **Inferior**: Closer to the ground.
- **Superior**: Closer to the head.
- **Medial**: Toward the sagittal plane.
- **Lateral**: Away from the sagittal plane.
- **Anterior**: Forward the front body's surface.
- **Posterior**: Toward the rear body's surface.
- **Proximal**: Closer to the centre of the body.
- **Distal**: Away from the centre of the body.

B.2 Rotations

The *rotational* terms are defined as follow (Strickland, 2009):

- **Abduction**: Motion directed away form the mid-sagittal plane.
- **Adduction**: Motion towards the mid-sagittal plane.
- **Varus**: An inward twisting of the distal limb.
- **Valgus**: An outward twisting of the distal limb.
- **Flexion**: Motion that reduces the knee angle.
- **Extension**: Motion that increases the knee angle.
- **Hyperextension**: Extension beyond the knee range of motion.
- **Internal rotation**: Rotation inwards.
- **External rotation**: Rotation outwards.

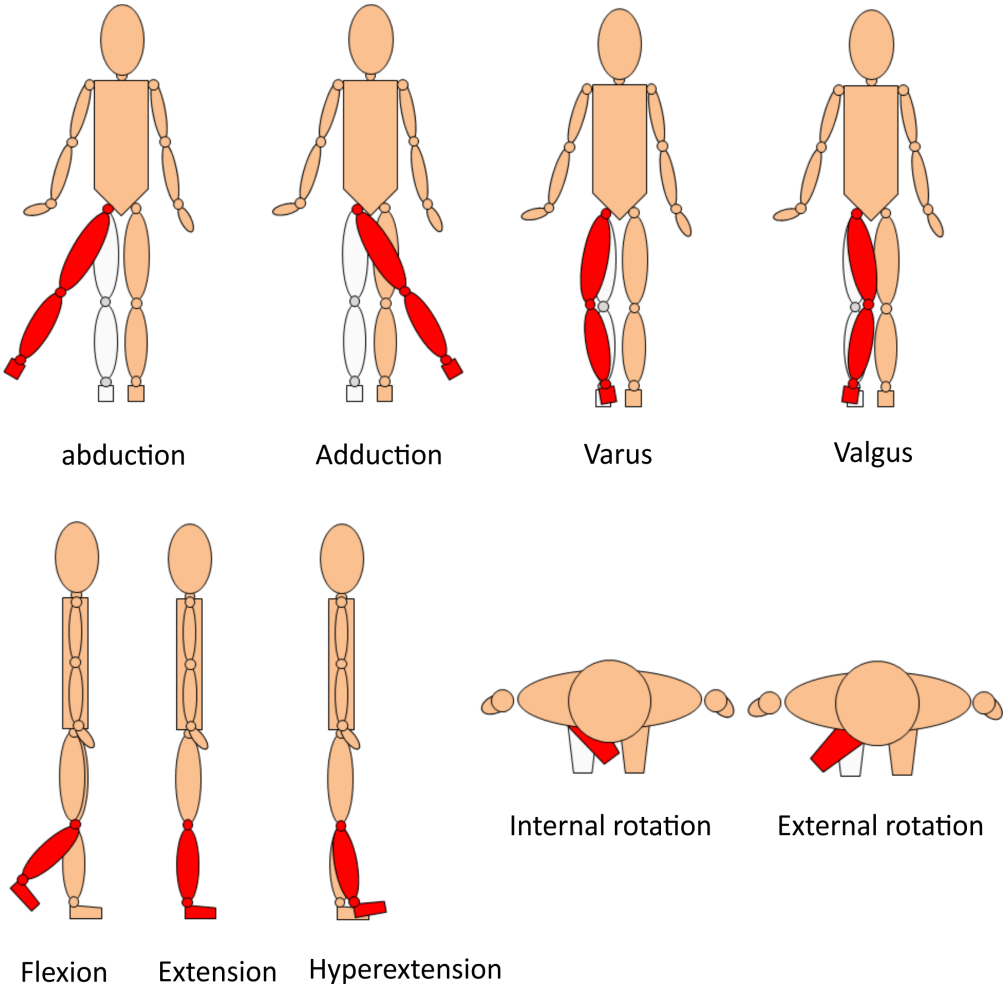

B.3 Translations and rotations at the tibiofemoral joint

Figure B.1 illustrates a right knee with the conventional terms used to described the kinematics of the tibiofemoral joint. Generally, *proximal* and *distal* are more suitable terms to use than *inferior* and *superior*. For instance, the *distal* direction along the tibia is *inferior* when the knee is fully extended, while is *posterior* when the knee is flexed of 90 °. The frame of reference should always be reported; the *anterior* motion of the tibia is equal to the *posterior* motion of the femur (Strickland, 2009).

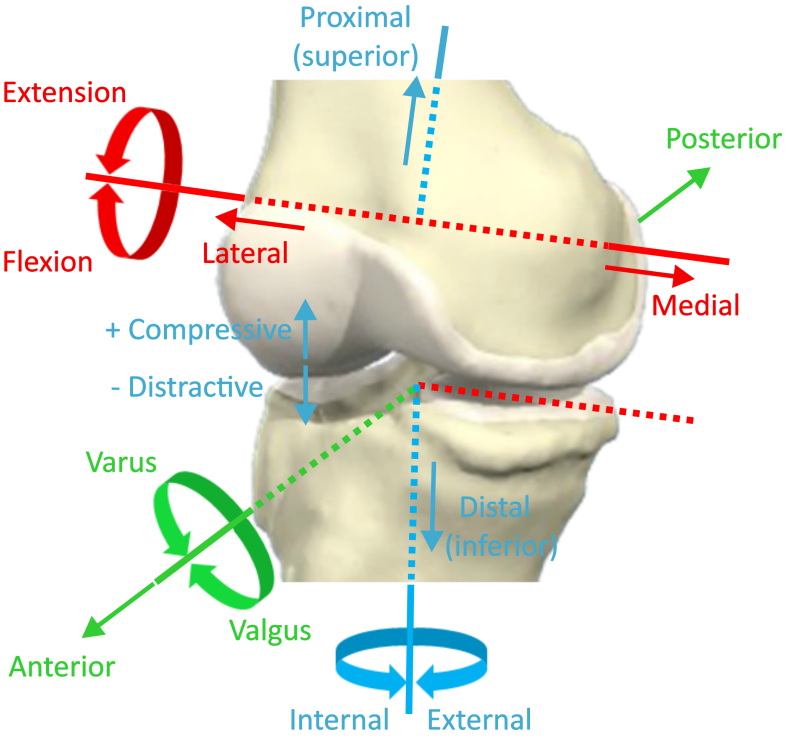

Figure B.1: Schematic of the knee joint kinematics

Appendix C

Publications

- **Articles**

  1. **Quinci, F.**, Dressler, M., Strickland, A.M., Limbert, G., 2014. Towards an accurate understanding of UHMWPE visco-dynamic behaviour for numerical modelling of implants. Journal of the mechanical behavior of biomedical materials 32, 62-75.
  2. **Quinci F**, Dressler, M. R., Strickland, A. M. and Limbert, G., 2013. Micromechanical modelling of UHMWPE chain realignment in multi-directional sliding. *In preparation.*

- **Book chapters**

  1. **Quinci F**, Matthew Dressler, Anthony M. Strickland, Amber Metcalfe, Mark Taylor, and Georges Limbert, 2013. The role of viscoelastic and plastic effects in the creep behaviour of UHMWPE: An experimentally based computational study using an AMTI knee wear simulator. In *Multifunctional Materials for Tribological Applications*. Pan Stanford Publishing Pte. Ltd. *In press*

- **Conference abstracts and proceedings**

  1. **Quinci F**, Limbert, G., Strickland, A. M., Dressler, M. R. and Taylor, M, 2011. Creep behaviour of UHMWPE tibial insert under cyclic loading: An experimental and modelling framework. Fourth International Conference on Mechanics of Biomaterials and Tissues, December 11-14, 2011, Marriott Waikola Beach Resort and Spa, Hawaii.
  2. **Quinci F**, Strickland, A. M., Limbert, G., Dressler, M. R. and Taylor, M., 2011. Creep behaviour of UHMWPE in knee joint replacement. The International Conference on Biotribology, September, 18-21, 2011, Imperial College, London, UK.

- **Publications from collaborations and parallel research activity**

  1. Katsamenis, O.L., Jenkins, T., **Quinci F**., Michopoulou, S., Sinclair, I., Thurner, P.J., 2013. A Novel Videography Method for Generating Crack-Extension Resistance Curves in Small Bone Samples. PloS one 8, e55641.

2. Mazzitelli, S., Capretto, L., **Quinci F**., Piva, R., Nastruzzi, C., 2013. Preparation of cell-encapsulation devices in confined microenvironment. Advanced drug delivery reviews 65, 1533-1555.

References

ABAQUS, U. M. (2012). 6.12.1 documentation. *Dassault Systemes Simulia Corporation., Providence, RI, USA*.

Abdelgaied, A., Liu, F., Brockett, C., Jennings, L., Fisher, J., and Jin, Z. (2011). Computational wear prediction of artificial knee joints based on a new wear law and formulation. *Journal of biomechanics*, 44(6):1108–1116.

Alhassan, S. and Goswami, T. (2008). Wear rate model for uhmwpe in total joint applications. *Wear*, 265(1):8–13.

Allan, P. and Bevis, M. (1980). Deformation processes in thin melt-cast films of high-density polyethylene ii. deformation processes in the non-equatorial regions of spherulites. *Philosophical Magazine A*, 41(4):555–572.

Archard, J. (1953). Contact and rubbing of flat surfaces. *Journal of applied physics*, 24(8):981–988.

Argon, A. (2013). *The physics of deformation and fracture of polymers*. Cambridge University Press.

Arruda, E. M. and Boyce, M. C. (1993). A three-dimensional constitutive model for the large stretch behavior of rubber elastic materials. *Journal of the Mechanics and Physics of Solids*, 41(2):389–412.

Ashcroft, N. W. and Mermin, N. D. (1976). Solid state physics (holt. *Rinehart and Winston, New York*, 19761.

Atkinson, J., Dowson, D., Isaac, J., and Wroblewski, B. (1985). Laboratory wear tests and clinical observations of the penetration of femoral heads into acetabular cups in total replacement hip joints: Iii: The measurement of internal volume changes in explanted charnley sockets after 2–16 years in vivo and the determination of wear factors. *Wear*, 104(3):225–244.

Banks, S. and Sawyer, W. (2005). Quantifying multidirectional sliding motions in total knee replacements. *Journal of Tribology(Transactions of the ASME)*, 127(2):280–286.

Barbour, P., Barton, D., and Fisher, J. (1995). The influence of contact stress on the wear of uhmwpe for total replacement hip prostheses. *Wear*, 181:250–257.

Barbour, P., Stone, M., and Fisher, J. (1999). A study of the wear resistance of three types of clinically applied uhmwpe for total replacement hip prostheses. *Biomaterials*, 20(22):2101–2106.

Barbour, P. M., Barton, D., and Fisher, J. (1997). The influence of stress conditions on the wear of uhmwpe for total joint replacements. *Journal of materials science: Materials in medicine*, 8(10):603–611.

Barron, D. and Birkinshaw, C. (2008). Ultra-high molecular weight polyethylene–evidence for a three-phase morphology. *Polymer*, 49(13):3111–3115.

Bartczak, Z. (2005). Influence of molecular parameters on high-strain deformation of polyethylene in the plane-strain compression. part ii. strain recovery. *Polymer*, 46(23):10339–10354.

Bartczak, Z. and Lezak, E. (2005). Evolution of lamellar orientation and crystalline texture of various polyethylenes and ethylene-based copolymers in plane-strain compression. *Polymer*, 46(16):6050–6063.

Baykal, D., Siskey, R., Haider, H., Saikko, V. and, A. T., and Kurtz, S. (2013). Advances in tribological testing of artificial joint biomaterials using multidirectional pin-on-disk testers. *Journal of the Mechanical Behavior of Biomedical Materials, http://dx.doi.org/10.1016/j.jmbbm.2013.05.020.*

Bennett, D. B., Orr, J. F., and Baker, R. (2000). Movement loci of selected points on the femoral head for individual total hip arthroplasty patients using three-dimensional computer simulation. *The Journal of Arthroplasty*, 15(7):909–915.

Bergmann, G., Deuretzbacher, G., Heller, M., Graichen, F., Rohlmann, A., Strauss, J., and Duda, G. (2001). Hip contact forces and gait patterns from routine activities. *Journal of biomechanics*, 34(7):859–871.

Bergström, J. and Bischoff, J. (2011). An advanced thermomechanical constitutive model for uhmwpe. *The International Journal of Structural Changes in Solids*, 2(1):31–39.

Bergström, J., Kurtz, S., Rimnac, C., and Edidin, A. (2002). Constitutive modeling of ultra-high molecular weight polyethylene under large-deformation and cyclic loading conditions. *Biomaterials*, 23(11):2329–2343.

Bergström, J., Rimnac, C., and Kurtz, S. (2003). Prediction of multiaxial mechanical behavior for conventional and highly crosslinked uhmwpe using a hybrid constitutive model. *Biomaterials*, 24(8):1365–1380.

Bevill, S. L., Bevill, G. R., Penmetsa, J. R., Petrella, A. J., and Rullkoetter, P. J. (2005). Finite element simulation of early creep and wear in total hip arthroplasty. *Journal of biomechanics*, 38(12):2365–2374.

Bitsakos, C., Kerner, J., Fisher, I., and Amis, A. A. (2005). The effect of muscle loading on the simulation of bone remodelling in the proximal femur. *Journal of Biomechanics*, 38(1):133–139.

Boontongkong, Y., Cohen, R., Spector, M., and Bellare, A. (1998). Orientation of plane strain-compressed ultra-high-molecular-weight polyethylene. *Polymer*, 39(25):6391–6400.

Bowden, P. and Young, R. (1974). Deformation mechanisms in crystalline polymers. *Journal of Materials Science*, 9(12):2034–2051.

Boyce, M. C., Weber, G., and Parks, D. M. (1989). On the kinematics of finite strain plasticity. *Journal of the Mechanics and Physics of Solids*, 37(5):647–665.

Bragdon, C., O'Connor, D., Lowenstein, J., Jasty, M., and Syniuta, W. (1996). The importance of multidirectional motion on the wear of polyethylene. *Proceedings of the Institution of Mechanical Engineers, Part H: Journal of Engineering in Medicine*, 210(3):157–165.

Bragdon, C. R., O'Connor, D. O., Lowenstein, J. D., Jasty, M., Biggs, S. A., and Harris, W. H. (2001). A new pin-on-disk wear testing method for simulating wear of polyethylene on cobalt-chrome alloy in total hip arthroplasty. *The Journal of Arthroplasty*, 16(5):658–665.

Burbank, R. (1960). Molecular structure in crystal aggregates of linear polyethylene. *Bell System Technical Journal*, 39(6):1627–1663.

Cameron, H. U. and Hunter, G. A. (1982). Failure in total knee arthroplasty: mechanisms, revisions, and results. *Clinical Orthopaedics and Related Research*, 170:141–146.

Carr, B. C. and Goswami, T. (2009). Knee implants–review of models and biomechanics. *Materials & Design*, 30(2):398–413.

Casey, D., Cottrell, J., DiCarlo, E., Windsor, R., and Wright, T. (2007). Pfc knee replacement: osteolytic failures from extreme polyethylene degradation. *Clinical orthopaedics and related research*, 464:157–163.

Charnley, J. (1976). The wear of plastics materials in the hip joint. *Plastics and Rubber*, 1(2):59–63.

Charnley, J. and Cupic, Z. (1973). The nine and ten year results of the low-friction arthroplasty of the hip. *Clinical Orthopaedics and Related Research*, 95:9–25.

Costa, L., Luda, M., Trossarelli, L., Brach del Prever, E., Crova, M., and Gallinaro, P. (1998). In vivo uhmwpe biodegradation of retrieved prosthesis. *Biomaterials*, 19(15):1371–1385.

Cowking, A., Rider, J., Hay, I., and Keller, A. (1968). A study on the orientation effects in polyethylene in the light of crystalline texture. *Journal of Materials Science*, 3(6):646–654.

Cuvilliez, S., Feyel, F., Lorentz, E., and Michel-Ponnelle, S. (2012). A finite element approach coupling a continuous gradient damage model and a cohesive zone model within the framework of quasi-brittle failure. *Computer Methods in Applied Mechanics and Engineering*, 237:244–259.

Das-Gupta, D. K. (1994). Polyethylene: structure, morphology, molecular motion and dielectric behavior. *Electrical Insulation Magazine, IEEE*, 10(3):5–15.

Davey, S., Orr, J., Buchanan, F., Nixon, J., and Bennett, D. (2004). Measurement of molecular orientation in retrieved ultra-high-molecular-weight polyethylene (uhmwpe) hip sockets using fourier-transform infrared spectroscopy. *Strain*, 40(4):203–210.

de Souza Neto, E., Perić, D., Dutko, M., and Owen, D. (1996). Design of simple low order finite elements for large strain analysis of nearly incompressible solids. *International Journal of Solids and Structures*, 33(20):3277–3296.

Deng, M., Latour, R. A., Ogale, A. A., and Shalaby, S. W. (1998). Study of creep behavior of ultra-high-molecular-weight polyethylene systems. *Journal of biomedical materials research*, 40(2):214–223.

Deng, M. and Shalaby, S. W. (1997). Properties of self-reinforced ultra-high-molecular-weight polyethylene composites. *Biomaterials*, 18(9):645–655.

DesJardins, J., Gustafson, L., Benson, L., and LaBerge, M. (2005). Fiberscopic visualization of total knee replacement contact kinematics during in vitro simulation. ASME.

Diezi, C., Wirth, S., Meyer, D. C., and Koch, P. P. (2010). Effect of femoral to tibial varus mismatch on the contact area of unicondylar knee prostheses. *The Knee*, 17(5):350–355.

D'Lima, D. D., Steklov, N., Fregly, B. J., Banks, S. A., and Colwell, C. W. (2008). In vivo contact stresses during activities of daily living after knee arthroplasty. *Journal of Orthopaedic Research*, 26(12):1549–1555.

Dressler, M. R., Strickland, M. A., Taylor, M., Render, T. D., and Ernsberger, C. N. (2011). Predicting wear of uhmwpe: Decreasing wear rate following a change in direction. *Wear*, 271(11):2879–2883.

Dunn, A. C., Steffens, J. G., Burris, D. L., Banks, S. A., and Sawyer, W. G. (2008). Spatial geometric effects on the friction coefficients of uhmwpe. *Wear*, 264(7):648–653.

Edidin, A. A., Pruitt, L., Jewett, C. W., Crane, D. J., Roberts, D., and Kurtz, S. M. (1999). Plasticity-induced damage layer is a precursor to wear in radiation-cross-linked uhmwpe acetabular components for total hip replacement. *The Journal of arthroplasty*, 14(5):616–627.

Eyerer, P., Frank, A., and Jin, R. (1985). Characterization of ultra-high molecular weight polyethylene (uhmwpe): Extraction and viscometry of uhmwpe. *Plastverarbeiter*, 36:46–54.

Feldman, L. A. and Hui, H. K. (1997). Compatibility of medical devices and materials with low-temperature hydrogen peroxide gas plasma. *Medical Device and Diagnostic Industry*, 19:57–63.

Fisher, J., Dowson, D., Hamdzah, H., and Lee, H. (1994). The effect of sliding velocity on the friction and wear of uhmwpe for use in total artificial joints. *Wear*, 175(1):219–225.

Flory, P. (1962). On the morphology of the crystalline state in polymers. *Journal of the American Chemical Society*, 84(15):2857–2867.

Fregly, B. J., Bei, Y., and Sylvester, M. E. (2003). Experimental evaluation of an elastic foundation model to predict contact pressures in knee replacements. *Journal of biomechanics*, 36(11):1659–1668.

Galetz, M. C. and Glatzel, U. (2010). Molecular deformation mechanisms in uhmwpe during tribological loading in artificial joints. *Tribology Letters*, 38(1):1–13.

Garvin, K. (2008). Rotating platform versus fixed-bearing total knees: an in vitro study of wear. *Clinical orthopaedics and related research*, 466(11):2677–2685.

Gevaert, M. R., LaBerge, M., Gordon, J. M., and DesJardins, J. D. (2005). The quantification of physiologically relevant cross-shear wear phenomena on orthopaedic bearing materials using the max-shear wear testing system. *Journal of tribology*, 127(4):740–749.

Godest, A., Beaugonin, M., Haug, E., Taylor, M., and Gregson, P. (2002). Simulation of a knee joint replacement during a gait cycle using explicit finite element analysis. *Journal of biomechanics*, 35(2):267–275.

Goldman, M. and Pruitt, L. (1998). Comparison of the effects of gamma radiation and low temperature hydrogen peroxide gas plasma sterilization on the molecular structure, fatigue resistance, and wear behavior of uhmwpe. *Journal of biomedical materials research*, 40(3):378–384.

Gomaa, S. T. (2011). Predicting the effect of creep of uhmwpe on the femoral-tibial contact area and contact stresses following total knee arthroplasty. In *Orthopaedic Research Society Annual Meeting*.

Gomaa, S. T. and Leisinger, S. (2010). Testing and modeling the nonlinear behavior of uhmwpe used in orhtopaedic implants. volume 0104. ASB.

Goreham-Voss, C. M., Hyde, P. J., Hall, R. M., Fisher, J., and Brown, T. D. (2010). Cross-shear implementation in sliding-distance-coupled finite element analysis of wear in metal-on-polyethylene total joint arthroplasty: Intervertebral total disc replacement as an illustrative application. *Journal of biomechanics*, 43(9):1674–1681.

Haasen, P., Kramer, E. J., Meijer, H. E., and Cahn, R. W. (1997). *Materials science and technology: a comprehensive treatment*, volume 18. VCH.

Hailey, J., Fisher, J., Dowson, D., Sampath, S., Johnson, R., and Elloy, M. (1994). A tribological study of a series of retrieved accord knee explants. *Medical engineering & physics*, 16(3):223–228.

Halloran, J. P., Petrella, A. J., and Rullkoetter, P. J. (2005). Explicit finite element modeling of total knee replacement mechanics. *Journal of biomechanics*, 38(2):323–331.

Hasan, O. and Boyce, M. (1995). A constitutive model for the nonlinear viscoelastic viscoplastic behavior of glassy polymers. *Polymer Engineering & Science*, 35(4):331–344.

Hinton, T., Rider, J., and Simpson, L. (1974). Chain and fibrillar slip in oriented polyethylene. *Journal of Materials Science*, 9(8):1331–1336.

Isaac, G., Dowson, D., and Wroblewski, B. (1996). An investigation into the origins of time-dependent variation in penetration rates with charnley acetabular cupswear, creep or degradation? *Proceedings of the Institution of Mechanical Engineers, Part H: Journal of Engineering in Medicine*, 210(3):209–216.

Jauffrès, D., Lame, O., Vigier, G., Doré, F., and Fridrici, V. (2008). Yield, creep, and wear properties of ultra high molecular weight polyethylene processed by high velocity compaction. *Journal of Applied Polymer Science*, 110(5):2579–2585.

Johannes, V., Green, M., and Brockley, C. (1973). The role of the rate of application of the tangential force in determining the static friction coefficient. *Wear*, 24(3):381–385.

Johnson, K. L. and Johnson, K. L. (1987). *Contact mechanics*. Cambridge university press.

Kabo, J., Gebhard, J., Loren, G., and Amstutz, H. (1993). In vivo wear of polyethylene acetabular components. *Journal of Bone & Joint Surgery, British Volume*, 75(2):254–258.

Kang, L., Galvin, A. L., Brown, T. D., Jin, Z., and Fisher, J. (2008). Quantification of the effect of cross-shear on the wear of conventional and highly cross-linked uhmwpe. *Journal of biomechanics*, 41(2):340–346.

Keller, A. (1979). Networks and crystallinity. *Polymer*, 20(11):1371–1372.

Kim, J., Nelson, C. L., and Lotke, P. A. (2004). Stiffness after total knee arthroplastyprevalence of the complication and outcomes of revision. *The Journal of Bone & Joint Surgery*, 86(7):1479–1484.

Knight, L. A., Pal, S., Coleman, J. C., Bronson, F., Haider, H., Levine, D. L., Taylor, M., and Rullkoetter, P. J. (2007). Comparison of long-term numerical and experimental total knee replacement wear during simulated gait loading. *Journal of biomechanics*, 40(7):1550–1558.

Korduba, L. and Wang, A. (2011). The effect of cross-shear on the wear of virgin and highly-crosslinked polyethylene. *Wear*, 271(9):1220–1223.

Korelc, J. (2002). Multi-language and multi-environment generation of nonlinear finite element codes. *Engineering with computers*, 18(4):312–327.

Korelc, J., Šolinc, U., and Wriggers, P. (2010). An improved eas brick element for finite deformation. *Computational Mechanics*, 46(4):641–659.

Krichen, A., Ketata, H., and Elgasri, S. (2006). Visualisation of tibiofemoral contact in total knee replacement using optical device. *The Knee*, 13(3):226–230.

Kurtz, S., Medel, F. J., and Manley, M. (2008). (iii) wear in highly crosslinked polyethylenes. *Current orthopaedics*, 22(6):392–399.

Kurtz, S. M. (2009). *UHMWPE biomaterials handbook: ultra high molecular weight polyethylene in total joint replacement and medical devices*. Access Online via Elsevier.

Kurtz, S. M., Muratoglu, O. K., Evans, M., and Edidin, A. A. (1999). Advances in the processing, sterilization, and crosslinking of ultra-high molecular weight polyethylene for total joint arthroplasty. *Biomaterials*, 20(18):1659–1688.

Kurtz, S. M., Pruitt, L., Jewett, C. W., Paul Crawford, R., Crane, D. J., and Edidin, A. A. (1998). The yielding, plastic flow, and fracture behavior of ultra-high molecular weight polyethylene used in total joint replacements. *Biomaterials*, 19(21):1989–2003.

Lapedes, D. N. (1978). Mcgraw-hill dictionary of scientific and technical terms.

Lavernia, C. J., Sierra, R. J., Hungerford, D. S., and Krackow, K. (2001). Activity level and wear in total knee arthroplasty: a study of autopsy retrieved specimens. *The Journal of arthroplasty*, 16(4):446–453.

Lee, K.-Y. and Pienkowski, D. (1997). Reduction in the initial wear of ultrahigh molecular weight polyethylene after compressive creep deformation. *Wear*, 203:375–379.

Lengiewicz, J., Korelc, J., and Stupkiewicz, S. (2011). Automation of finite element formulations for large deformation contact problems. *International Journal for Numerical Methods in Engineering*, 85(10):1252–1279.

Liau, J.-J., Cheng, C.-K., Huang, C.-H., and Lo, W.-H. (2002). Effect of fuji pressure sensitive film on actual contact characteristics of artificial tibiofemoral joint. *Clinical Biomechanics*, 17(9):698–704.

Lin, L. and Argon, A. (1994). Structure and plastic deformation of polyethylene. *Journal of Materials Science*, 29(2):294–323.

Long, M. and Rack, H. (1998). Titanium alloys in total joint replacementa materials science perspective. *Biomaterials*, 19(18):1621–1639.

Lubarda, V. A. (2004). Constitutive theories based on the multiplicative decomposition of deformation gradient: Thermoelasticity, elastoplasticity, and biomechanics. *Appl. Mech. Rev*, 57(2):95–108.

MacIntosh, D. and Hunter, G. (1972). The use of the hemiarthroplasty prosthesis for advanced osteoarthritis and rheumatoid arthritis of the knee. *The Journal of bone and joint surgery. British volume*, 54(2):244.

Malchau, H. and Herberts, P. (1996). Prognosis of total hip replacement. *The International Journal of Risk and Safety in Medicine*, 8(1):27–45.

Marieb, E. N. and Hoehn, K. (2007). *Human anatomy and physiology*. Pearson Education.

Mazzucco, D. and Spector, M. (2003). Effects of contact area and stress on the volumetric wear of ultrahigh molecular weight polyethylene. *Wear*, 254(5):514–522.

McEwen, H., Fisher, J., Goldsmith, A., Auger, D., Hardaker, C., and Stone, M. (2001). Wear of fixed bearing and rotating platform mobile bearing knees subjected to high levels of internal and external tibial rotation. *Journal of Materials Science: Materials in Medicine*, 12(10-12):1049–1052.

McGloughlin, T. M. and Kavanagh, A. (2000). Wear of ultra-high molecular weight polyethylene (uhmwpe) in total knee prostheses: a review of key influences. *Proceedings of the Institution of Mechanical Engineers, Part H: Journal of Engineering in Medicine*, 214(4):349–359.

McKellop, H., Shen, F.-w., Lu, B., Campbell, P., and Salovey, R. (1999). Development of an extremely wear-resistant ultra high molecular weight polythylene for total hip replacements. *Journal of Orthopaedic Research*, 17(2):157–167.

Menzel, A. (2007). A fibre reorientation model for orthotropic multiplicative growth. *Biomechanics and modeling in mechanobiology*, 6(5):303–320.

Metcalfe, A. (2011). Quantifying deformation and recovery of polyethylene in total knee replacement. In *Transactions Society for Biomaterials.*

Meyer, R. and Pruitt, L. (2001). The effect of cyclic true strain on the morphology, structure, and relaxation behavior of ultra high molecular weight polyethylene. *Polymer*, 42(12):5293–5306.

Muratoglu, O. K., Bragdon, C. R., O'Connor, D. O., Jasty, M., and Harris, W. H. (2001). A novel method of cross-linking ultra-high-molecular-weight polyethylene to improve wear, reduce oxidation, and retain mechanical properties: Recipient of the 1999 hap paul award. *The Journal of arthroplasty*, 16(2):149–160.

Norman, C. C. and Kress, T. (2003). Risk factors for knee osteoarthritis: a review of epidemiological studies. In *Proceedings of the IASTED International Conference on Biomechanics*, pages 6–11.

Pal, S., Haider, H., Laz, P. J., Knight, L. A., and Rullkoetter, P. J. (2008). Probabilistic computational modeling of total knee replacement wear. *Wear*, 264(7):701–707.

Patten, E. W. (2012). A multidirectional tribo-system: Wear of uhmwpe under sliding, rolling, and rotation.

Peacock, A. (2000). *Handbook of polyethylene: structures: properties, and applications*. CRC Press.

Penmetsa, J. R., Laz, P. J., Petrella, A. J., and Rullkoetter, P. J. (2006). Influence of polyethylene creep behavior on wear in total hip arthroplasty. *Journal of orthopaedic research*, 24(3):422–427.

Petrella, A. J., Armstrong, J. R., Laz, P. J., and Rullkoetter, P. J. (2012). A novel cross-shear metric for application in computer simulation of ultra-high molecular weight polyethylene wear. *Computer methods in biomechanics and biomedical engineering*, 15(11):1223–1232.

Pijaudier-Cabot, G. and Bazant, Z. P. (1987). Nonlocal damage theory. *Journal of Engineering Mechanics*, 113(10):1512–1533.

Pruitt, L. A. (2005). Deformation, yielding, fracture and fatigue behavior of conventional and highly cross-linked ultra high molecular weight polyethylene. *Biomaterials*, 26(8):905–915.

Quinci, F., Dressler, M., Strickland, A. M., and Limbert, G. (2014). Towards an accurate understanding of uhmwpe visco-dynamic behaviour for numerical modelling of implants. *Journal of the Mechanical Behavior of Biomedical Materials*.

Reeves, E., Barton, D., FitzPatrick, D., and Fisher, J. (1998). A two-dimensional model of cyclic strain accumulation in ultra-high molecular weight polyethylene knee replacements. *Proceedings of the Institution of Mechanical Engineers, Part H: Journal of Engineering in Medicine*, 212(3):189–198.

Renò, F. and Cannas, M. (2006). Uhmwpe and vitamin e bioactivity: An emerging perspective. *Biomaterials*, 27(16):3039–3043.

Rullkoeter, P. and Gabriel, S. (2000). Viscoelastic behavior of uhmwpe tkr components. In *46th Annual Meeting of the Orthopaedic Research Society*, page 0562.

Saikko, V. (1993). Wear and friction properties of prosthetic joint materials evaluated on a reciprocating pin-on-flat apparatus. *Wear*, 166(2):169–178.

Saikko, V. and Ahlroos, T. (1999). Type of motion and lubricant in wear simulation of polyethylene acetabular cup. *Proceedings of the Institution of Mechanical Engineers, Part H: Journal of Engineering in Medicine*, 213(4):301–310.

Saikko, V. and Ahlroos, T. (2000). Wear simulation of uhmwpe for total hip replacement with a multidirectional motion pin-on-disk device: Effects of counterface material, contact area, and lubricant. *Journal of biomedical materials research*, 49(2):147–154.

Saikko, V., Calonius, O., and Keränen, J. (2001). Effect of counterface roughness on the wear of conventional and crosslinked ultrahigh molecular weight polyethylene studied with a multidirectional motion pin-on-disk device. *Journal of biomedical materials research*, 57(4):506–512.

Saikko, V., Calonius, O., and Keränen, J. (2004). Effect of slide track shape on the wear of ultrahigh molecular weight polyethylene in a pin-on-disk wear simulation of total hip prosthesis. *Journal of Biomedical Materials Research Part B: Applied Biomaterials*, 69(2):141–148.

Seto, T., Hara, T., and Tanaka, K. (1968). Phase transformation and deformation processes in oriented polyethylene. *Jap. J. Appl. Phys*, 7:31.

Shadrake, L. and Guiu, F. (1979). Elastic line energies and line tensions of dislocations in polyethylene crystals. *Philosophical Magazine A*, 39(6):785–796.

Sobieraj, M. and Rimnac, C. (2009). Ultra high molecular weight polyethylene: mechanics, morphology, and clinical behavior. *Journal of the mechanical behavior of biomedical materials*, 2(5):433–443.

Strickland, A. M. (2009). *Enhanced pre-clinical assessment of total knee replacement using computational modelling with experimental corroboration & probabilistic applications*. PhD thesis, University of Southamtpon.

Strickland, M., Dressler, M., Render, T., Browne, M., and Taylor, M. (2011). Targeted computational probabilistic corroboration of experimental knee wear simulator: The importance of accounting for variability. *Medical engineering & physics*, 33(3):295–301.

Strickland, M., Dressler, M., and Taylor, M. (2012). Predicting implant uhmwpe wear in-silico: A robust, adaptable computational–numerical framework for future theoretical models. *Wear*, 274:100–108.

Strickland, M. and Taylor, M. (2009). In-silico wear prediction for knee replacementsmethodology and corroboration. *Journal of biomechanics*, 42(10):1469–1474.

Stupkiewicz, S., Lengiewicz, J., and Korelc, J. (2010). Sensitivity analysis for frictional contact problems in the augmented lagrangian formulation. *Computer Methods in Applied Mechanics and Engineering*, 199(33):2165–2176.

Takahashi, Y., Yamamoto, K., Shishido, T., Masaoka, T., Tateiwa, T., Puppulin, L., and Pezzotti, G. (2013). Strain-induced microstructural rearrangement in ultra-high molecular weight polyethylene for hip joints: A comparison between conventional and vitamin e-infused highly-crosslinked liners. *Journal of the mechanical behavior of biomedical materials*.

Turell, M., Wang, A., and Bellare, A. (2003). Quantification of the effect of cross-path motion on the wear rate of ultra-high molecular weight polyethylene. *Wear*, 255(7):1034–1039.

Van Dommelen, J., Parks, D., Boyce, M., Brekelmans, W., and Baaijens, F. (2003). Micromechanical modeling of intraspherulitic deformation of semicrystalline polymers. *Polymer*, 44(19):6089–6101.

Van Dommelen, J., Schrauwen, B., Van Breemen, L., and Govaert, L. (2004). Micromechanical modeling of the tensile behavior of oriented polyethylene. *Journal of Polymer Science Part B: Polymer Physics*, 42(16):2983–2994.

Vianello, M. (1996a). Coaxiality of strain and stress in anisotropic linear elasticity. *Journal of elasticity*, 42(3):283–289.

Vianello, M. (1996b). Optimization of the stored energy and coaxiality of strain and stress in finite elasticity. *Journal of elasticity*, 44(3):193–202.

Villa, T., Migliavacca, F., Gastaldi, D., Colombo, M., and Pietrabissa, R. (2004). Contact stresses and fatigue life in a knee prosthesis: comparison between in vitro measurements and computational simulations. *Journal of biomechanics*, 37(1):45–53.

Walker, P. and Hsieh, H. (1977). Conformity in condylar replacement knee prosthesis. *Journal of Bone & Joint Surgery, British Volume*, 59(2):222–228.

Walker, P. S., Blunn, G. W., and Lilley, P. A. (1996). Wear testing of materials and surfaces for total knee replacement. *Journal of biomedical materials research*, 33(3):159–175.

Wang, A. (2001). A unified theory of wear for ultra-high molecular weight polyethylene in multi-directional sliding. *Wear*, 248(1):38–47.

Wang, A., Essner, A., and Klein, R. (2001). Effect of contact stress on friction and wear of ultra-high molecular weight polyethylene in total hip replacement. *Proceedings of the Institution of Mechanical Engineers, Part H: Journal of Engineering in Medicine*, 215(2):133–139.

Wang, A., Lee, R., Herrera, L., and Korduba, L. (2012a). Wear of ultra-high molecular weight polyethylene moving along a circular path in a hip simulator. *Wear*.

Wang, A., Lee, R., Herrera, L., and Rodriguez, L. (2012b). Modeling and verification of ultra-high molecular weight polyethylene wear in multi-directional sliding. *Wear*.

Wang, A., Stark, C., and Dumbleton, J. (1995). Role of cyclic plastic deformation in the wear of uhmwpe acetabular cups. *Journal of biomedical materials research*, 29(5):619–626.

Wang, A., Stark, C., and Dumbleton, J. (1996). Mechanistic and morphological origins of ultra-high molecular weight polyethylene wear debris in total joint replacement prostheses. *Proceedings of the Institution of Mechanical Engineers, Part H: Journal of Engineering in Medicine*, 210(3):141–155.

Wang, A., Sun, D., Yau, S.-S., Edwards, B., Sokol, M., Essner, A., Polineni, V., Stark, C., and Dumbleton, J. (1997). Orientation softening in the deformation and wear of ultra-high molecular weight polyethylene. *Wear*, 203:230–241.

Waslewski, G. L., Marson, B. M., and Benjamin, J. B. (1998). Early, incapacitating instability of posterior cruciate ligament-retaining total knee arthroplasty. *The Journal of arthroplasty*, 13(7):763–767.

William, F. S. (1995). Scienza e tecnologia dei materiali.

Willing, R. and Kim, I. Y. (2009). A holistic numerical model to predict strain hardening and damage of uhmwpe under multiple total knee replacement kinematics and experimental validation. *Journal of biomechanics*, 42(15):2520–2527.

Woolf, A. D. and Pfleger, B. (2003). Burden of major musculoskeletal conditions. *Bulletin of the World Health Organization*, 81(9):646–656.

Young, R. J. and Lovell, P. A. (1991). *Introduction to polymers*, volume 2. Chapman & Hall London.

Young, W. C. and Budynas, R. G. (2002). *Roark's formulas for stress and strain*, volume 6. McGraw-Hill New York.

Zdero, R., Fenton, P., Rudan, J., and Bryant, J. (2001). Fuji film and ultrasound measurement of total knee arthroplasty contact areas. *The Journal of arthroplasty*, 16(3):367–375.

Zhao, D., Sakoda, H., Sawyer, W. G., Banks, S. A., and Fregly, B. J. (2008). Predicting knee replacement damage in a simulator machine using a computational model with a consistent wear factor. *Journal of biomechanical engineering*, 130(1):011004–11010.

Zhao, D., Sawyer, W. G., and Fregly, B. J. (2006). Computational wear prediction of uhmwpe in knee replacements. *ASTM SPECIAL TECHNICAL PUBLICATION*, 1472:45.